Modeling Ripple Formation

Dissertation

zur

Erlangung des Doktorgrades (Dr. rer. nat.)

der

Mathematisch-Naturwissenschaftlichen Fakultät

der

Rheinischen Friedrich-Wilhelms-Universität Bonn

vorgelegt von

Michael Küpper

aus

Cochem

Bonn 2003

Angefertigt mit Genehmigung der Mathematisch-Naturwissenschaftlichen Fakultät der Rheinischen Friedrich-Wilhelms-Universität Bonn.

Referent: Prof. Dr. Horst J. Neugebauer
Koreferent: Priv. Doz. Dr. Andreas Hördt
Tag der Promotion: 19.08.03

II

Contents

Introduction

Ripples are characteristic patterns which are found in various natural environments. For example, ripples are generated by wind forces on sandy surfaces in deserts or on snowy surfaces. Subaqueous ripples are, on the other hand, present in coastal zones or on river beds. The media which show ripple patterns consist always of granular matter at the boundary. A driving medium (gas, fluid) which is able to entrain particles interacts with the underlying matter in a complex way. The resemblance of the ripple formed by air and by water leads to the false assumption that the physical processes behind both must be similar. If we compare the movement of transported grains in air and in water, one difference is evident: grains lifted up by wind forces fall down impacting the surface (see Sect. 1.4). Grains in water show a more flowing behavior along the sand bed, because the specific weight of the sediment and water differs less (Trefil 1984). Therefore, in rivers ripple formation results from special flow structures and not from impact characteristics as for aeolian ripples (see Sect. 1.6).

The focus of this thesis is on ripples created under uni–directional water flow. We are interested in modeling the sediment transport over bedforms. It is supposed to be one of the most interesting problems among a wide range of processes observed in rivers (Nikora et al. 2002). The questions, which require clarification are manifold: for example, for river engineering it is important to know whether bedforms enhance or reduce sediment transport. Geologists try to relate the morphology of ripples preserved in rock records to ancient flow conditions, and physicists ask for the long term behavior of a ripple system in order to understand the dynamics.

Considering the known facts about subaqueous ripples, it is generally accepted that ripple formation is associated with turbulent flow conditions. In addition, the shear stress acting on the bed surface must be sufficient to entrain sediment. In natural environments the ripple patterns are highly variable and the transition to other structures, for example, dunes are "smooth". Thus during investigations many different classifications have been used (Ashley 1990). From the modeling, view patterns differ only if the belonging formation processes are basically different. Attention is paid therefore to the common morphology of ripples and their dynamics. All observed ripples agree in the following manner: (1) developed ripples move with constant velocities
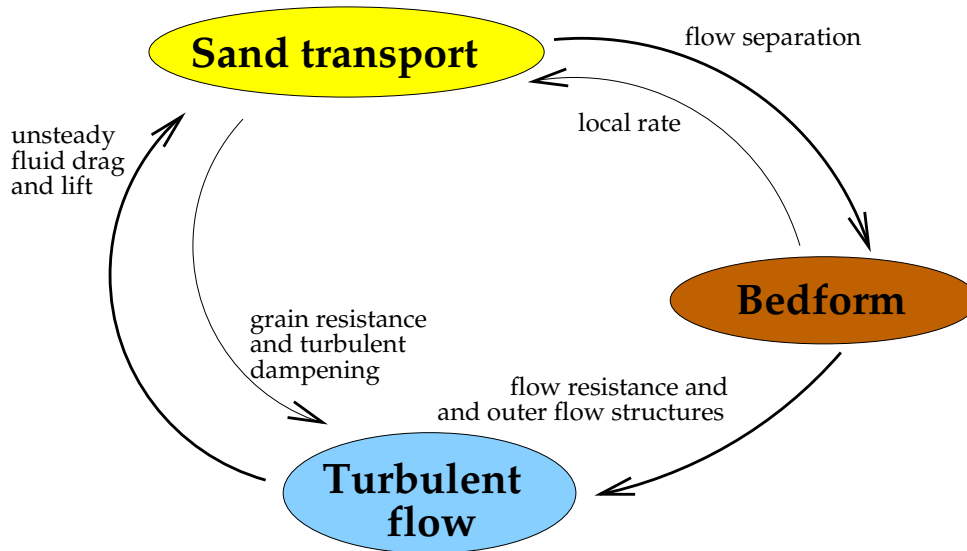
Fig. 0.1. Interrelationship between flow characteristics and bedform development in current flow (Leeder 1980).

almost inversely proportional to their heights (Fredsøe and Deigaard 1992); (2) ripples are asymmetrically shaped with a steep lee side and a flat stoss side (see Fig. 1.1). In this view ripples are simple patterns, which raise expectations that a clear transport process could finally underlay the ripple formation. Nevertheless "for every complex problem there is a simple solution, and it is wrong" (H.L. Mencken 1880–1956), so that we have first to ask, what an exact approach looks like. This means to start with microscopic treatment in which the dynamics of individual sand grains is taken into account.

In principle such a system is described by the combination of established equations and laws; the Navier-Stokes equation (i.e., for turbulent fluid flow the Reynolds–Averaged Navier Stokes Equations with turbulent closure model) and hard core interaction between grains (i.e., balance of forces on single particle). Figure 0.1 shows the interrelations which have to be considered (Leeder 1980). First the shear stress caused by turbulent flow is responsible for the sediment transport over the bed. Different transport rates changes the bedform which in turn retroact with the flow field. Furthermore, a layer of moving sand tends to dampen the flow turbulence. Due to gravity the sediment transport is also directly influenced by the shape of the bedforms. If taking all these effects into account (if that is possible at all, since the correct way of coupling sediment particle movement and fluid flow dynamics is not known) it is clear that a huge amount of computation is needed. Nishimori et al. (1998) states, even if this could be done, we must not forget that most computational resources are wasted in this case to compute the motions we are not at all interested in. Another question is what can we

learn if we reproduce ripples on a microscopic scale? Beside the important conclusion that it is feasible, we do not have necessarily a better understanding of the investigated phenomenon i.e., how ripple patterns occur on the macroscopic scale.

The aim of the thesis presented here approaches the problem in a different manner. It is necessary to find a way to relate the sand transport over sand ripples to bed surface properties, such as height, inclination, and curvature. We will call it parameterization of the fluid flow, which should extract the essential factors that significantly control the evolution process of ripples. Our model describes the sediment transport on a space–time scale much larger than the elementary processes. We focus on the average effect of elementary grain moves on the bedform surface. Hence the large scale dynamics of ripples is in our field of view and we are neither interested in the reproduction of single grain dynamics nor in exact flow field simulations. The purpose of the model is to clarify basic questions about initiation, evolution, and final states. Anderson (1996) argues that given today's computational power, it is relatively simple to set up and run models that embed abstracts of geomorphic processes. We follow him that the effort lies in interpreting the results by pulling out global conclusions from a set of model runs. Therefore we keep the number of control parameter minimal to find the most simple, effective macroscopic description.

Typical questions concerning pattern forming systems are: Why did the system evolve to this pattern? How stable is the result, and how sensitive is the final pattern to the initial conditions? What sorts of quantities do we have to measure in the field so that it helps our understanding at this ripple scale? These questions are investigated in the next chapters. Beginning with the phenomenon 'ripple' and an experimental setup, a basic approach of our model is explained in Chap. 2. The theory and principle features of the model are presented in Chap. 3, whereby Chap. 4 is about the numerics. Our results are investigated and discussed in Chap. 5.

1. Ripples

This chapter provides a general survey of the experimentally received knowledge about subaqueous sand pattern, especially ripples. An excursus is up to aeolian sand pattern, since similar patterns like aeolian impact ripples (see Figure 1.5) and subaqueous vortex ripples (Sect. 1.3) could have in detail very different formation processes. Furthermore aeolian phenomena were first considered in modeling, which gave the motivation to extend it to subaqueous pattern formation in this thesis.

1.1 Subaqueous Bedforms

Subaqueous bedforms can be observed in rivers and in the sea, particularly the coastal zone. They can form if water flows over granular material. The fluid flow is mostly turbulent and the grain size has to be in a order of magnitude that entrainment is possible. Bedforms which grow under the oscillatory flow condition of a coastal environment show more symmetry concerning their profile than bedforms created by unidirectional river flow. They differ a lot regarding the three dimensional patterns (Hansen et al. 2001).

Figure 1.1 shows schematically a characteristic ripple profile created on a river bed. The lee slope is steep, usually equal to the angle of repose $(30° - 32°)$ and the stoss side is flatter often below $10°$. The two hopping grains in Fig. 1.1 indicate the increasing sediment transport capacity towards the crest, due to accelerated average fluid flow (see the three arrows). The ripple migrates downstream and preserves its shape, since all sediment eroded on the stoss side is deposited behind the crest. Avalanches adjust the slope on the lee side accordingly.

To describe the shape of ripples two quantities are widely used: the vertical form index and asymmetry index (for definition see also Fig. 1.1).

> *Vertical form index:*
> Ratio between wavelength λ and height H, also called ripple index.
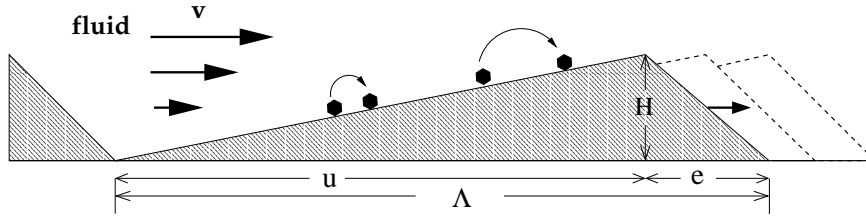> $$i := \frac{\Lambda}{H}$$

Fig. 1.1. Definition of the vertical form index $i = \frac{A}{H}$ and the asymmetry index $A := \frac{u}{e}$.

> *Asymmetry index:*
> Ratio between the lengths of the horizontal projections u of the stoss side and lee side e.
> $$A := \frac{u}{e}$$

Usually river bedforms are divided into ripples, dunes, and antidunes (see Fig. 1.2). Dunes can form only in turbulent flows and are related to water depth. No assertion on this score can be made with regard to ripples. Subaqueous dune formation is supposed to be most comparable to the development of aeolian dune pattern. For froude number $Fr > 0.8$ (see definition below), standing waves occur on the free surface of an open channel flow. The surface wave interacts strongly with the river bed so that antidunes are built, which are in phase with the surface wave. Antidunes are best understood of all bedforms (Blatt et al. 1980). The name comes from the peculiarity that antidunes could migrate upstream. In fact they also migrate downstream and sometimes even stop moving. Antidunes can only be found in unidirectional open water flow and the wavelength Λ is directly related to the mean flow velocity U ($U^2 = \frac{g\Lambda}{2\pi}$).

> *Froude number:*
> dimensionless quantity, which denotes the ratio between the forces of inertia and the gravity in a viscous fluid. h_w is the water height and u the average flow velocity.
>
> $$Fr := \frac{u}{\sqrt{h_w \|\boldsymbol{g}\|}}$$

Beyond the threshold of sediment transport, two regions remain without pattern formation, the lower– and the upper–stage plane. The upper–stage plane is supposed to be a consequence of very high concentrations of transported sediment close to the bed, which tends to dampen turbulence (Pye 1994). For the lower–stage plane Leeder (1980) found the following explanation:
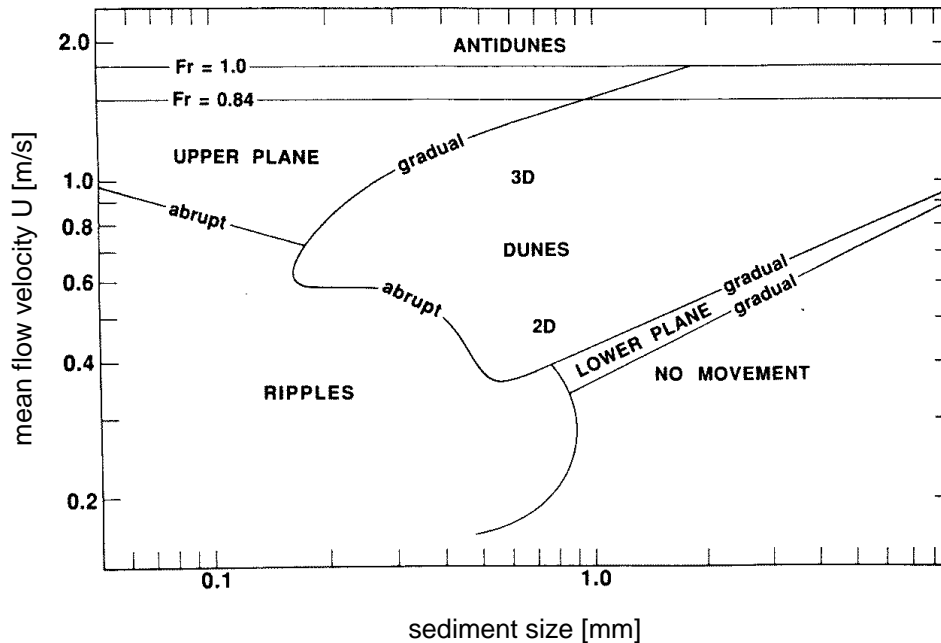
Fig. 1.2. Existence regions of bed forms (Southard and Boguchwal 1990). The diagram consists of experimental data from different authors and has a more qualitative character. To eliminate the influence of the different parameters, the average mean velocity was rescaled for a temperature of $10°C$ (for details see Southard (1971))

> Lower–stage plane beds are a consequence of the strong, vertical turbulence that occurs over a rough boundary at velocities close to the threshold for sediment transport. This tends to inhibit the development of flow separation so that bed irregularities are not amplified and propagated downstream.

The diagram shown in Figure 1.2 is a first approach to classify subaqueous pattern formation. The aim is to find a scale–free description of the onset and the evolution of ripple formation as this is not yet known, whereby modeling approaches become important.

1.2 Experimental Setups

The most recent carefully performed experiments in artificial environments are the one from Baas (1999) considering fully three–dimensional patterns, and the one from Betat et al. (1999) concentrating on approximate two–dimensional periodic structures. Most experimental results presented here refer either to Baas (1994, 1999) or to Betat et al. (1999).
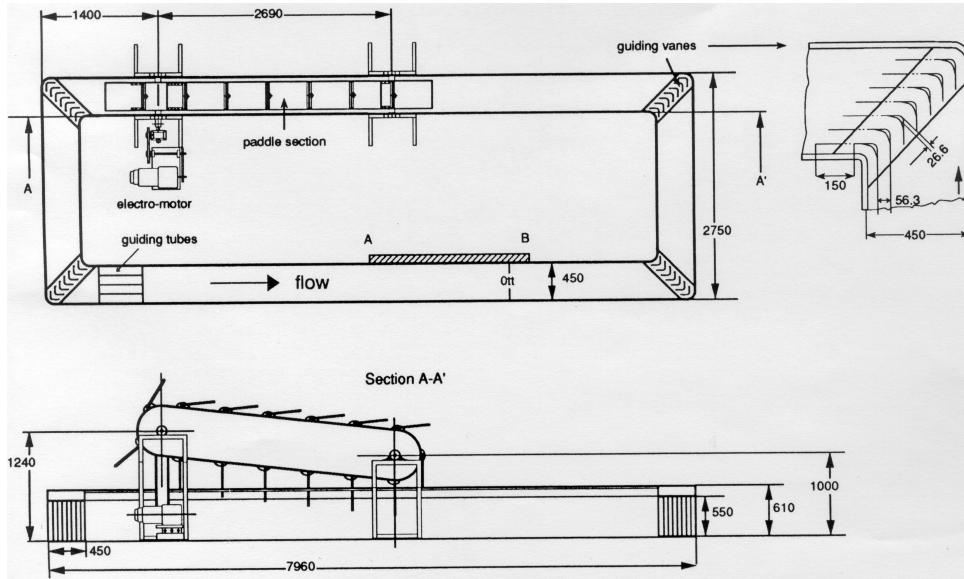
Fig. 1.3. The experimental setup from Baas (1994) and Baas (1999). Plan view and cross section of the flume. All dimensions are in millimeters. Section A-B is the transect along which bedform development was studied.

1.2.1 Recirculating Flume

A recirculating flume is the preferred setup particularly if the three–dimensionality of ripple formation is considered. All kinds of bedforms are constructible, especially antidunes, which need an open water flow.

In the rectangular flume of Fig. 1.3 the water flows in a continuous loop. The rectangular channel is 0.45 m wide and 0.61 m deep and has a maximum length of 7.96 m (Baas 1994). The depth–averaged downstream flow velocity U ranges from 0.3 to 0.9 $\frac{m}{s}$ and the flow discharge $q = U h_w$ from 0.1 to 0.4 $\frac{m^2}{s}$. Recirculating flumes often consist of only one straight channel, which must be fed with both water and sand. It is therefore difficult not to disturb the ripple dynamics especially close to the threshold where the system is very susceptible (Betat et al. 1999). Besides the costs are extraordinary to stabilize the fluid flow (guiding vanes, guiding tubes Fig. 1.3) and to achieve stationary flow condition. Therefore, if the main focus is more on reproducible flow conditions and less on three dimensionality the annular channel is the preferred experimental setup.

1.2.2 Annular Channel

The annular channel used by Betat et al. (1999) consists of two telescoped solid cylinders, which are lowered into an aquarium that is filled with water (compare Fig. 1.4). The interspace between inner and outer cylinders is filled
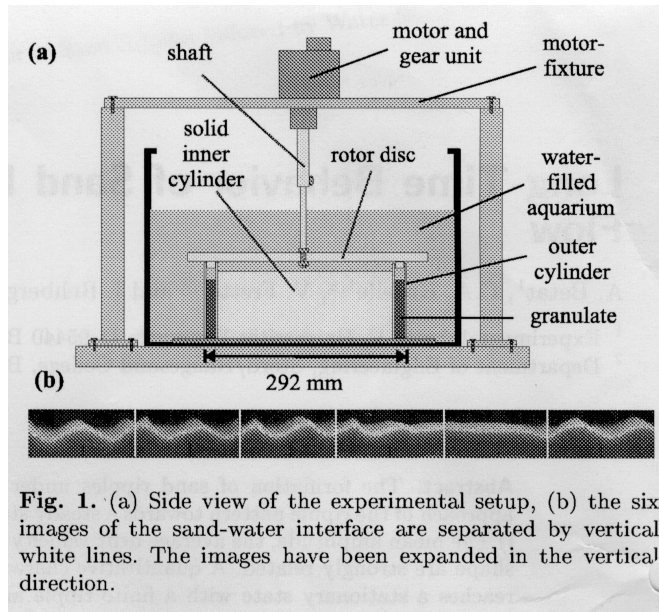
Fig. 1.4. The experimental setup from Betat et al. (1999, 2001) consists of a 15 mm wide and 58 mm high annular channel, which is filled with glass bead of density $\rho = 2.45 \frac{g}{cm^3}$. The channel is lowered into an aquarium that is filled with water to a height of 14 cm.

Fig. 1. (a) Side view of the experimental setup, (b) the six images of the sand-water interface are separated by vertical white lines. The images have been expanded in the vertical direction.

with granular material (glass beads 280–300 μm were used in the experiments of Betat et al. (1999)). To guarantee reproducible initial conditions it is important to fill the cylinder in the correct way. Simply filling it in with sand creates internal grain structures inside the sand body (contact network, arching) which can retard the beginning of sediment transport (see Grasselli and Herrmann (1997), Grasselli and Herrmann (1999)). To avoid such memory effects the sand is often caused to vibrate before the experiments. The shear flow is generated with a rotor disc above the cylinders.

This channel geometry has several advantages compared to a rectangular recirculating flume: strict mass conservation, rotational symmetry, quasi–one–dimensional geometry. These properties are especially useful for modeling the formation process because model equations mostly fulfilled mass conservation, often have periodic boundaries, and are at best quasi–one–dimensional. But the advantages also include some limitations. Due to the channel geometry only a finite number of ripples is possible. Compared to a very large system this could change the ripple wavelength. Another characteristic is that the rotor disk provides rigid boundary conditions for the water flow on the upper surface, in contrast to open water flow in a rectangular flume. As Betat et al. (2002) noted, this might influence the final size of the ripples.

1.3 Sand Ripples under Oscillatory Flow

Ripples beneath a surface wave are comparatively easy to control in the flume experiments, as their wavelength is related to the amplitude of the fluid wave. Bagnold (1941) already distinguished two types of ripples:

1. *Rolling-grain ripples* are generated when starting from a unstable flat bed and consist of small triangular ridges separated by a comparatively long stretch of flat bed (Andersen et al. 2001). They are characterized by the absence of flow separation behind the crest. They appear to be only transient or unstable patterns (Stegner and Wesfreid 1999).

2. *Vortex ripples* are characterized by the existence of vortex shedding at the crest. Experiments have shown that the wavelength Λ of the steep sand pattern is proportional to the total amplitude A of the fluid oscillation (Andersen et al. (2001) appraised $\Lambda \approx 1.3 \cdot A$) and depends neither on the frequency of the oscillations nor on the grain dimensions.

Andersen (1999) extensively investigated sand ripples formed under the action of an oscillatory flow and proposes various modeling approaches (compare Sect. 2.2). According to him the selected wavelength of rolling grain ripples has nothing to do with the selected wavelength of vortex ripples. Nevertheless they could be seen as a initial pattern in a transient process to vortex ripples, as they grow and coarsen to become vortex ripples with no flat bed between them. The growth of vortex ripples appears to be limited by the static angle of repose of the granular media (Definition (p. 9)). Also some influence by the frequency of the oscillation is determinable. The final state exhibits a strong hysteresis, whether the driving amplitude changes, and relaxation from large to small wavelengths is not possible (Stegner and Wesfreid 1999).

An important question arising in conjunction with pattern formation on sediment beds is whether the sediment transport over bedforms is reduced or enhanced compared to a flat bed. In the case of vortex this question can be answered: the presence of vortex ripples induces a higher sediment transport than for a flat bed. If superposed currents cause a net sediment transport in one direction the effect of vortex ripples is more complicated (see Andersen (1999)).

1.4 Aeolian Impact Ripples

Although the ripples in deserts (Fig. 1.5) show similarities compared with subaqueous bedforms, in particular vortex ripples, the underlying processes are rather different. The motion of grains results not directly from fluid forces imposed by the air, but rather from the impact of saltating (see below) particles that are themselves accelerated by the wind (Anderson 1987). Bagnold (1941) divided the sand transport by wind into three modes:

Fig. 1.5. Aeolian impact ripples in sand. Sierra Rosario, Mexico, Photo by Tad Nichols.

1. If the wind force acting on the sand surface is not sufficient for lifting up particles but strong enough for keeping them rolling and hopping along the surface, the transport is called *rolling* or *creeping* (Ouchi and Nishimori 1995). If this transport is caused by a rebound of saltating particles, the mechanism is also called *reptation* (Anderson (1987), Hoyle and Woods (1997), and Fig. 1.6).

2. If the power of flow is sufficient for lifting up particles, but not strong enough for keeping them in the fluid for long times, the transport mechanism is called *saltation* (Fig. 1.6). In saltating sand, grains are whipped along the surface of the sand bed by the wind, impacting the bed at small angles to the surface and with high speed (Hoyle and Woods 1997). A typical sand grain saltating in air rises steeply to a height of more than 1 cm and strikes the ground at an angle of about 10°, some 10 cm or more downwind (Blatt et al. 1980). The impacts lead to the ejection of sand grains from the bed. This impact gives "birth" to a new generation of salting particles and causes a kind of chain process.

3. *Suspended load* takes place if the acceleration acting on the particles during their motion is so strong that they are kept a long time in fluid and effects of inertia are negligible. The resulting particle traces are more random, as for saltation, where effects of inertia are more important. The mechanism is not materially different from suspension of grains in water.

However in the real process of ripple/dune formation the distinction between creep and saltation is not clear (Anderson 1987). Bagnold (1941) put forward the hypothesis, that the ripple wavelength (typically of order 10 cm) is equal to the mean length of saltation jump. Nowadays it is commonly accepted that the essential physics lies in the variation of reptation flux. The role of saltation, whose trajectories are many times longer than the ripple wavelength, is indirect (Prigozhin 1999). A model proposed by Anderson (1987) showed that the initial ripple wavelength is determined by, and several times larger than, the mean length of reptation.
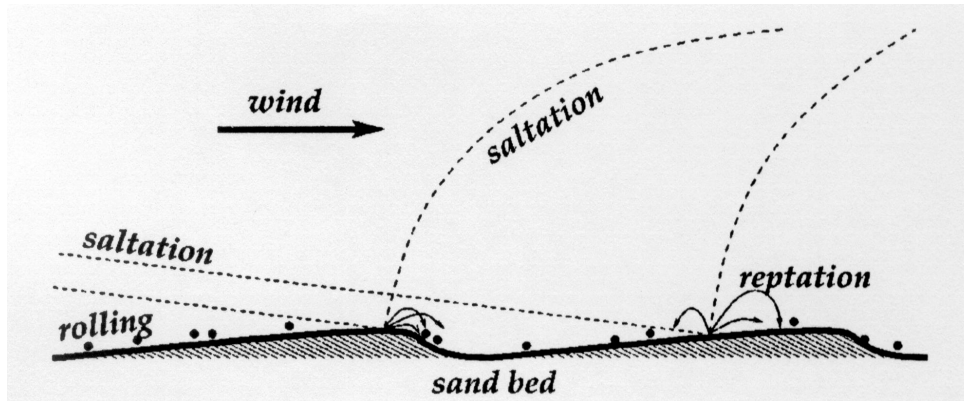
Fig. 1.6. Schematical plot of the different transport modes (Prigozhin 1999)

The *particle size segregation* is another property reported for wind-blown sand ripples. Heavy (coarse) grains accumulate on the crest on the sand ripple and light (fine) grains accumulate in the trough of the sand ripple. Following Ouchi and Nishimori (1995) the crest of the ripple is the most unstable place for the grain, so the most stable grains (heavy grains) can keep themselves at the crest of the sand ripple and vice versa for the trough. The reverse sorting is observed for water ripples. Here the coarse grains are less mobile than the finer, so that they reach the surface only in the trough, where the finer sediment is eroded (Blom et al. 2003).

1.5 Granular Matter

Many problems in modeling ripple formation arise because the sediment of the riverbed is neither treatable like a dense fluid nor as a solid body. Thus no classical boundary condition applies. Ripples consist of granular matter and the special characteristics of granular media, for example, avalanching, the angle of repose, etc. are supposed to influence strongly the pattern formation (Linz and Hänggi 1995). Let's first have a look at a granular system, without a driving fluid.
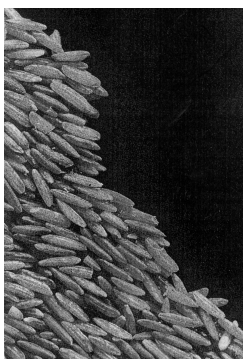
Granular matter consists of macroscopic particles of different size, shape, and surface roughness, leading to specific packing behavior: disordered structures allow compaction only in connection with reorganization of parts of the system. Due to friction, elastic vibrations, and plastic deformation, energy is dissipated, so that a system of granular particles is not in thermodynamic equilibrium (see also Luding (1997)). The left picture is a close–up photograph of a pile of rice from Frette et al. (1996).

> *Angle of repose:*
> The maximum angle at which a pile of unconsolidated material can remain stable is called angle of repose. It depends on the shape of the granule and is a characteristic property of granular media (Frette et al. 1996).

Sandpiles are the most investigated granular system, because they show almost all typical effects of granular media. The real process of pile growth is usually intermittent. Discharged granular material not only flows continuously over the pile slopes but is also able to build up under the charging point. From time to time it suddenly pours down the slope in an avalanche which redistributes the material and stops the slope from over–steepening (Prigozhin 1994).

The question of whether these system show SOC (self–organized criticality) is frequently discussed. A system exhibits SOC behavior if it tends to move into a quasi stationary state (critical state), where the distribution of event sizes is scale invariant, and where the temporal behavior is a $\frac{1}{f}$ (pink, flicker) noise (Hergarten (1998) and Hergarten (2002)). To investigate this question Frette et al. (1996) do their experiment on grains of rice, which they find to be less subject to slipping and rolling than sand grains. They report that the avalanche dynamics in the rice pile with the elongated rice A (see table 1.1) is consistent with a SOC process. For rice B the probability densities are consistent with a stretched–exponential scaling function, which do not satisfy a power–law distributed scaling. Frette et al. (1996) propose the difference in the detailed relaxation mechanisms as an explanation of the crossover from a critical to a non-critical behavior.

Name	Rice A	Rice B
Description	Unpolished (rough)	Polished (smooth)
Length	7.6 ± 0.9 mm	4.8 ± 0.4 mm
Width	2.0 ± 0.1 mm	2.4 ± 0.2 mm
Angle of repose	48.4° ± 1.2°	46.6° ± 0.8°

Table 1.1. Definition of the rice type A and B.

If we go back to the question of whether granular media influence the pattern formation, we can say that especially at the beginning of ripple formation (Sect. 1.7) the leewards avalanche process around the angle of repose and other complex intra granular interactions (see Sect. 1.2) play an important role. The effect of grain size and angle of repose on the final wavelength remains unclear. In the experiments of Betat et al. (2002) the measured angle of repose for glass beads was around 30° (sand 32°) and the measured slopes during the runs remain below this angle.
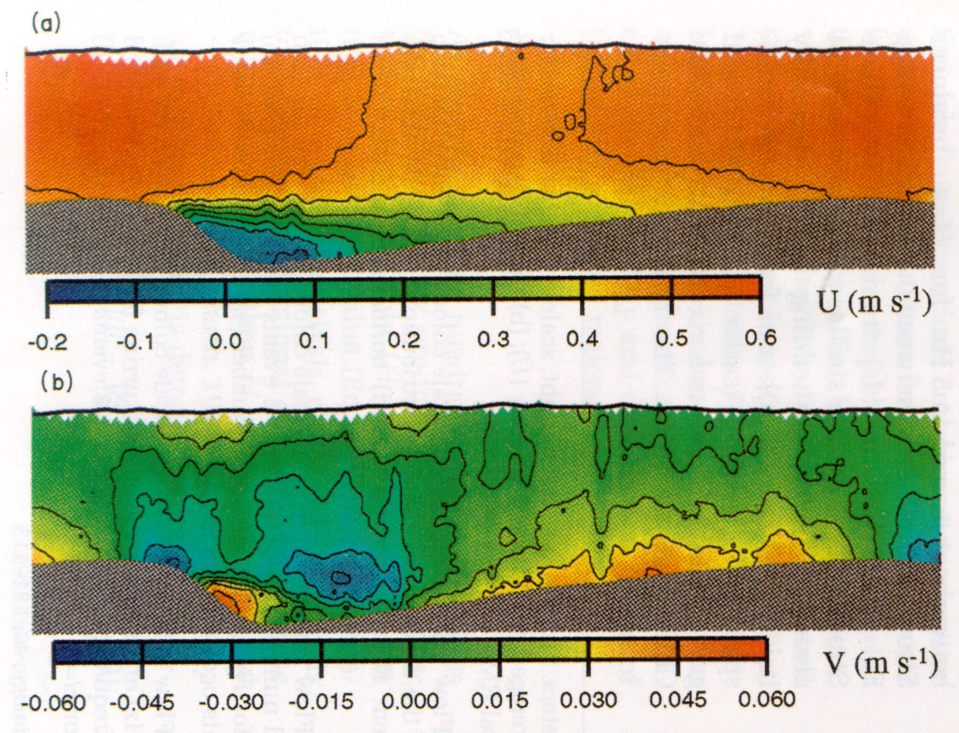
Fig. 1.7. Time-averaged downstream velocity U and vertical velocity V (Bennet and Best 1995).

1.6 Fluid Motion

Many researchers (Nelson and Smith (1989), Yalin (1992), Bennet and Best (1995), Nelson et al. (1995)) have investigated the interrelation between bedforms and flow structure. Their main focus was the measurement of average flow velocities and fluctuations along a fixed bedform (cement). Figure 1.7 shows an average flow field over fully developed bedforms (dunes) . The flow structure is schematically summarized in Fig. 1.8. Typically the flow over the crest is accelerated due to converging pattern of streamlines. The turbulent flow detaches at the ripple crest and creates a *roller* (characteristic recirculation pattern) at the lee side before it reattaches at the stoss side of the adjacent ripple. One can observe that the sediment transport ceases in the separation zone and sediment is predominantly deposited.

Three regions of different velocity profiles can be distinguished: the internal boundary layer, the wake region, and the outer region above (compare Fig. 1.8). A new internal boundary layer originates downstream of the reattachment point and reaches its maximum size over the crest. Wake flow is characterized by turbulence production one order of magnitude greater than over the stoss side. Wake current speeds are extremely low and variable in direction. The greatest downstream velocity occurs just prior to and at the
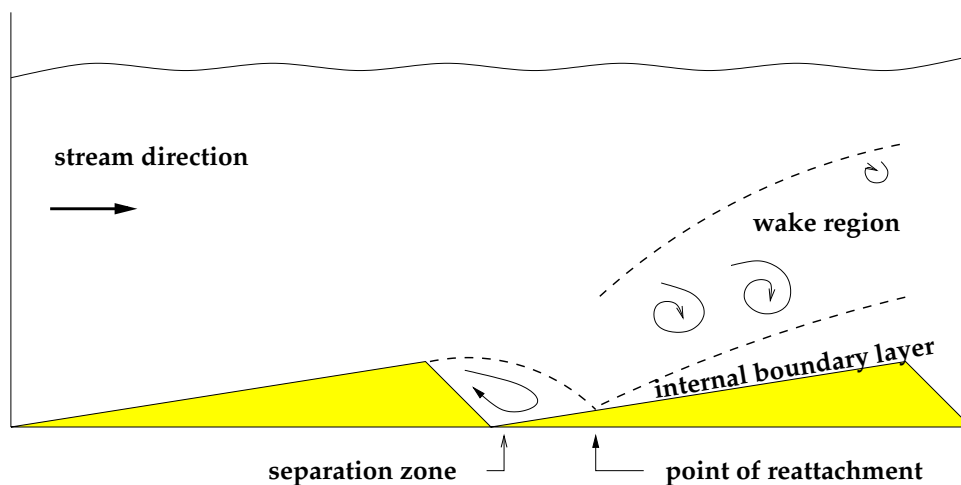
Fig. 1.8. Schematic plot of the flow structure over a ripple.

dune crest. The time–averaged vertical velocity over the dune crest is close to zero (compare Fig. 1.7). The distance from the separation point to the flow reattachment point is around 4 times the dune height. Whereas for a step, the distance is around 7 times the step height which indicates that the stoss side of ripples influence the detachment further downstream. From diffusor experiments it is known that stationary flow detachment arises for angles φ (lee slope) greater than 10°. At $\varphi \leq 5°$, there is no detachment. For fully turbulent flow, this behavior does not depend on the flow velocity (Cockrell and Markland 1963).

The flow field sensitively depends on the present profile of the sand surface and its roughness . Experiments suggest that roughness has a large effect close to the bed, reducing the longitudinal and increasing the vertical dimensions of turbulent structures (Pye 1994). At the same time, the surface profile varies in time caused by the transport of sand grains. For a given average fluid velocity the total surface resistance decreases with growing height and length of the ripple (Li and Amos 1996). For increasing average fluid velocity the total resistance of a sand surface grows until it reaches a maximum. After this maximum the surface resistance decreases again and the transition from dunes to antidunes is found (Raudkivi 1997). These observations apply to averaged quantities, but some authors emphasize the importance of instantaneous turbulent events on the sediment transport and pattern formation:

> Turbulence structures associated with the separation and reattachment process significantly affect the sediment transport field without much affecting the local bed shear stress. They do so by producing high–magnitude, low–frequency turbulence events that vary effectively sediment entrainment and movement. Significant peaks in the spatial pattern of bed load transport are therefore produced downstream of separation points, thus lending credence to the idea
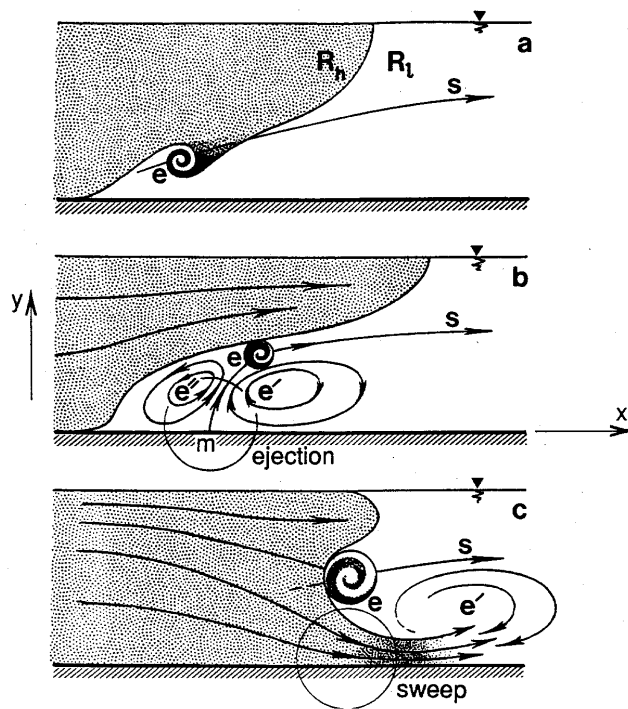
11

Fig. 1.9. Flow profile of a sequence of events during a burst cycle according to Yalin (1992). R_h and R_l stand for the high–speed and low–speed regions occurring in the body of the turbulent shear flow. s denotes the trajectory of the eddy e. e' and e'' are secondary eddies.

that flow separation plays a central role in the development of bed forms (Nelson et al. 1995).

Such a turbulent event, called burst, is illustrated in Fig. 1.9. Grass (1971) has demonstrated experimentally that bursts occur in any regime of turbulent shear flow. Yalin (1992) assumes that a turbulent shear flow contains in its body a series of large-scale *high–speed* and *low–speed* regions. He explains a burst event in the following way: eddy e (Fig. 1.9) is created at the boundary of these regions. It is formed by both low- and high-speed fluid, but the trajectory s lies completely in the low-speed region. During the process the size of e increases continually and the high–speed fluid overtakes the eddy through the gap between this eddy and the free surface (diagram b in Fig. 1.9). Together with the secondary eddies e' and e'' a process called *ejection* arises, which is able to lift up sediment from the bed surface. The next stage is that the high–speed fluid will suddenly change its configuration so as to overtake the eddy e by passing under it. This sudden and convective flow of the high–speed fluid is referred to as a *sweep*, which is also able to carry sediment from the bed.

The aim of the thesis is the parameterization of the important flow structures with regard to the sediment transport. Therefore we focus mainly on flow separation and reattachment. The influence of a single turbulent event as described above is not taken into account.
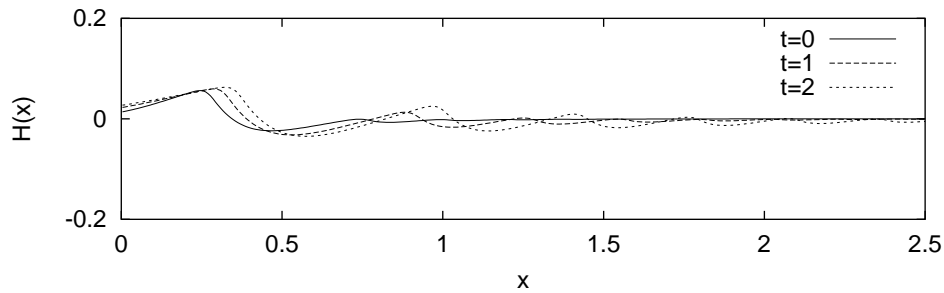
Fig. 1.10. Ripple development in the lee of an incidental ridge (profile from model results).

1.7 Initiation

Sediment ripples in flumes arise if *bedload* is the dominating transport mode. Bedload in contrast to suspended load means that grains are transported in a thin layer over the bed.

> The detachment of grains is due to the friction shear stress interacting between the flow and the bed surface; their downstream motion is due to the local flow velocities (Yalin 1992).

The beginning of turbulent fluid motion is not necessarily identical with the beginning of ripple formation. Recent experiments focus on the question of how to determine the threshold of sand movement. The growth of bedforms is indeed only observable above the threshold of motion, but evidence shows that pattern formation exists even before that in a range of grain size (Betat et al. 1999). It is generally accepted that bedforms do not grow simultaneously. In fact the growth of one irregularity induces the development of bedforms in downstream direction (Betat et al. 1999). The nucleation may be due to local inhomogeneities in the sediment density or size, randomly occurring turbulent fluid action, or inevitable deviations from a perfectly smooth sand surface (Betat et al. 2002). A possible formation scenario is described by Puls (1981):

> The starting points for bedform development are small incidental irregularities on a plane bed (height about one grain diameter). In the lee of an incidental ridge, a small separation zone with increased turbulent agitation develops. The material eroded in this zone deposits further downstream, building up a new small ridge. In this way, a range of elevations develop, whose wavelength Λ is relatively short. In the course of times, Λ increases (compare Fig. 1.10).

The properties of the developed sand waves do not depend on the nature of the geometric discontinuity. The observations show that the ripples grow fast in height and length in the beginning and reach a kind of saturation, where

they can be stable for a long period (Baas (1994), Southard and Boguchwal (1990)). In the beginning the temporal behavior can be represented by exponential growth with a growth rate σ (Betat et al. 1999):

$$H_{\max}(t) = H_{\max} \exp(\sigma t) \tag{1.1}$$

The time to reach the equilibrium state increases exponentially with decreasing flow strength (Baas 1994). The observations from Baas (1999) support the statement that initial ripple length, defined as the dominant length of the ripples to form first from flat bed, is largely independent of flow strength and primarily a function of sediment size.

1.8 Migrating Ripples

There is still confusion as to whether ripples finally stop migrating downstream or not. Williams and Kemp (1972) observed *stationary ripples*: these bedforms grew to a certain geometry and from then on remained stationary. But this observation is not supported by any recent experiments. The migration could be very slow, as the example measured by Betat et al. (1999) shows: ripples of mean amplitudes of 0.54 cm drift in *equilibrium state* with a velocity of approximately $0.09 \frac{m}{d}$ in a downstream direction (Baas 1993). For transient isolated dunes of an approximate amplitude between 3 and 14 cm Mohrig and Smith (1996) measured a migration velocity of $60 \frac{m}{d}$, which underlines the difficulties in interpretation of measurement in a natural environment far from equilibrium states. Carling and Gölz (2000) reported that the measured bedload transport rates over developing dunes in the river Rhine varies both spatially and temporally, over three orders of magnitude. But nevertheless ripples are inherently downstream migrating pattern.

Ripple speed is found to vary inversely with height, so that small ripples catch up with larger ones and merge into them (Hoyle and Woods (1997)). The relation between the height of a ripple and its migration velocity is known as the *inverse relation* and could be seen as the simple result of mass conservation. If it is assumed that the volumes q_C per width per unit time of sand crossing the crest is deposited on the lee side of the ripple, then the velocity of the ripple is given by

Inverse relation:
$$v = \frac{q_C}{H} \tag{1.2}$$

where H denotes the height of the dune (Nishimori et al. 1998). Only sand caught by the lee face contributes to the migration of a single ripple, whereas most of suspended load for example would not.

An important application area of ripple formation not yet mentioned is the reconstruction of paleo–climate and determining the depositional environment and history of sediments and sedimentary rocks. Only in cases where
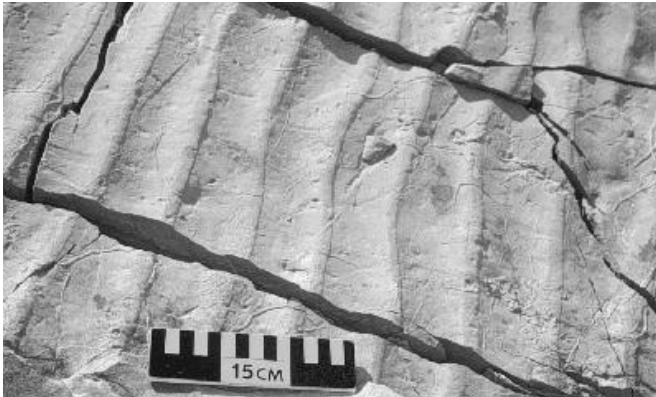
Fig. 1.11. Ancient ripple marks preserved in rock (picture from www.geo.umn.edu)

the rate of aggradation is large compared with the rate of migration of the bedforms can the bedform itself be preserved. It is chiefly the sorting, due to size segregation of the grains carried down by the avalanches which allows one cross–stratum to be distinguished from another. The sorting decreases steadily as the period of avalanching falls within the intermittent range (Allen 1970). To relate the morphology of preserved bedforms (see Fig. 1.11) to internal structures and external flow conditions, it is necessary to know the exact dynamic behavior of a ripple including migration rates and directions (Rubin and Hunter (1982), Allen (1984), Allen (1970)). A time–dependent model relating wind and sediment parameters to dune morphology would be helpful for addressing questions regarding the efficacy of using the morphology of existing dune fields as paleo–climatic indicators and for inverting the aeolian rock record to determine the details of past environmental conditions (Werner 1995).

1.9 Ripple Development

Figure 1.2 shows an attempt to classify bedforms. Southard (1971) chooses the parameter mean flow velocity U and sediment size D. But it is still an open question as to which parameter finally controls the ripple formation. Since the ripple formation retroacts on the flow field it cannot be expected to find parameters which fit likewise for initiation and equilibrium. One example may clarify this point: Betat (1999) observed that the critical shear velocity is more adequate to describe the beginning of ripple formation than a critical Reynolds number (see definitions).

Shear velocity (undisturbed):

$$u_\tau = \sqrt{\nu \frac{\partial U}{\partial y}} \qquad \left[\frac{m}{s}\right] \qquad\qquad (1.3)$$

$U(y)$: downstream velocity $\left[\frac{m}{s}\right]$
y : vertical coordinate $[m]$
$\frac{\partial U}{\partial y}$: is estimated by assuming a linear velocity profile $U(y)$
         in the middle of the channel
ν : kinematic viscosity of water at room temperature $\left[\frac{m^2}{s}\right]$

Reynolds number: Dimensionless value, which denotes the relation between inertia forces and friction forces in a viscose fluid. It characterizes the beginning of turbulent flow.

$$Re = \frac{h_w U}{\nu} \qquad\qquad (1.4)$$

h_w : water height

Betat reports that if the water height h_w is increased, the velocity U has to grow accordingly to adjust the same shear velocity (shear stress) on the bed. Thus, as the Reynolds number is not the appropriate quantity, there seems to be no correlation between the beginning of turbulent flow and the initiation of ripples. Furthermore the water height and the fluid velocity are depending parameters, because one cannot be seen without the other. Leaving the initiation process and considering subsequent ripple states, height could gain importance and is no longer a simple scaling parameter, because it also poses serious limitations on the pattern formation. Ripple dimensions become controlled by flow depth if the form roughness of the ripples extends its influence up to the water surface. At such shallow depths undulations at the water surface induce extra turbulence which extends down to the bed surface and accelerates incipient erosion of that surface (Baas 1994). Nevertheless, above this depth the dimensions of ripples are independent of flow depth. This example should underline the difficulties and the importance of finding out significant parameters.

Recently, mainly the sediment size and the shear stress are believed to dominate the equilibrium state of ripples. One experimental difficulty is the fact that the ripple formation needs a long time to reach a final state. Betat et al. (2002) measured already about 36 hours to identify a stationary state with a specific wavelength and amplitude. It became unclear whether the periodicity of the experimental setup had an influence on the selection of the final wavelength or not (see Fig. 1.12). According to Baas (1994) the time needed to develop equilibrium ripples from flat bed conditions is related to an inverse power of the flow velocity, and ranges between a few minutes
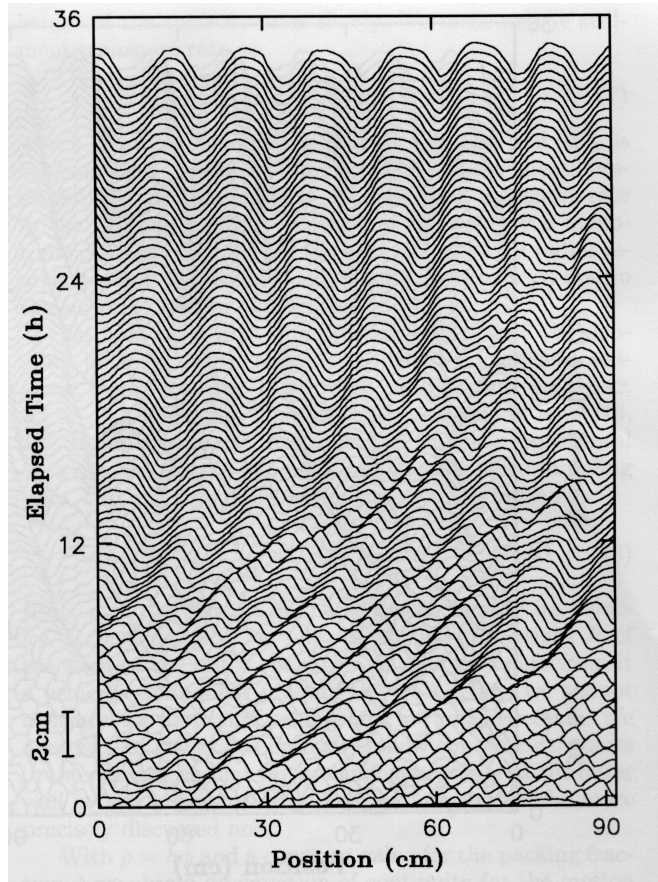
Fig. 1.12. Spatio-temporal evolution of the sand-water interface along the circumference of the channel (Betat et al. 2002). Consecutive data sets are separated 25 min in time. The scale is given at the left side of the figure.

at high flow velocities and days or weeks at low flow velocities. In most of Baas's experiments equilibrium height is reached earlier than the equilibrium wavelength because the wavelength increases more slowly than the height, particularly in the early developmental stages.

Figure 1.12 shows developing ripple profiles over time, resulting from the experiments of Betat et al. (2002). The ripple evolution is easy dividable into a transient regime, where ripples grow, diminish, and merge and into a stabilizing regime, where ripples drift slowly in the downstream direction without significant changes in the mean ripple amplitude. The procedure of stabilizing ripple height and ripple length could be understood in the following way: First the shear stress acting on the bed causes a sediment transport along the bed. The growing ripples are exposed to a drag force. The resulting form drag stress τ_d, quotient of drag force and bed area, reduces the shear stress τ_s on the bed surface, as long the total bed stress $\tau_b = \tau_s + \tau_d$ is preserved. Thus less sediment is transported along the ripples and they stop growing. Finally the shear stress is just strong enough to keep sufficient sediment on the move, that the ripples migrate only with stable amplitude and wavelength (Betat 1999). Another explanation is given by Nelson et al. (1993): The velocity
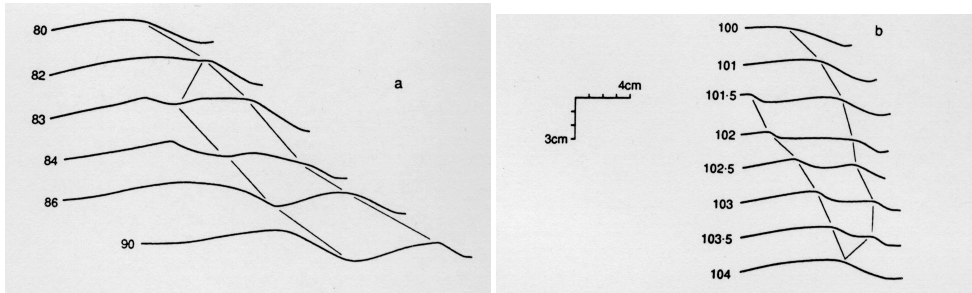
Fig. 1.13. Left diagram: convergence of two ripples. Right diagram divergence of a ripple according to Baas (1994)

near the crest increases the higher the ripple grows. They also observed that the turbulence intensity is reduced over developed ripples. Both effects tend to move the maximum of sediment transport towards the crest. Ripples stop growing if the crest corresponds to the area of maximum sediment flux. Then increasing flux on the stoss side of a ripple generates erosion and decreasing flux behind the crest deposition, whereby only migration is possible.

The evolution of ripples in the transient regime exhibit ripple interaction like merging. Baas (1994) observed similar processes in his open channel experiments (compare Fig. 1.13). He reports that the generation of new ripples occurs by the splitting of one slip face into two separate slip faces, and by sediment redistribution through local erosion and deposition on an anomalously long flat bed section. According to Baas (1994) the merging of ripples is an effect of different velocities and sheltering (named shadowing here). If a little and therefore faster ripple approaches another ripple, the fast ripple does not simply merge into the slow ripple; since the slow ripple is sheltered by the first, it loses sediment due to additional erosion and thus it's velocity increases again. It depends on the balance between the velocities if the shadowing ripple is able to overrun the sheltered ripples.

Patterns in three dimensional experimental setups (Sect. 1.2) are more complex. Measured values like ripple height, wavelength, and ripple velocity vary in strength over time and are generally more difficult to determine. A frequency distribution of the heights and wavelengths of three dimensional equilibrium ripples measured by Baas (1994) is plotted in Fig. 1.14. Since the ripple dimensions changes, even in the defined equilibrium, they are often named quasi–stationary. According to Baas (1999) ripples evolve to a quasi–stationary equilibrium in the following manner: current ripples (median grain size of 0.095 mm) always attain a linguoid plan morphology with constant average height (13.1 ± 0.6 mm) and wavelength (115.7 ± 2.4 mm) (compare Fig. 1.14). The pattern formation pass through four stages: (1) incipient ripples; (2) straight and sinuous ripples; (3) non–equilibrium linguoid ripples, and (4) equilibrium linguoid ripples (see Fig. 1.15). Baas (1999) report that every ripple shows a cyclical development. The height of a ripple develops
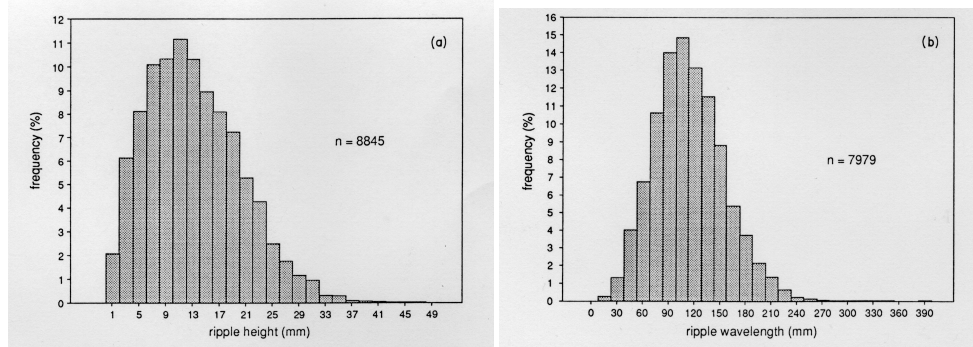
18

Fig. 1.14. Distribution of height (left diagram) and wavelength (right diagram) of equilibrium ripples (Baas 1994)
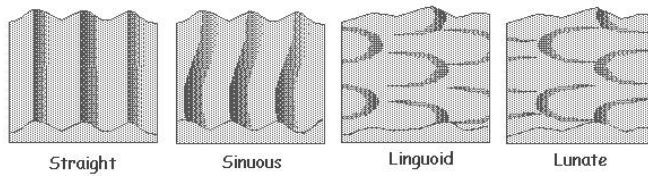

Fig. 1.15. Three dimensional pattern formation.

from zero towards a maximum value, and thereafter decreases again towards zero. This birth and death process is not identical for every ripple. This is caused by the influence of adjacent ripples that shelter downstream ripples in certain cases, and enhance downstream ripple development in others. New ripples form constantly, while existing ripples disappear. This described behavior is apparently not observable in the experiments from Betat et al. (2002) Fig. 1.12 and seems to be a feature of a complex three–dimensional ripple field.

Experimentally it is not clear which parameters could describe the final state, thus are important for the wavelength selection. Baas (1999) observed that the equilibrium ripple size and flow strength are independent. Theoretically there exists different opinions about the connection between the final wavelength of ripples and the mean particle size d (Mendoza and Zhou 1999). According to Yalin (1992) the wavelength of fully developed ripples obey the following relation:

$$\Lambda \approx 1000\,d \qquad (1.5)$$

Raudkivi (1997) found for equilibrium wavelength

$$\Lambda \sim d^{0.35} \qquad (1.6)$$

and in the beginning of ripple formation $\Lambda \sim \sqrt{d}$. The truths about the right parameter, which finally controls ripple wavelengths, are not found yet. This gives reason to further experiment work, where especially modeling approaches could provide insight in the relevance of parameter.

2. Models

The models we are dealing with focus on questions about wavelength selection, development and interaction of ripples, and stability of the final state. As examples, this chapter introduces three different approaches to model such pattern formation. A common feature of all the approaches is the need for a parameterization f of the sediment transport along the bed surface. They differ in the way of relating the sediment flux to the bed structures. Nishimori and Ouchi (1993) and Werner (1995) experimented with height $f(H)$ and slope $f(\nabla H)$ dependent approaches. A central question is, if the parameterization could simply depend on locally determinable (i.e., differential) surface attributes, or if non–local influences have to be considered.

2.1 Cellular Automata Models

A *cellular automaton* is a system which is discrete concerning space (cellular) and time, and whose evolution through time is defined by some rules and takes place in discrete steps (automaton) which are not necessarily linked to time in the physical sense (Hergarten 2002). However, it is often possible to find a transition between a discrete cellular automata model and a continuous formulation.

A cellular automata model was used by Nishimori and Ouchi (1993) and Werner (1995) to investigate ripples formed by wind–blown sand. This model is called *coarse grain models*, because one cell of the lattice corresponds to an area of the ground sufficiently larger than an individual sand grain. In other words it contains more than one sand particle. At each cell a field variable H_{ij} is allocated to denote the average height of the sand surface within the cell. The evolution of H_{ij} at one time step does not express the movement of individual sand grains. It rather describes the resulting surface height change after the collective motion of many grains during the unit time period. The time step has to be sufficiently shorter than the characteristic time of a ripple formation but much larger than the time scale of individual sand grain dynamics (Nishimori et al. 1998).

2.1.1 Nishimori and Ouchi (1993)

The model developed by Nishimori and Ouchi (1993) has some similarities
with the approach presented in this thesis (Chap. 3): the degree of abstraction
in determining the parameterization of the sediment transport, and the way
to sum up the processes which destroy pattern in a diffusional term. However,
since their model concerns wind generated ripples, the transport mechanism
differs in detail (Sect. 1.4). Their attention is mainly turned to the onset
mechanism and the wavelength selection of ripple formation. Nishimori and
Ouchi (1993) identify two main kinds of processes: saltation and creeping. In
creeping they also include grain movement by gravity force, when the gradient
of the sand hill where a grain landed is too steep for it to keep its position. To
realize the saltation process within the rules of a cellular automaton, a jump
length L is introduced. Nishimori and Ouchi (1993) propose two different
approaches to couple the saltation length L with the relief:

1. **Small scale dynamics** $f(H)$:

$$
\begin{aligned}
L &= L_0 + b\,H(x, y) \\
q &= \text{const}
\end{aligned}
\tag{2.1}
$$

   The jump length depends only on the surface height $H(x, y)$ i.e. the
   higher a sand particle starts the further it will fly. L_0 is a parameter
   proportional to the shear stress of the wind at the sand surface, or more
   precisely to the friction velocity of the wind on the sand surface (Kurtze
   et al. 2000). The quantity b in general depends on the average drag force
   on the grain. q denotes the height transfer, which is here preserved in
   each time–step.

2. **Large scale dynamics** $f(\nabla H)$ (Nishimori et al. 1998):

$$
\begin{aligned}
L &= \alpha\left[\tanh(\nabla H(x, y)) + 1\right] \\
q &= \beta\left[1 + \epsilon - \tanh(\nabla H(x, y))\right]
\end{aligned}
\tag{2.2}
$$

   α, β, and ϵ are positive constants. The parameter ϵ is the minimum
   quantity of sand that is displaced by saltation. The mathematical form
   $\tanh(\nabla H(x, y))$ of those relationships assumes that the local slope mainly
   controls the granular transport and tries to map the following observa-
   tions: compared to a flat area the wind velocity increases on the stoss
   side of a dune and decreases at the lee side. Around the crest a sharp
   peak of the wind velocity is observed. In spite of Eq. 2.1, the average
   transport length L now decisively depends on whether the starting point
   is on the stoss side or one the lee side of the sand hill (see Fig. 2.1).

Both approaches use the assumption, that the topography of the landing
point of grains can be ignored. The information at the takeoff point other
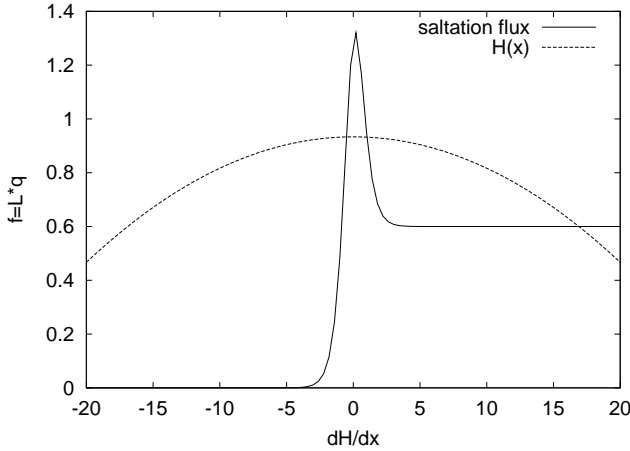than the surface height or the surface inclination are ignored as well. This

Fig. 2.1. Saltation flux $f = L \cdot q$ as a function of local slope ∇H. α and β are 1 and ϵ is 0.3. The parabola represents the corresponding surface function $H(x)$. The scales for $H(x)$ are different from ∇H and not denoted.

assumption roughly holds if the features' scale is smaller than, or at most the same as, the scale of saltation. This is just the case for wind ripple formation.

The creeping process is implemented by a diffusional term. This flux is the horizontal component of the flow which is assumed to be proportional to the gravitational force along the slope (Hoyle and Woods 1997). It does not include any bias motion in the direction of the wind. The complete model equation is based on a local conservation law of the amount of sand in the coarse grained space mesh. Thus it reads:

$$\frac{\partial H}{\partial t}(x,t) = A \left[\underbrace{N(\xi)\frac{d\xi}{dx}}_{\text{incoming flux}} - \underbrace{N(x)}_{\text{outgoing flux}} \right] + \underbrace{D\,\Delta H(x,t)}_{\text{diffusion}} \qquad (2.3)$$

where ξ denotes the x coordinate of the takeoff point of the grains which land at x. Between x and ξ the relation $x = \xi + L(H(\xi))$ is assumed. A is a scale parameter and D is the rate of relaxation, also called diffusivity. The diffusion allows grain flux in y–direction, too. It is the only two dimensional interaction in this model. Any transport due to saltation is in x direction.

Model One reproduces two important kinds of behavior: first, ripple pattern forms spontaneously, independent of initial starting conditions and reach a stationary wavelength; second, the model shows threshold behavior, when wind force exceeds critical value. A weakness of the model is the non–physical result that while the sand grains are blown downwind (saltation to the right) the ripple pattern itself drifts upwind (simulation example Fig. 2.1.1) Kurtze et al. (2000) performed a linear stability analysis of Model One and found out, that the wavelength of the marginal mode, where the growth rate is just zero, is somewhat longer than the flight distance of a grain in saltation. In nature the observed saltation lengths are found to be much longer than the ripple wavelength (Sect. 1.4).
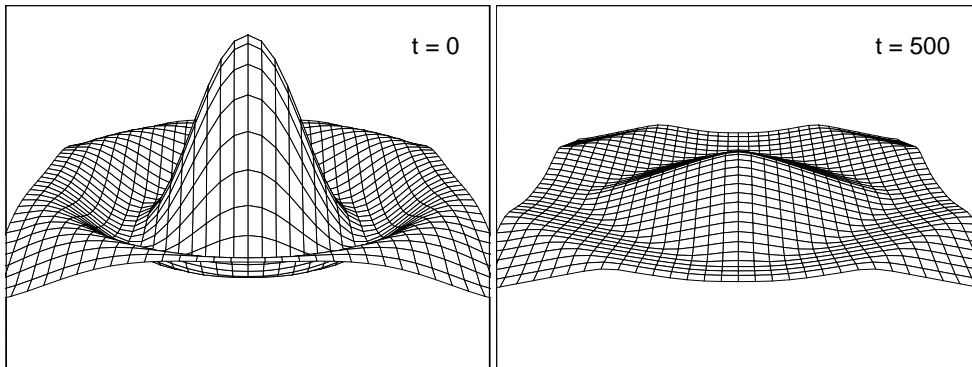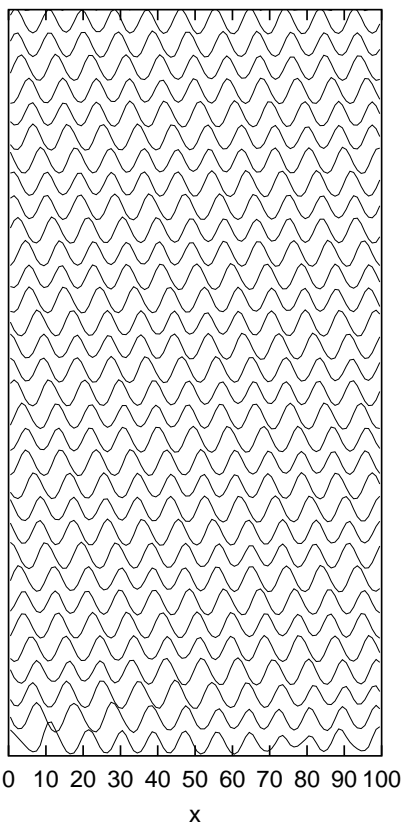
Fig. 2.2. The effect of the diffusion is that the local height of a sand hill is relaxed by gravity with a speed proportional to the convexity of the sand surface.

Calculated profiles of Model One. The profiles are plotted sequentially in time by an off-set. The ripples are moving to the left (upstream). The initial field variable $h(x)$ is set randomly with sufficiently small fluctuation around the aver-aged initial value $h = 0$. Periodic boundary conditions are used.

Model Two (Nishimori et al. 1998) shows more interesting dynamics. Two types of collision could be distinguished, when a small isolated dune catches up with a larger and slower dune: One is the perfect absorption of the smaller dune by the larger one. Through this process the average size of isolated dunes in the system increases. The second type is called tunneling, which is described as follows: the smaller dune climbs up the larger dune and, before being completely absorbed by the larger, reaches the crest of the latter, is

pushed forward, and eventually escapes from the lee side. A similar process could be observed in our model before converging of ripples (Sect. 5.6). In nature this process is not clearly confirmed, neither for wind nor for water generated ripples.

Caps and Vandewalle (2001a) performed extensive simulations by varying the parameters α, β, D and ϵ (Eq. 2.2, Eq. 2.3). They report: modifying α changes the mean ripple wavelength, while D affects the ripple index. The values taken by β and ϵ determine whether or not ripples appear. The detailed shape of the dunes depends on the combination of L and q which are experimentally difficult to observe separately. According to Caps and Vandewalle (2001b) the model leads to the unrealistic feature, that ripples become infinitely high, a problem which have arisen also in our first model (Sect. 2.3).

2.1.2 Werner (1995)

Werner and Gillespie (1993) claim that the evolution of wind ripples and other physical systems of this type cannot be modeled by either deterministic methods or spatial continuum methods. Within the developed worm model, they investigate the question, if the ripple scale evolution is dominated by the interaction and merging of ripples due to different translation velocities. Small ripples travel faster than larger ripples (Eq. 1.2). Their worm model predicts that the ripple height H (identified with the length of a worm), and therefore the spacing (for a constant shape), increases logarithmically with time. Thus they also grow infinitely.

Werner (1995) proposed another more detailed model here, the so called "slab model" for eolian dunes, where sand is transported in slabs, which consist of many grains. One grid spacing of the square lattice is equivalent to the slab size and the surface elevation is proportional to the number of sand slabs at a lattice site. As a constraint the angle between adjacent lattice sites cannot overcome the angle of repose set to 30°. The time evolution rules for this cellular automaton are as follows:

– One randomly chosen slab is moved a specified number of lattice sites l in the transport direction and is deposited at this site with a probability that depends upon the number of sand slabs there. If the slab is not deposited, then it is repeatedly moved l sites in the transport direction.
– To keep the inclination between two adjacent lattice sites less than the angle of repose, slabs are moved down the steepest gradient until compliance is achieved. This allows also slab movement perpendicular to the transport direction.
– For some simulation, Werner includes a shadow zone (to our knowledge he is the first), which means a zone behind the dune crest, where no sediment transport occurs.

To characterize the simulated dune fields Werner chooses two variables: dune orientation, angle relative to the mean transport direction and the number
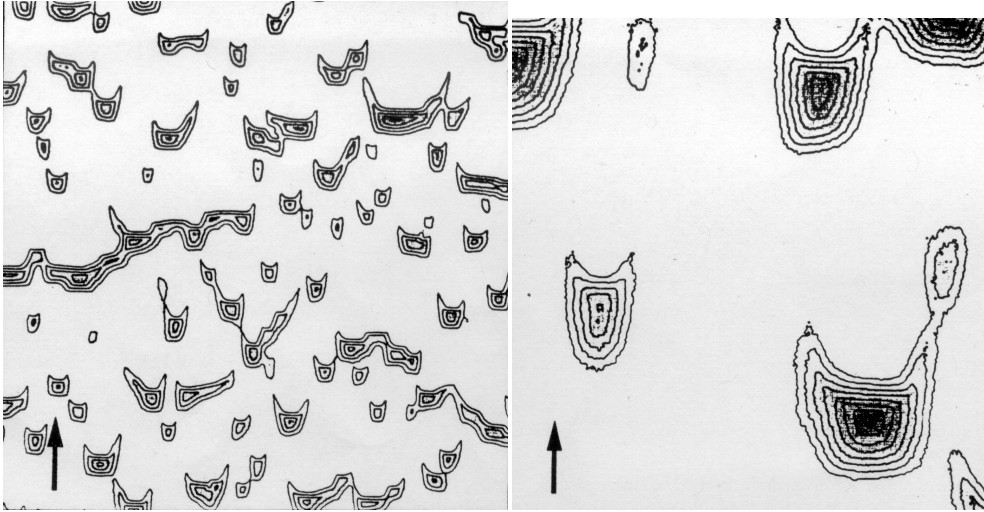
Fig. 2.3. Results from Werner (1995): Simulated barchan dune field. The arrow indicates the transport direction.

of dune-crest terminations (see Fig. 2.3). As both values tend to zero during time, which means linear dunes, and because this evolution is independent of the initial condition Werner concludes that this is due to the existence of a single attractor in the *phase space* of the system .

Both models describe situations, which are not found in natural environment. The worm model includes the assumption that there is unlimited sand supply and the slab model presumes one transport direction. Nevertheless these constraints are theoretically conceivable and show important features of the physical system behavior.

2.2 Semi–Empirical Model

The title indicates models, which contain empirically found relations. This is the case for an approach proposed by Andersen et al. (2002). They consider the wavelength selection mechanism of vortex ripple in sand (Sect. 1.3) to be one–dimensional. Therefore, they start with a discrete equation for the wavelength λ_j. The change of one ripple wavelength λ_j is, according to this approach, only a function of λ_j itself and the length of the neighboring ripples:

$$\frac{d\lambda_j}{dt} = -f(\lambda_{j-1}) + 2f(\lambda_j) - f(\lambda_{j+1}) \tag{2.4}$$

The *interaction function $f(\lambda)$* describes the transfer of mass between neighboring ripples and is extracted from the data analysis of experimental runs. Ripples, which reach zero length are removed from the system of equations.

The model is able to reproduce coarsening and saturation at a finite wavelength. Concerning vortex ripples, this is a nice reduction of complexity. Since

the shape and the growth of vortex ripples is assumed to be limited only by the angle of repose, the reconstruction of the full ripple profiles is easily done. Unidirectional current ripples are neither depending only on the close neighbors nor is their shape determinable through the known wavelength.

2.3 Continuum Model

Our approaches are continuous, which means we are able to formulate a continuous model equation in space and time, independent of any special cell size. Nevertheless the models are also coarse grain models since we do not care for single grain dynamic. In fact the particles transport is described on a "sand packet scale". The model proposed in this thesis is based on the ideas developed for our former two–dimensional model (Küpper 1999). Thus we start our investigation here with this former approach. In doing so we explain the reasons behind some basic assumptions, which are parts of the actual model too, and we will later on only refer to this section.

In addition to the approaches mentioned above, we also concentrate on the sediment transport along the bed surface, without modeling the fluid flow separately. The challenge is then to find a appropriate parameterization of the impacting fluid flow, in relation to surface properties. The results of our early numerical experiments confirm the idea to include non–local effects on the relationship between surface form and sediment transport. Thus our parameterization f is always a function of another more complex stream/shadow function W/S, which itself depends non–locally on the bed relief. Principally we divide the dynamical processes acting on a river bed into two types:

1. The *advective process*, which creates patterns. This includes mainly the average transport effect of the special water flow structures over bedforms.
2. The *diffusion process*, which destroys patterns. This process includes transport due to gravitational force as well as irregular bed particle motion, due to turbulent fluid flow. In detail these fluctuation effects around the average motion are due to turbulent changes in fluid directions, irregularities of the ripple surface, etc.. This process is assumed to be diffusive (Nikora et al. 2002).

In the former model we use the two–dimensional *master equation* for computing the changes of the surface height to model the advective part of the pattern formation (Küpper 1999):

$$\frac{\partial}{\partial t} H(\boldsymbol{x}, t) = V \left(\int \nu(\boldsymbol{y}, t) \, w(\boldsymbol{y}, \boldsymbol{x}, t) \, d^2 y - \nu(\boldsymbol{x}, t) \right) \qquad (2.5)$$

$\nu(\boldsymbol{x}, t)$ is the number of saltating particles per area and time starting at the location $\boldsymbol{x}$ at the surface; $w(\boldsymbol{y}, \boldsymbol{x}, t) d^2 x$ is the probability that a particle that

starts at the location $\boldsymbol{y}$ lands in the interval $[\boldsymbol{x}, \boldsymbol{x} + \delta\boldsymbol{x}]$. The first term at the right hand side of Equation 2.5 describes those particles which start at any location and touch down at $\boldsymbol{x}$, while the second term describes the particles starting at $\boldsymbol{x}$.

Actually saltation is not present in water environment, because of the absence of elastic collisions. Nevertheless some authors also use this term for fluid generated transport. Here the meaning of the term is more a variable transport length (capacity) than really jumping and repelling particles. Due to Equation 2.5 the sediment transport vary with the number of entrained particles $\nu(\boldsymbol{x}, t)$ and with the distribution of saltation lengths $w(\boldsymbol{x}, \boldsymbol{y}, t)$. As a first approach, we choose the saltation length to be constant and consider the influence of the fluid flow in the term $\nu(\boldsymbol{x}, t)$ which is exclusively depending on the current bed topography.

2.3.1 Lee/Stoss Effect

The basic idea is to describe the number of moved particles along the sediment bed as a kind of shadowing: for example, the shadowing is relatively strong in the separation zone where the sediment transport is reduced in consequence of the upstream ripple crest, whereas the shadowing effect ceases behind the point of reattachment (see Sect. 1.6). Thus the sediment transport at the side x depends on the situation further upstream and is therefore non–local .

For the sake of simplicity the average transport direction is chosen parallel to the x-axis of the lattice. We assume that due to the shadowing mechanism the number of moved particles over ripples is reduced compared with the number of moved particles over a flat bed. We parameterize this behavior with the water stream function $W(x)$ which varies between zero and one, so that the number of moved particles can be determined as follows:

$$\nu(\boldsymbol{x}, t) = \nu_0 \cdot W(\boldsymbol{x}, t) \tag{2.6}$$

where ν_0 is the number of moved particles for a flat bed. The function can be obtained by applying variational calculus:

$$W(x) = \left[1 - \frac{1}{\Delta} \min_{\substack{u \geq H \\ u \in C^0 \\ u(x_{max}) = H_{max}}} \left(\max_{\zeta \epsilon [x^{max}, x]} \left\{ -u'(\zeta) \right\} \right) \right]_+ \tag{2.7}$$

with u as shown in Fig. 2.4. $[\ ]_+$ denotes the positive part of the term in brackets. The function W assigns each point of the surface $H(x)$ to the derivative of $u(x)$ (see Fig. 2.5). Δ is the steepness of $u(x)$ where the particles are not moved any longer and W is equal to zero. According to W the sand transport decreases at the lee side of a ripple and increases at the stoss side of the adjacent ripple. As mentioned above, we assume that the saltation length
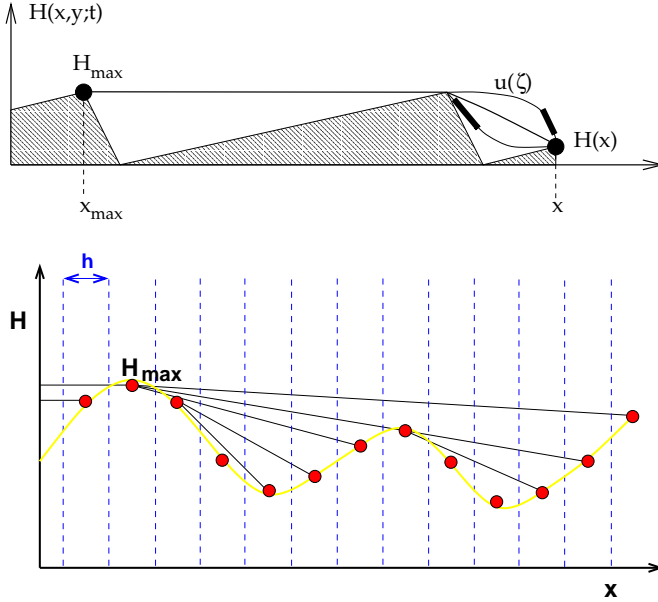
Fig. 2.4. Illustration of the variational calculus to obtain the shadow function $W(x)$. The three plots shows possible connection curves. The thick black lines denotes the sides, where the negative derivative of $u(\xi)$ reach the maximum. The middle curve solves the variational calculus.

Fig. 2.5. Resulting discrete distribution of the derivative of $u(x)$ (Definition of $u(x)$ see Fig. 2.4) along the surface $H(x)$ after the variational calculus.

l of the particles is constant. Thus the correspondent probability function $w(\boldsymbol{y}, \boldsymbol{x}, t)$ has the shape of Dirac's delta function $\delta(\boldsymbol{x} - \boldsymbol{y} - l\,\boldsymbol{e}_1)$ and Eq. 2.5 turns into:

$$
\begin{aligned}
\frac{\partial}{\partial t}H(\boldsymbol{x}, t) &= V \cdot \Big(\nu(\boldsymbol{x} - l\,\boldsymbol{e}_1) - \nu(\boldsymbol{x}, t)\Big) \\
&= V\nu_0 \cdot \Big(\underbrace{W(\boldsymbol{x} - l\,\boldsymbol{e}_1)}_{\text{Deposition}} - \underbrace{W(\boldsymbol{x})}_{\text{Erosion}}\Big)
\end{aligned}
\qquad (2.8)
$$

Hence the alteration of the sand bed height is given by the difference between the number of incoming and outgoing particles.

2.3.2 The Diffusional Processes

Equation 2.8 describes a process that creates patterns due to the lee/stoss characteristics. However, ripples observed in nature reach a quasi–stationary state with a limited height of the crest after a transient process (Baas 1999). Hence, besides constructive processes, there are also destructive influences that smooth the bed surface. We identify the following behavior: the steeper the slope, the larger the number of particles which move downhill due to rolling; moreover, avalanching occurs if the slope exceeds the angle of repose
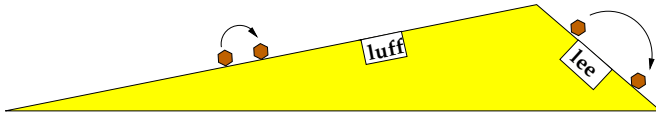
Fig. 2.6. Influence of diffusion on a constant sediment transport downstream. Longer jumps indicate higher sediment flux.

(for sand $\approx 32°$). Both processes are described by a diffusional approach for the stream density:

$$\boldsymbol{j}_d(\boldsymbol{x}, t) \quad = \quad \begin{cases} -D\left(|\boldsymbol{\nabla} H| - \tan \varphi\right) \frac{\boldsymbol{\nabla} H}{|\boldsymbol{\nabla} H|} & \text{if} \quad |\boldsymbol{\nabla} H| > \tan \varphi \\ 0 & \text{else} \end{cases} \quad (2.9)$$

with φ as the smallest angle, where rolling occurs. D denotes the diffusivity. The impact of the diffusional stream on the total sediment transport is shown in Fig. 2.6. Assuming a net sand transport to the right, the diffusion reduces the flux uphill and enhanced downhill motion. By putting Eq. 2.8 and Eq. 2.9 together, we yield eventually the governing equation of the model.

$$\frac{\partial H}{\partial t} \quad = -\mathrm{div}\,\boldsymbol{j}_d + V\nu_0 \cdot \Big(W(\boldsymbol{x} - l\,\boldsymbol{e}_1) - W(\boldsymbol{x}) \Big) \quad (2.10)$$

2.3.3 Results

To illustrate the capabilities of the model, we perform an exemplary simulation experiment (see Fig. 2.7): in the initial state we assume that the sediment bed has small random fluctuations in height. After some time, ripples begin to grow and migrate downstream, whereby little ones are captured by bigger ones. The patterns are 3-dimensional and all crests are lunate. We observe in our simulations that the development of the ripples continues until one ripple occupies the whole model region. Then only one large ripple remains and stops growing if it covers the whole sand bed (Hergarten et al. 2003).

Even if the morphology of ripples is very well reproduced by our model, the system behavior in the long run is not in agreement with experimental observation about the final state (Sect. 1.9). Hence further development is necessary (see Chap. 3). More precisely, the parameterization has to be revised. The disadvantage of the chosen stream/shadow parameterization is elaborate numerical formalism. In some extent the discretization is very special. A difficult question to answer in this context is, where does the shadow exactly start on a discrete grid? Is the cell which includes the crest inside, or outside of the shadow region, or in both? A plausible but not sole solution is described in Küpper (1999). The threshold behavior of the diffusion (limit angle φ) shows also some surprising effects. It was thought to preserve edges, because the existence of sharp crests are necessary for this kind of shadow parameterization. A look at Fig. 2.7 especially the later stages shows some edges on the stoss side in y–direction, which are artifical effects.
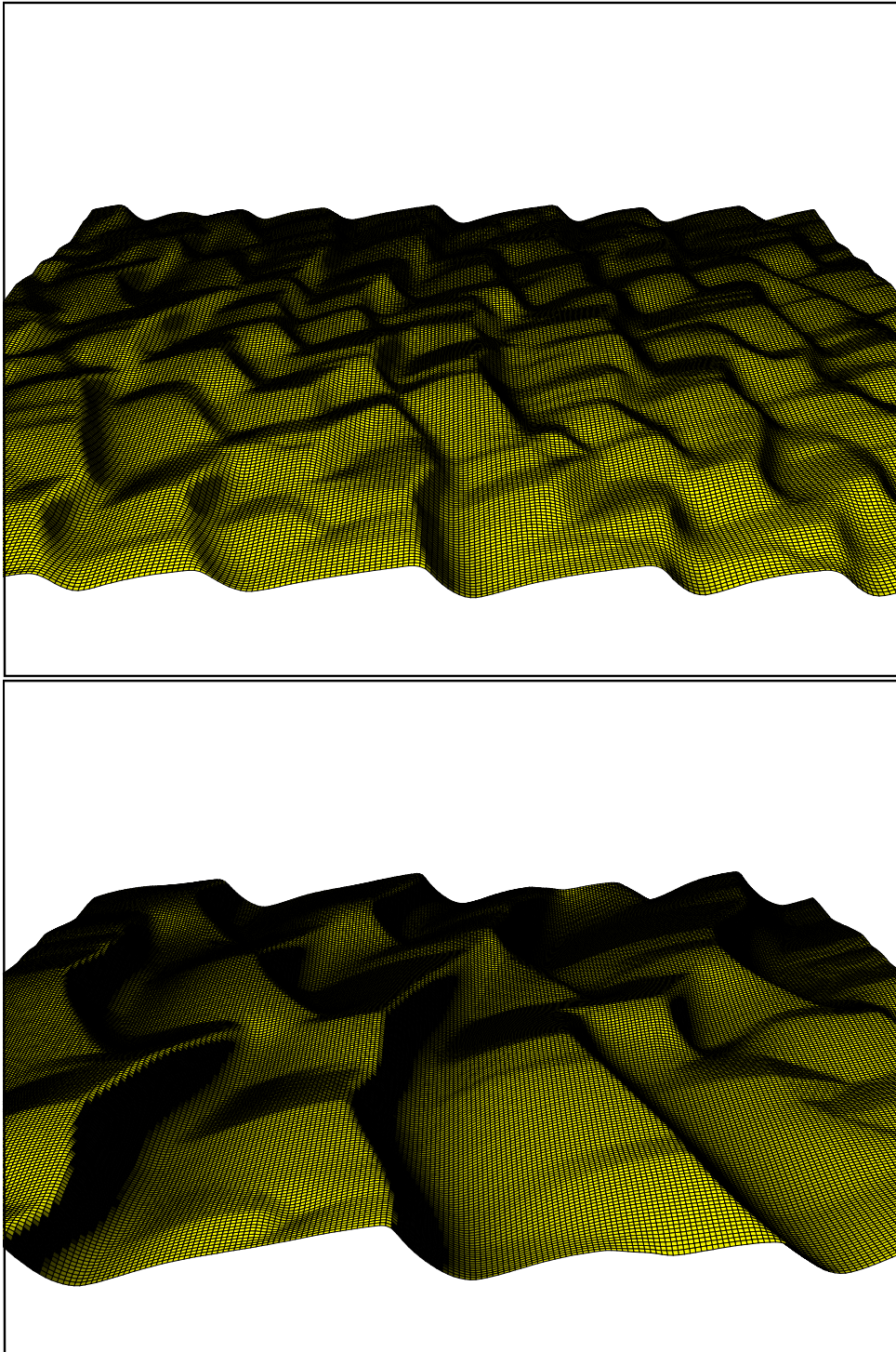
Fig. 2.7. Ripple development; $l = 1 \times$ grid spacing, $D = 10$, $V\nu_0 = 1$, $k = 1$, $\varphi = 0.1$, periodic boundary conditions.

2.4 Evaluation of Models

The models mentioned above are often called "Toy Models", because no experimental data is fitted by the numerical results. Another severe problem consists in the fact that the unknown model parameter are not accessible in experiments (in the sense that one can measure them independently). So what is the essence of these type of models?

Many authors evaluate their results through the similarity between the morphology of simulated patterns and the naturally existing patterns. This is dangerous, because as we learned during model development, there are many ways to create patterns resembling natural examples. Nishimori et al. (1998) show the linear increase of the dune migration velocity with decreasing dune height. Such observable dynamic characteristics tell more about the truth of model behind the simulation than the static morphology. Therefore the evaluation of our model is mainly based on the dynamic behavior. Otherwise the shape of simulated ripples could sometimes be helpful to calibrate model parameter (Sect. 5.4).

Another justification, which is brought up, is the fact that toy models can be used to simulate long term dynamics and answer questions regarding the development of system states. It is experimentally very difficult to achieve such situations in a natural ripple system.

3. Theory

Our new approach is a continuous sediment transport model similar to the former model proposed in Sect. 2.3. It is reduced to one dimension, because this allows deeper insight into the processes and into their mathematical features. The main idea is still to consider the influence of the fluid flow in terms which are exclusively dependent on the current bed topography. The new aspect is another even more simple approach for the shadowing S, which could be formulated in its own differential equation.

3.1 Basic Approach

We again concentrate on the coupling between main fluid flow and surface attributes. Locally determinable surface characteristics are the heights $H(x)$ and their derivatives. We consider the relation between the averaged flow and the surface curvature i.e., $\frac{\partial^2}{\partial x^2}H$ (compare Figure 3.1). The average fluid stream is at pains to follow the surface shape "as long as possible". If the curvature is too strong (negative) the fluid flow detaches. This builds a separation area of reduced fluid motion, which we call shadow zone. Later on, if the strong curvature has decreased, the main flow reattaches at the bed surface again. This behavior leads us to the assumption that the change of shadowing S along the relief is as a first approximation proportional to the surface curvature. This holds only insofar as the curvature is negative:

$$-\frac{\partial}{\partial x}S \sim \left[\frac{\partial^2}{\partial x^2}H\right]_-$$

where $[\ ]_-$ denotes the negative part of the term in brackets.
The degree of flow detachment and hence shadowing is also dependent on the upstream scenery. If a big ripple lies in front (further upstream) of a little one, the detachment at the second is weaker. A change in $S(x)$ depends therefore on the current shadowing, which could be interpreted as a memory value of the processes further upstream. The shadow decreases and thus the full fluid flow recovers according to the existing shadow. This counteracts the influence of the surface curvature on shadowing (opposite sign):
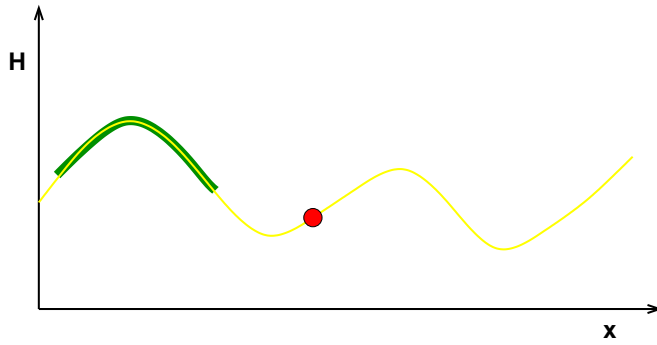
$$-\frac{\partial}{\partial x}S \sim S$$

Fig. 3.1. Schematic diagram to illustrate the relation between the bed surface $H(x)$ and the shadow function $S(x)$. The point of interest is the filled circle. The thick black line represents the area which has a shadowing effect on the point, due to the negative curvature.

Putting both processes together we get a differential equation for the shadow function $S(x)$. For the boundaries we chose periodic conditions because our considered calculation area L should be a part of a much longer bed region, where stationary flow conditions are achieved and mass conservation of the sediment holds.

$$\frac{\partial}{\partial x}S = -\mu \left[\frac{\partial^2}{\partial x^2}H\right]_- - \lambda S \qquad \text{with} \qquad S(x) = S(x+L)$$

$$
\begin{aligned}
H(x): \quad & \text{Surface height} \quad [m] \\
S(x): \quad & \text{Shadowing along x} \\
L: \quad & \text{Calculation area i.e., periodicity} \\
\mu: \quad & \text{Influence of the negative curvature, called flow strength.} \\
\lambda: \quad & \text{1/Length where the influence of the curvature has}
\end{aligned}
$$

decreased in an order of $e^{-1}\left[\frac{1}{m}\right]$. Here called inverse shadow length.

If the fluid detaches due to strong curvature, sediment is deposited and shadow increases respectively. The more the shadow changes along the surface, the more sediment is deposited or eroded. To model the evolution of the surface height through time we assume the mass conservation, which implies that the total change of the surface H is equivalent to the local change of the total stream (Eq. 3.2). Based on the shadow function the advective stream $j_a = j_a(S(x))$ is defined as:

Advective stream:

$$j_a = e^{S_{\min}-S} \quad \text{with} \quad S \in [S_{\min}, \infty]$$

The reason for inserting $S(x)$ in an exponential function follows from the intention to define the sediment transport over a plan river bed equal to

one. Thus any variation of the sediment flux due to shadowing will be in a range between zero and one. With it we avoid negative advective streams and back flow of sediment. Although back flow really occurs in the lee eddy of a ripple, it is not considered here because our approach does not account for the detailed flow structure of an eddy. Rather our parameterization of the flow derives from the shadow idea, which allows only variation of the amount of transported sand transport not of the transport direction. A principal advantage of the stream based approach above is the fact that in contrary to the former model, no discrete jump length is necessary now because no difference is made between the amount of transported particles and their transport length. This is a further simplification of the modeling approach.

The irregularities of the fluid flow, like local turbulent burst or the vertical variation (see Sect. 1.6) together with the characteristics of the granular media (avalanching effects on the lee side, see Sect. 1.5 and Sect. 2.3) are put into the diffusional stream function j_d.

Diffusional stream:

$$j_d = -d\frac{\partial}{\partial x}H \qquad\qquad (3.1)$$

$$d: \quad \text{Diffusivity} \quad \left[\frac{m^2}{s}\right]$$

In contrast to the approach of the former model the diffusional stream no longer includes a smallest angle φ, where rolling occurs. This simplifies the numerics and the interpretation of the results a lot. The angle φ inside the former model turned out to dominate the stoss slope near the crest as well as it created artifical edges along the y–direction (see Sect. 2.3). Hence simply introducing a limit angle into the system was not a way to map a behavior comparable to the angle of repose. A feature which is important in the beginning of pattern formation could be hindering in the later development stage. The diffusional stream approach of the model is again very simple and therefore poses no special limitation on the evolution of bedforms. For the total bed surface changes the advective stream j_a and diffusional stream j_d have to be added and inserted in the mass conservation equation.

$$\frac{\partial}{\partial t}H = -\frac{\partial}{\partial x}\left(j_a + j_d\right) \qquad\qquad (3.2)$$

The complete set of model equations consists of two equations: the first derived from mass conservation describing the surface evolution and the second representing the important parameterization of the fluid impact in terms of shadowing. It finally it reads:
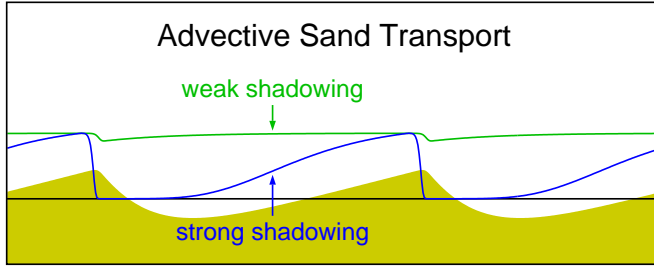
Fig. 3.3. Effect of parameter λ on the resulting advective stream j_a over developed ripples. The base line is equivalent to $j_a = 0$, where the shadowing reaches the maximum value.
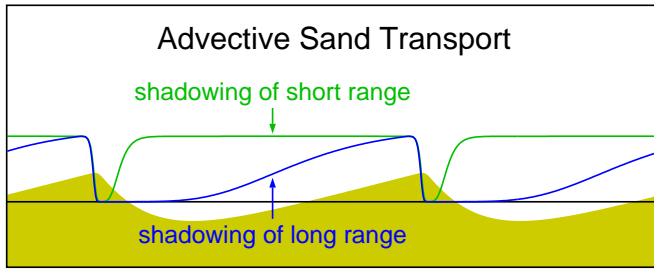
Model equations:

$$\frac{\partial}{\partial t}H \;\; = \;\; -\frac{\partial}{\partial x}e^{S_{min}-S} + d\frac{\partial^2}{\partial x^2}H \qquad (3.3)$$

$$\frac{\partial}{\partial x}S \;\; = \;\; -\mu\left[\frac{\partial^2}{\partial x^2}H\right]_{-} - \lambda\,S \qquad (3.4)$$

Boundary conditions:

$$H(x) = H(x+L) \qquad S(x) = S(x+L)$$

Three diagrams Fig. 3.2, Fig. 3.3, and Fig. 3.4 show the influence of the three parameters on the advective stream j_a and the diffusional stream j_d respectively. The proportionality factor μ could be interpreted as the average flow strength. If the flow strength is weak as in the laminar flow region, no detachment occurs at irregularities, which results in no or weak shadowing. As a consequence, the sediment transport hardly varies along the bed surface (compare Figure 3.2). The other way around, if the flow strength is strong like in the turbulent region, flow detachment is likely to occur at each obstacle. Hence the modulation of sediment transport due to shadowing rises.

The parameter λ quantifies the range of the shadowing. This is comparable to the reattachment length observed in flume experiments. High values correspond to short reattachment lengths. For low values the length to recover j_a completely increases accordingly (see Figure 3.3). The reattachment length itself is not a simply measured quantity of the fluid flow. In fact it is complex and depends on the shape of the detachment zone, on flow parameters (flow velocity, viscosity, density) and last but not least on properties
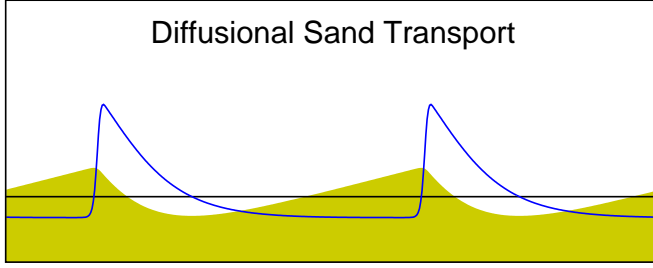
Fig. 3.4. Effect of parameter d on the resulting diffusional stream function j_d. The base line is equivalent to $j_d = 0$, where the derivative of the surface is zero.

on the sediment (McLean et al. 1994). Thus the parameter λ is difficult to derive from naturally observable quantities. Nevertheless λ is a important model parameter, because it introduces a length scale. This length scale is an outcome of the non–local approach in shadowing. The sediment transport at the side x is strongly influenced by patterns further upstream and thus not simply derivable from local surface attributes, such as height, slope, and curvature.

The diffusivity d is also an average quantity and not easy to determine from naturally measured values (Nikora et al. 2002). The effect of the diffusional stream j_d is shown in Fig. 3.4. It acts in a isotropic way and since the stream is proportional to the gradient the grains are transported always downhill.

3.2 Analytical Solution

It would be desirable to find an analytic solution of the model equation system. But since Eq. 3.3 is a nonlinear partial differential equation this is a "bold venture". Equation 3.4 is more promising in finding a solution. In the following a way to solve this equation numerically is explained. The next section will present a concrete solution of the second model equation and also one for the linearized first model equation.

If $H(x)$ is given, Eq. 3.4 is an ordinary, linear, and inhomogeneous differential equation, whose solution is the linear combination of a solution of the inhomogeneous part and the solution of the ordinary part. The boundaries in our model are periodic.

$$\frac{\partial}{\partial x} S = -\mu \left[\frac{\partial^2}{\partial x^2} H \right]_- - \lambda S(x)$$

with $\quad S(x) = \underbrace{\varphi(x)}_{\text{inhomogeneity}} \underbrace{e^{-\lambda x}}_{\text{ordinary solution}}$

$$\frac{\partial}{\partial x} S(x) = \frac{\partial}{\partial x} \varphi(x)\, e^{-\lambda x} - \lambda \varphi(x)\, e^{-\lambda x} = -\mu \left[\frac{\partial^2}{\partial x^2} H \right]_- - \lambda \varphi(x)\, e^{-\lambda x}$$

37

$\implies$

$$\frac{\partial}{\partial x}\varphi(x) = -\mu \left[\frac{\partial^2}{\partial x^2}H\right]_- e^{\lambda x}$$

$$\varphi(x) = -\int_0^x \mu \left[\frac{\partial^2}{\partial x'^2}H\right]_- e^{\lambda x'}\, dx' + C \tag{3.5}$$

From the periodic boundary conditions we can derive an expression for C. L is the dimension of the calculation area and therefore equal to the periodicity, which has to be fulfilled.

$$S(x) = S(x + L)$$
$$\implies \quad \varphi(x + L) = \varphi(x)\, e^{\lambda L} \tag{3.6}$$

The differential Equation 3.4 can not be solved with periodic boundary conditions if λ is zero. Inserting Eq. 3.5 in Eq. 3.6 yields:

$$-\int_0^{x+L} \mu \left[\frac{\partial^2}{\partial x'^2}H\right]_- e^{\lambda x'}\, dx' + C = \left(-\int_0^x \mu \left[\frac{\partial^2}{\partial x'^2}H\right]_- e^{\lambda x'}\, dx' + C\right) e^{\lambda L}$$

$$C = \frac{\int_0^{x+L} \mu \left[\frac{\partial^2}{\partial x'^2}H\right]_- e^{\lambda x'}\, dx' - \int_0^x \mu \left[\frac{\partial^2}{\partial x'^2}H\right]_- e^{\lambda x'}\, dx'\, e^{\lambda L}}{1 - e^{\lambda L}}$$

$$C = \frac{\int_0^{x+L} \mu \left[\frac{\partial^2}{\partial x'^2}H\right]_- e^{\lambda x'}\, dx' - \int_L^{x+L} \mu \left[\frac{\partial^2}{\partial x'^2}H\right]_- e^{\lambda x'}\, dx'}{1 - e^{\lambda L}}$$

$$C = \frac{\int_0^L \mu \left[\frac{\partial^2}{\partial x'^2}H\right]_- e^{\lambda x'}\, dx'}{1 - e^{\lambda L}} \tag{3.7}$$

We have to ensure $e^{\lambda L} \neq 1$ so that the denominator does not remain equal to zero. This is surely true for $\lambda L > 0$, as λ and L are per definition positive. If we know $H(x)$ and thus $\left[\frac{\partial^2}{\partial x'^2}H\right]_-$ we are able to solve the shadow equation through Eq. 3.5 and Eq. 3.7. However, for a fast numerical solution another method is recommended. The one–dimensional, affine solution space can be constructed without the need for considering the boundary conditions. At the site $x = 0$ the solution of Eq. 3.4 is $S(0) = \varphi(0) = C$. C could be chosen here arbitrarily. To solve now the differential equation we need two numerically determined solutions, representing two points in the solution space. So the whole solutions line can be constructed by linear combination. Suppose that $S_0(0) = 0$ is the solution with the starting value $C = 0$ at the site 0. $S_0(x)$

denotes the complete solution for $C = 0$. The same notation is chosen for $C = 1$, hence $S_1(0)$ and $S_1(x)$ respectively. The linear combination of $S_0(x)$ and $S_1(x)$ is then the general solution of Eq. 3.4.

$$S(x) = S_0(x) + S(0)\left(S_1(x) - S_0(x)\right)$$

$S(0) = C$ is free and has to be fixed via the periodic boundary conditions.

$$S(0) = S(L)$$
$$S(0) = S_0(L) + S(0)\left(S_1(L) - S_0(L)\right)$$
$$S(0) = \frac{S_0(L)}{1 - (S_1(L) - S_0(L))}$$

$\Longrightarrow$

$$S(x) = S_0(x) + \frac{S_0(L)\left(S_1(x) - S_0(x)\right)}{1 - (S_1(L) - S_0(L))}$$
$$S(x) = \frac{S_0(x)\left(1 - S_1(L)\right) + S_0(L)S_1(x)}{1 - S_1(L) + S_0(L)} \tag{3.8}$$

Hence if two solutions $S_0(x)$ and $S_1(x)$ are known, the entire solution is easily found, remembering that periodic boundaries are required.

3.3 Linear Stability Analysis

The idea behind a linear stability analysis is to investigate how a stationary solution develops if little perturbations are superposed. Little means in this case in relation to the linearized model equations. Here we ask how an initial flat bed behaves if a sinusoidal perturbation of any wavelength is added. By considering the limits for long or short wavelength it is possible to get information about which is the most amplified wavelength dominating the solution and which wavelengths are damped. The following initial situation is chosen where A denotes the amplitude:

$$H(x) = A\frac{\sin(\frac{2\pi x}{L})}{4\pi^2} \tag{3.9}$$
$$\frac{\partial^2}{\partial x^2}H = -A\frac{\sin(\frac{2\pi x}{L})}{L^2}$$

The known surface height $H(x)$ is inserted into Eq. 3.7 for C. Since only the negative part of the second derivative of $H(x)$ is not equal to zero, the support of the integrand extends from 0 to $\frac{L}{2}$.

$$C = \frac{-\mu A \int\limits_{0}^{\frac{L}{2}} \sin(\frac{2\pi x'}{L})e^{\lambda x'}\,dx'}{L^2(1 - e^{\lambda L})}$$

Auxiliary calculation:

$$\int\limits_{a}^{b} \sin(\tfrac{2\pi x}{L})e^{\lambda x}\,dx = \frac{1}{1 + \frac{\lambda^2 L^2}{4\pi^2}} \left(\frac{\lambda L^2}{4\pi^2} \sin(\tfrac{2\pi x}{L})e^{\lambda x}\Big|_{a}^{b} - \frac{L}{2\pi} \cos(\tfrac{2\pi x}{L})e^{\lambda x}\Big|_{a}^{b} \right)$$

$$C = \frac{-\mu A}{(1 + \frac{\lambda^2 L^2}{4\pi^2})(1 - e^{\lambda L})} \left(\frac{\lambda}{4\pi^2} \sin(\tfrac{2\pi x}{L})e^{\lambda x}\Big|_{a}^{b} - \frac{1}{2\pi L} \cos(\tfrac{2\pi x}{L})e^{\lambda x}\Big|_{a}^{b} \right)$$

with $a = 0$ and $b = \frac{L}{2}$ and $K = \frac{\mu A}{1 + \frac{\lambda^2 L^2}{4\pi^2}}$

$$C = -\frac{K}{2\pi L}\frac{1 + e^{\lambda \frac{L}{2}}}{1 - e^{\lambda L}} \tag{3.10}$$

The next step is to compute $\varphi(x)$ via Eq. 3.5. Due to the behavior of the cutoff function $[\ ]_-$ it is necessary to split the solution into $0 \le x \le \frac{L}{2}$ and $\frac{L}{2} < x \le L$.

$x \le \frac{L}{2}$

$$\varphi(x) = \frac{\mu A}{L^2} \int\limits_{0}^{x} \sin(\tfrac{2\pi x'}{L})e^{\lambda x'}\,dx' + C$$

$$\varphi(x) = K\left(\frac{\lambda}{4\pi^2} \sin(\tfrac{2\pi x}{L})e^{\lambda x} - \frac{1}{2\pi L}\left(\cos(\tfrac{2\pi x}{L})e^{\lambda x} - 1 \right) \right) + C$$

$x > \frac{L}{2}$

$$\varphi(x) = \varphi(\tfrac{L}{2})$$

It is now straight forward to compute the two parts of the full solution of Eq. 3.4:

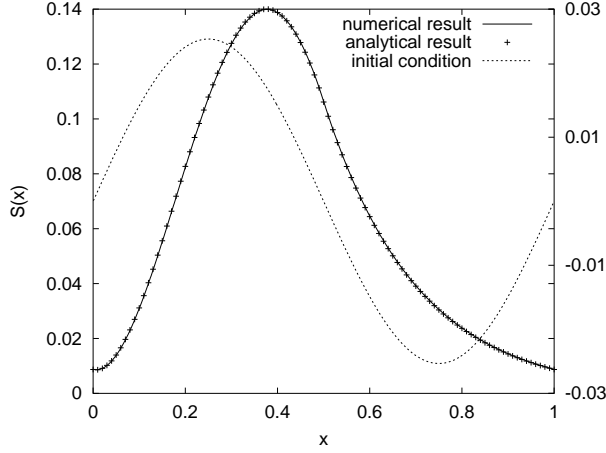$$S(x) = \varphi(x)\,e^{-\lambda x}$$

Fig. 3.5. Numerically calculated $S(x)$ in comparison to the analytical solution from Eq. 3.11 and Eq. 3.12. The slightly dotted graph is the corresponding initial sinus $H(x)$.

$x \leq \frac{L}{2}$

$$S(x) = K\left(\frac{\lambda}{4\pi^2}\sin(\frac{2\pi x}{L}) - \frac{1}{2\pi L}\left(\cos(\frac{2\pi x}{L}) - e^{-\lambda x}\right)\right) + Ce^{-\lambda x}$$

$$S(x) = \frac{K}{2\pi L}\left(\frac{\lambda L}{2\pi}\sin(\frac{2\pi x}{L}) - \cos(\frac{2\pi x}{L}) - e^{-\lambda x}\left(\frac{e^{\frac{-\lambda L}{2}} + 1}{e^{-\lambda L} - 1}\right)\right) \qquad (3.11)$$

$x > \frac{L}{2}$

$$S(x) = \left(\frac{K}{2\pi L}\left(e^{\frac{\lambda L}{2}} + 1\right) + C\right)e^{-\lambda x}$$

$$S(x) = \frac{K}{2\pi L}e^{-\lambda x}\left(e^{\frac{\lambda L}{2}} + 1 - \frac{1 + e^{\frac{\lambda L}{2}}}{1 - e^{\lambda L}}\right)$$

$$S(x) = -\frac{K}{2\pi L}e^{-\lambda x}\left(\frac{e^{\frac{\lambda L}{2}} + 1}{e^{-\lambda L} - 1}\right) \qquad (3.12)$$

The graph plotted in Fig. 3.5 is an example of the solution of $S(x)$ for the corresponding initial sinus function $H(x)$ (dotted graph). All calculations in this section are performed with the parameter values denoted in table 3.1, where N stands for the number of grid points. Figure 3.5 clearly shows that the periodicity is satisfied at the boundaries $x = 0$ and $x = L = 1$ and that $S(x)$ is always positive. The analytic solution and the numerical solution are in good agreement which proves the correct implementation of Eq. 3.4. The shadowing reaches its maximum just behind the maximum surface height. This reflects our view of the shadowing effect that behind a crest (obstacle, hill) the flow is shielded whereby sediment transport diminishes. If λ increases

N	μ	λ	d	L
1000	1	5	0.1	1

Table 3.1. Chosen parameter for numerical simulation in Fig. 3.5 and Fig. 3.6.

the length of the shadowed area is reduced, which leads to a lesser shift between the maximum of the shadow function and the maximum of the relief height. To verify this behavior we compute the maximum of S by setting $\frac{\partial}{\partial x} S$ equal zero in Eq. 3.4. Afterwards the limit $\lambda \to \infty$ is examined to find out the minimum distance between the two maxima (see above). Considering the solution of $S(x)$ it is clear that the condition $\frac{\partial}{\partial x} S = 0$ can only be met in the region $x \leq \frac{L}{2}$.

$$0 = -\mu \left[\frac{\partial^2}{\partial x^2} H \right]_- - \lambda S$$

$x \leq \frac{L}{2}$

$$0 = \frac{\mu A}{L^2} \sin\left(\frac{2\pi x}{L}\right) - \frac{\lambda K}{2\pi L} \left(\frac{\lambda L}{2\pi} \sin\left(\frac{2\pi x}{L}\right) - \cos\left(\frac{2\pi x}{L}\right) - e^{-\lambda x} \left(\frac{e^{\frac{-\lambda L}{2}} + 1}{e^{-\lambda L} - 1} \right) \right)$$

$$0 = \frac{2\pi}{\lambda L} \sin\left(\frac{2\pi x}{L}\right) + \cos\left(\frac{2\pi x}{L}\right) + e^{-\lambda x} \left(\frac{e^{\frac{-\lambda L}{2}} + 1}{e^{-\lambda L} - 1} \right) \tag{3.13}$$

in the limit $\lambda \to \infty$

$$0 = \cos\left(\frac{2\pi x}{L}\right) \quad \Longleftrightarrow \quad x = \frac{L}{4} \tag{3.14}$$

$H_{\max}$ is reached here for an initial sinus at the side $x = \frac{L}{4}$. Hence from Eq. 3.14 it follows that the distance between $S_{\max}$ and $H_{\max}$ tends to zero for high values of λ, which proves the decreasing shift between both maxima with increasing λ. In nature a short distance between flow detachment and reattachment causes only a weak modulation of the sediment transport, if anything. Our model also produces only small structures for increasing λ thus short reattachment lengths (results see Sect. 5.4.3). However, a kind of detachment always occurs in our model if the relief surface has irregularities and therefore locally negative curvature (concave). Experimentally detachment shows a threshold behavior (Cockrell and Markland 1963). The simplicity of our model does not account for this.

To complete the linear stability analysis we have to insert the computed $S(x)$ in the linearized Eq. 3.3 for the evolution of $H(x)$. The first order approximation of the exponential function is $1 + S_{\min} - S$. Thus Eq. 3.3 reads:
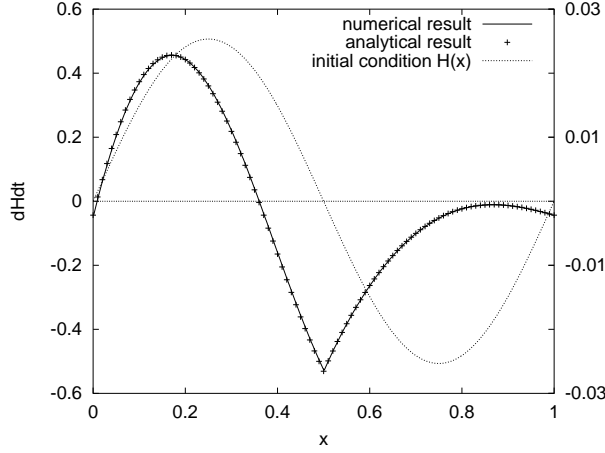
Fig. 3.6. Numerically calculated $\frac{\partial}{\partial t}H$ in comparison to the analytical solution from Eq. 3.15 and Eq. 3.16. The dotted graph is the corresponding initial sinus $H(x)$. The used parameters are denoted in table 3.1.

$$\frac{\partial}{\partial t}H = \frac{\partial}{\partial x}S - \frac{Ad}{L^2}\sin\left(\frac{2\pi x}{L}\right)$$

Substitution $\frac{\partial}{\partial x}S$ by Eq. 3.4 leads to:

$$\frac{\partial}{\partial t}H = -\mu\left[\frac{\partial^2}{\partial x^2}H\right]_{-} - \lambda S - \frac{Ad}{L^2}\sin\left(\frac{2\pi x}{L}\right)$$

It is again necessary to consider the two parted solution of $S(x)$, due to the cut–off function.

$x \le \frac{L}{2}$

$$\frac{\partial}{\partial t}H = \frac{\mu A}{L^2}\sin\left(\frac{2\pi x}{L}\right) - \lambda S - \frac{Ad}{L^2}\sin\left(\frac{2\pi x}{L}\right)$$

$$\frac{\partial}{\partial t}H = \underbrace{\frac{A}{L^2}\left(\frac{\mu}{1+\frac{\lambda^2 L^2}{4\pi^2}} - d\right)}_{a}\sin\left(\frac{2\pi x}{L}\right) + \underbrace{\frac{\lambda K}{2\pi L}}_{b}\cos\left(\frac{2\pi x}{L}\right)$$

$$+ \underbrace{\left(\frac{e^{-\frac{\lambda L}{2}}+1}{e^{-\lambda L}-1}\right)}_{c^{-}}\underbrace{\frac{\lambda K}{2\pi L}}_{b}e^{-\lambda x} \tag{3.15}$$

$x > \frac{L}{2}$

$$\frac{\partial}{\partial t}H = \underbrace{\frac{\lambda K}{2\pi L}}_{b}\underbrace{\left(\frac{e^{\frac{\lambda L}{2}}+1}{e^{-\lambda L}-1}\right)}_{c^{+}}e^{-\lambda x} - \frac{Ad}{L^2}\sin\left(\frac{2\pi x}{L}\right) \tag{3.16}$$
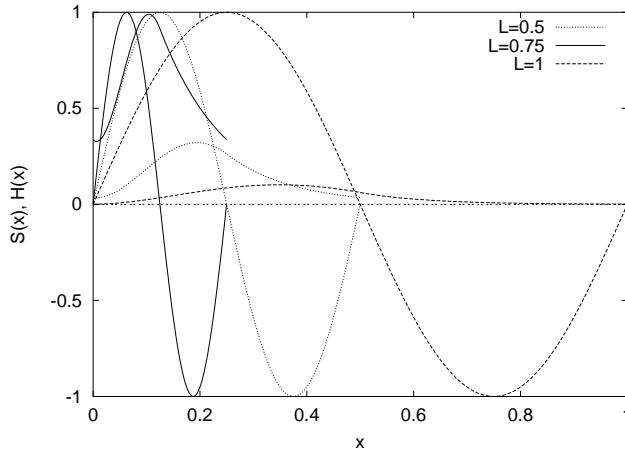
Fig. 3.7. Three sinusoidal starting conditions of different wavelengths in comparison to the belonging shadow functions.

The graph plotted in Fig. 3.6 is a calculated example of the term $\frac{\partial}{\partial t}H$. Numerical and analytical results do not differ much for little time steps. It is perhaps surprising that the point where most sediment is deposited, lies before the highest point of the initial relief which entails a backwards moving structure. This is due to the strong dependence on the first derivative of $S(x)$. It is not an unphysical result, because it is often observable that if the flow hit an irregularity the sediment is deposited in front of the crest, so that the whole structure moves first backwards. While the shape becomes more asymmetrical the structure starts moving downstream. In contrast antidunes , backwards migrating bedforms, have very symmetrical shapes, but in a longer run we do not find any stable backwards moving ripple structure as a result of our model.

Most of the graph in Fig. 3.6 is in a region of erosion (means $\frac{\partial}{\partial t}H < 0$), where the structures decays. This is because it has been calculated with a small diffusivity d. Larger diffusivity will produce more deposition, due to the convexity of the relief and higher erosion due to concavity, so that the second part ($x > 0.5$) of the plot would be able to overcome the base line and structures would grow there.

The central aspect of the linear stability analysis is how the wavelength of the starting relief influences the results. Figure 3.7 shows three initial sinus functions of different wavelength together with the belonging solutions $S(x)$.

The plots show clearly that the maximum and minimum of the shadow function increases if only the wavelength is reduced. This is also confirmed by the plot of Fig. 3.8, which shows the development of the relative maximum height of $S(x)$ and its position $x(H_{\max} - S_{\max})$ in relation to the maximum surface height $H_{max}(x)$. The distance between both maxima tend to zero for longer wavelengths L. This can be derived as follows: from Eq. 3.13 results for $L \to \infty$ that the shadow extrema fulfill $cos(\frac{2\pi x}{L}) = e^{-\lambda x}$. The exponential function tends quickly to zero and intersects the cosines near its zero point
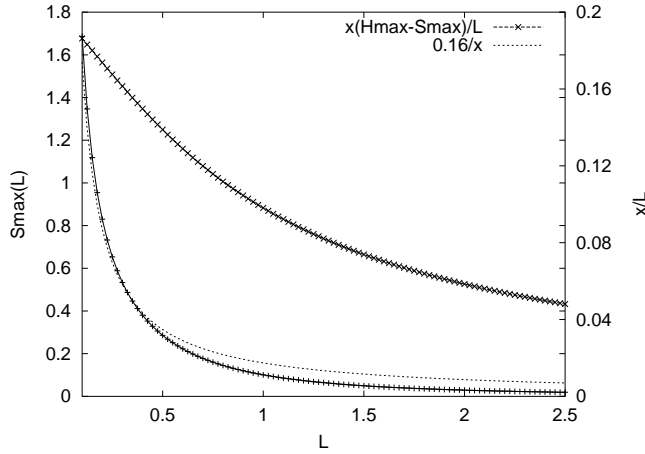
Fig. 3.8. Maximum of S in comparison to the wavelength L. The function $f(x) = 0.16\frac{1}{x}$ illustrates a similar evolution. The other plot shows the development of the relative distance (right axis $\frac{x}{L}$) between $H_{\max}$ and $S_{\max}$ in relation to L.

$(x = \frac{L}{4})$, especially if L is increased. Since the surface height is also maximal at the site $x = \frac{L}{4}$ the distance to the maximum of the shadow function tends to zero for increasing L.

The values of $S_{\max}$ itself are inversely related to L. This is comprehensible if we remember that S is according to Eq. 3.4 approximately proportional to $\frac{\partial}{\partial x}H$. Since the first derivative depends itself inversely on L (compare Fig. 3.9) this implies that $S \sim \frac{1}{L}$.
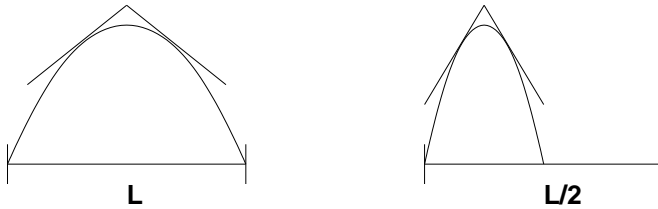
Fig. 3.9. Schematic plot of a relief structure with decreasing wavelength and the effect on the derivatives. The amplitude is preserved. The first derivative grows proportional to $\frac{1}{L}$ and the second derivative proportional to $\frac{1}{L^2}$.

Further on because $\frac{\partial}{\partial t}H$ is proportional to $\frac{\partial}{\partial x}S$ the grow of the surface height through time is in first order approximately proportional to $\frac{1}{L^2}$.

To clarify the dependency between growth rate and wavelength let us come back to the question of whether we could find some information about the stability of the model solutions. Only solution modes which are amplified contributes to the final solution. Therefore we need a quantity to measure the growth rate. Very similar to the derivation of the migration velocity (see Appendix A) we can define a growth rate, which is also based on the correlation function.

Grow rate:

$$v_g = \frac{\int\limits_{-\infty}^{\infty} \frac{\partial}{\partial t} H(x,t) H(x,t) \, dx}{\int\limits_{-\infty}^{\infty} H(x,t)^2 \, dx} \qquad (3.17)$$

The following calculation consists of inserting $H(x)$ and $\frac{\partial}{\partial t} H$ and solving the integral again for two ranges $0 \le x \le \frac{L}{2}$ symbolized with the superscript $-$, and $\frac{L}{2} < x \le L$ symbolized with the superscript $+$. It is reproducible with the help of the auxiliary calculation (see below) remembering the abbreviations.

$x \le \frac{L}{2}$

$$v_g^- = \frac{\int\limits_0^{\frac{L}{2}} \left(a \sin\left(\frac{2\pi x}{L}\right) + b \cos\left(\frac{2\pi x}{L}\right) + c^- b e^{-\lambda x}\right) \sin\left(\frac{2\pi x}{L}\right) \, dx}{\frac{A}{4\pi^2} \int\limits_0^L \sin^2\left(\frac{2\pi x}{L}\right) \, dx}$$

$$v_g^- = \frac{2\pi^2 a}{A} + \frac{4\pi c^- b}{A(1 + \frac{\lambda^2 L^2}{4\pi^2})} \left(e^{-\frac{\lambda L}{2}} + 1\right)$$

$x > \frac{L}{2}$

$$v_g^+ = \frac{8\pi^2}{AL} \int\limits_{\frac{L}{2}}^{L} \left(c^+ b e^{-\lambda x} - \frac{Ad}{L^2} \sin\left(\frac{2\pi x}{L}\right)\right) \sin\left(\frac{2\pi x}{L}\right) \, dx$$

$$v_g^+ = -\frac{2\pi^2 d}{L^2} - \frac{4\pi c^+ b}{A(1 + \frac{\lambda^2 L^2}{4\pi^2})} \left(e^{-\lambda L} + e^{-\frac{\lambda L}{2}}\right)$$

with $v_g = v_g^- + v_g^+$

$$v_g = 2\pi^2 \left(\frac{a}{A} - \frac{d}{L^2}\right)$$

Resubstitution of the abbreviations:

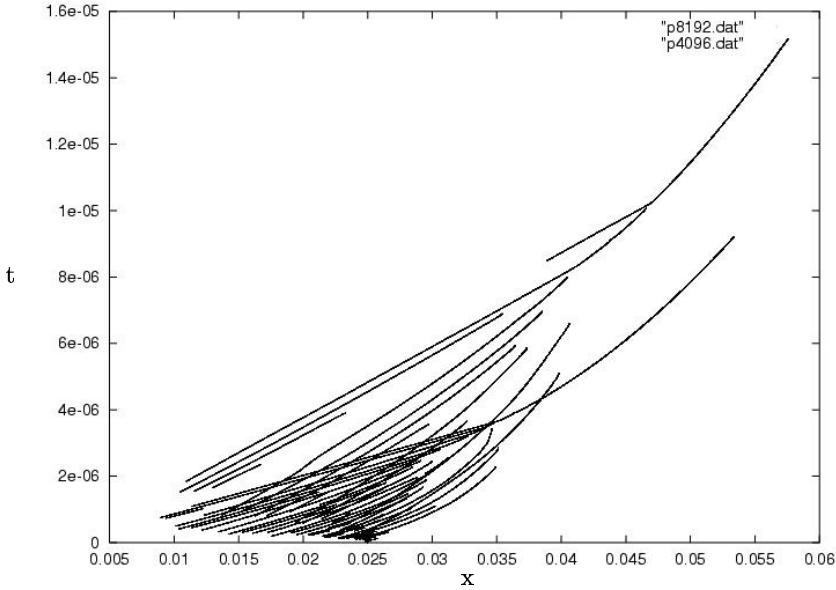$$v_g = \frac{2\pi^2}{L^2} \left(\frac{\mu}{1 + \frac{\lambda^2 L^2}{4\pi^2}} - 2d\right) \qquad (3.18)$$

Fig. 3.10. Relief maxima in space and time. The horizontal axis represents the spatial coordinates x and the vertical axis the temporal coordinates t. The upper curve is calculated for 4096 grid cells and the lower curve for 8192 grid points. The initial profile is a sinus with one period on the grid length $L = 0.1$.

As expected, the growth rate depends in the linear approximation inversely on L^2. The amplitude A does not appear in the term, because the relative change of height is independent of the initial amplitude. The difference between μ and d determines mainly whether in the beginning a structure grows or decays. Equation 3.18 gives a limit for the longest wavelength L to which L could grow. For this we have to set the growth rate equal to zero:

$$ v_g = 0 \quad \Longleftrightarrow \quad L_{\max} = \frac{2\pi}{\lambda} \sqrt{\frac{\mu}{2d} - 1} $$

The existence of a limit wavelength in the linear approximation signifies that in the early stage perturbations have no infinite range. $L_{\max} \sim \frac{1}{\lambda}$ means that the faster the shadow decays proportional to λ, the smaller the longest wavelength which just grows. But Eq. 3.18 contains no limitation for decreasing wavelengths. Even worse the smaller the wavelength L, the higher the growing rate. Thus it is inevitable that in the region where the linear approximation holds the numerical solution which depends on the grid resolution. Figure 3.10 shows this dependency on two simulations. The lower graph is calculated for 8192 grid cells and the upper one for 4096 grid cells. Both show the spatiotemporal development of the relief maximum, beginning with the initial sinus function. In the longer run the graphs are very similar to each other, hence independence of the grid resolution. In the early linear stage the number of perturbations in the case of 8192 points is twice as much

as for 4096 points, which proves that the strongest grow of the shortest possible wavelength. This attribute of the model equation is surely unphysical. Though the behavior is quickly caught by the non–linearity, the physics in the early stage has to be considered deeper in further work.

Another point which could be investigated with the help of the linear approximated solutions, is the question of whether surface patterns could move or not. To compute the migration velocity v_m we have to cross correlate the solution of $\frac{\partial}{\partial t} H$ with $\frac{\partial}{\partial x} H$. The definition reads (see Appendix A):

Migration velocity:

$$v_m = \frac{- \int\limits_{-\infty}^{\infty} \frac{\partial}{\partial t} H(x,t) \frac{\partial}{\partial x} H(x,t) \, dx}{\int\limits_{-\infty}^{\infty} \left(\frac{\partial}{\partial x} H(x,t) \right)^2 \, dx}$$

Again we consider the two parts of the solution separately and utilize the periodicity.

$x \leq \frac{L}{2}$

$$v_m^- = \frac{- \int\limits_0^{\frac{L}{2}} \left(a \sin \left(\frac{2\pi x}{L} \right) + b \cos \left(\frac{2\pi x}{L} \right) + c^- b e^{-\lambda x} \right) \cos \left(\frac{2\pi x}{L} \right) \, dx}{\frac{A}{2\pi L} \int\limits_0^{L} \cos^2 \left(\frac{2\pi x}{L} \right) \, dx}$$

$$v_m^- = -\frac{\pi b L}{A} - \frac{c^- b \lambda L^2}{A\pi \left(1 + \frac{\lambda^2 L^2}{4\pi^2} \right)} \left(e^{-\frac{\lambda L}{2}} + 1 \right)$$

Auxiliary calculation:

$$\int\limits_0^{\frac{L}{2}} \cos^2 \left(\frac{2\pi x}{L} \right) \, dx = \frac{x}{2} + \frac{L}{8\pi} \sin \left(\frac{4\pi x}{L} \right) \Big|_0^{\frac{L}{2}} = \frac{L}{4}$$

$$\int\limits_0^{\frac{L}{2}} \sin \left(\frac{2\pi x}{L} \right) \cos \left(\frac{2\pi x}{L} \right) \, dx = \frac{L}{4\pi} \sin^2 \left(\frac{2\pi x}{L} \right) \Big|_0^{\frac{L}{2}} = 0$$

$$\int\limits_0^{\frac{L}{2}} \cos\left(\tfrac{2\pi x}{L}\right)e^{-\lambda x}\,dx = \frac{1}{1+\frac{\lambda^2 L^2}{4\pi^2}}\left(-\tfrac{\lambda L^2}{4\pi^2}\cos\left(\tfrac{2\pi x}{L}\right)e^{-\lambda x}\Big|_0^{\frac{L}{2}} + \tfrac{L}{2\pi}\sin\left(\tfrac{2\pi x}{L}\right)e^{-\lambda x}\Big|_0^{\frac{L}{2}}\right)$$

$$= \frac{\lambda L^2}{4\pi\left(1+\frac{\lambda^2 L^2}{4\pi^2}\right)}\left(e^{-\frac{\lambda x}{2}}+1\right)$$

$x > \frac{L}{2}$

$$v_m^+ = -\frac{4\pi}{A}\int\limits_{\frac{L}{2}}^{L}\left(bc^+ e^{-\lambda x} - \tfrac{Ad}{L^2}\sin\left(\tfrac{2\pi x}{L}\right)\right)\cos\left(\tfrac{2\pi x}{L}\right)\,dx$$

$$v_m^+ = \frac{c^- b\lambda L^2}{A\pi\left(1+\frac{\lambda^2 L^2}{4\pi^2}\right)}\left(e^{-\lambda L}+e^{-\frac{\lambda L}{2}}\right)$$

with $v_m = v_m^- + v_m^+$

$$v_m = -\frac{\pi b L}{A} = -\frac{\tfrac{1}{2}\lambda\mu}{1+\frac{\lambda^2 L^2}{4\pi^2}} \tag{3.19}$$

As long as μ and λ are not equal to zero all initial sinus structures will move. In the linear approximation this is independent of the diffusivity d. Since μ determines the amount of transported particles, it is correct that it influences linearly the migration velocity. The right hand of Eq. 3.19 can be simplified to $\frac{2\pi^2\mu}{\lambda L^2}$ by choosing $\lambda L \gg 2\pi$. In this case the migration velocity grows for low λ values. This means that long reattachment length allows in the beginning higher migration velocities of the structure. An attended result is that the migration velocity is always negative for the symmetrical initial shape $H = \frac{A}{4\pi^2}\sin\left(\frac{2\pi x}{L}\right)$. This is a hint that the asymmetrical shape of the surface at a later date rather than the wavelength seems to be of major importance for the migration velocity.

In Fig. 3.11 the migration velocity and the growth rate is plotted in relation to the wavelength. For longer wavelengths migration velocity and grow rate converge. Hence the sinus decays as fast as it migrates upstream. Whereas shorter wavelengths move faster than they could grow or decay, besides in the diverging area ($L \to 0$. But an interpretation of these results is risky, because they are only true in the very early stage of model development. As mentioned before, the behavior for very small wavelengths does not appear to be reasonable. The linear stability analysis provides outcomes which are very useful for testing the correctness of the implementation and discretization of the model equation and gives a hint to enhanced model development concerning the sensitivity on small perturbations.
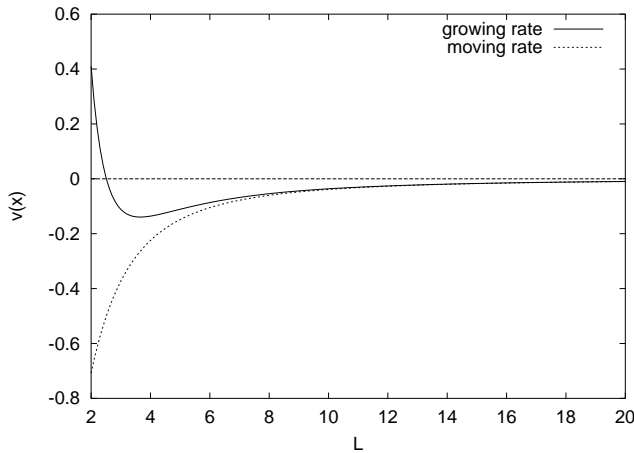
Fig. 3.11. Growing rate v_g versus moving rate v_m for a fixed set of parameter μ, λ, d along increasing L. The zero–crossing of the grow rate defines $L_{\max}$. For $L \to 0$ both graphs diverge.

3.4 Measured Data

The question of which calculated quantities could be significant for the model has to be answered carefully. On the one hand we want to use quantities which are measurable for natural ripples, like for example ripple height and vertical form index respectively (see definition (p. 1)). On the other hand these measurands should be meaningful and practically determinable from the model results. The absolute height is not practical, because it varies a lot and has to be taken from the deepest valley to the highest crest. In addition the ripple height is also not a very significant characterization of model solutions, because it is not scale independent (see Sect. 3.6). Besides, for geometric comparison with natural ripples it is useful to have a kind of ripple height. Therefore the *variance of the average ripple height* is chosen, here named h, which is more stable than the absolute height and independent of the defined base line.

$$h = \sqrt{\frac{1}{N} \sum_i \left(H_i(x) - H_{av} \right)^2} \qquad (3.20)$$

The velocity determination is necessary because it is an important feature of natural ripple systems. Again it is not sufficient to follow one ripple crest though time, if the system development is considered. Definition (p. 48) represents the term of the velocity calculated in our simulation. In the following the *migration velocity* is shortened v.

For the shape of ripples the vertical form index and the asymmetry are widely used. We concentrate on the *asymmetry index A* (definition (p. 2)) because it turns out to be independent of scaling (Sect. 3.6). To measure the wavelength the *number of maxima* is selected, shortened #max, whereby the average wavelength is easy estimated via $\Lambda_{av} = \frac{L}{\#max}$.
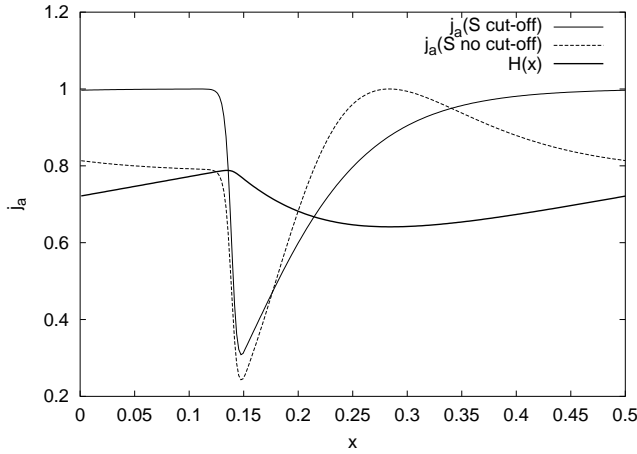
Fig. 3.12. Two advective streams over a developed ripple $H(x)$ are shown. $j_a(S\text{ cut–off})$ is based on the original shadow Eq. 3.4. $j_a(S\text{ no cut–off})$ is calculated without a cut–off function.

3.5 Non–Linearity

What is the importance of the non–linear terms in the model equations? In Eq. 3.3 the non–linearity is due to the exponential function and Eq. 3.4 is non–linear because of the cut–off function. To check the effect of the exponential function we performed simulations with a first order approximation of $j_a(S(x))$.

$$
j_a \;=\; \begin{cases} 1 + S_{\min} - S(x) & \text{if} \quad S(x) < S_{\min} + 1 \\ 0 & \text{else} \end{cases}
$$

In fact we conserve the non–linearity since a cut–off function is also introduced here. This has to be done because we want to normalize the advective stream between zero and one. The reason for that is on the one hand the basic assumption is to describe the advective sediment transport j_a according to the shadow model, which does not include back flow of sediment and negative streams respectively. On the other hand thereby we limit the maximum sediment transport rate, which corresponds to the assumption of a stationary mean flow over the ripples.

	v	h	A
lin	0.013 ± 0.0005	0.079 ± 0.0001	2.57 ± 0.0003
exp	0.015 ± 0.0006	0.051 ± 0.0001	2.42 ± 0.0002

Table 3.2. Linear shadow function versus exponential shadow function. The values height variance h, velocity v, and asymmetry A are averaged over time.

To compare the both stream functions $j_a(S(x))$, exemplary the values of the height variance h, the velocity v, and the asymmetry A are enlisted in table 3.2. The values are averaged over time and calculated for a one ripple

system. The results of the approximated stream function do not differ much from the original. It enhanced growing and asymmetry whereby the velocity is reduced. Even for bigger ripple systems the influence is poor, so that we can conclude that the exponential function is replaceable by a the cut–off function, without important effects on the simulation runs.

As mentioned the non–linearity of Eq. 3.4 is due to the cut–off function $\left[\frac{\partial^2}{\partial x^2}H\right]_-$ which allows only the concave surface to contribute to shadowing. Figure 3.12 shows the resulting advective stream j_a over a ripple with and without a cut–off. The fundamental difference is that the original advective stream reaches its maximum where the surface is concave, hence near the crest, whereby an advective stream without cut-off is maximal where the surface is convex, hence in the vale. The latter implicates new creation of structures in the lee region of the ripple. Experiments show clearly that the maximum flow strength is reached near the crest and not near the vale (Hand and Bartberger 1988), and besides we can not find a stable solution of Eq. 3.3, excluding an approach with a cut–off function.

3.6 Scaling

The aim in considering the scaling properties is to select, out of the three parameters, quantities which scale independently of each other and still describe the entire solution space of Eq. 3.3. Therefore three scaling variables a, b, c are introduced: a represents the space scaling factor, b the time scaling and c scales the height separately.

$$\tilde{x} = ax \qquad\qquad [a] = \tfrac{1}{m}$$
$$\tilde{t} = bt \qquad\qquad [b] = \tfrac{1}{s}$$
$$\tilde{H}(\tilde{x}, \tilde{t}) = cH(x, t) \qquad\qquad [c] = \tfrac{1}{m}$$
$$\tilde{S}(\tilde{x}, \tilde{t}) = S(x, t) \qquad\qquad \text{(non dimensional)}$$

The new scaled quantities are non dimensional. The idea is to identify solutions which differ only linearly in time or space by the new non–dimensional parameter. To find them, it is necessary to formulate the model equations in a non–dimensional manner:

Equation 3.3:

$$\frac{\partial}{\partial \tilde{t}}\tilde{H} = \frac{c}{b}\left(-\frac{\partial}{\partial x}S + d\frac{\partial^2}{\partial x^2}H\right)$$

$$\frac{\partial}{\partial \tilde{t}}\tilde{H} = \frac{c}{b}\left(-a\frac{\partial}{\partial \tilde{x}}\tilde{S} + d\frac{a^2}{c}\frac{\partial^2}{\partial \tilde{x}^2}\tilde{H}\right)$$

$$\frac{\partial}{\partial \tilde{t}}\tilde{H} = -\frac{ac}{b}\frac{\partial}{\partial \tilde{x}}\tilde{S} + d\frac{a^2}{b}\frac{\partial^2}{\partial \tilde{x}^2}\tilde{H}$$

$\Longrightarrow$

$$\frac{ac}{b} = 1 \qquad \tilde{d} = d\frac{a^2}{b}$$
$$b = ac \qquad \tilde{d} = d\frac{a}{c}$$

if $a = c$ is chosen:

$$b = a^2 \qquad \tilde{d} = d$$

Equation 3.4:

$$\frac{\partial}{\partial \tilde{x}}\tilde{S} = \frac{1}{a}\left(-\mu\left[\frac{\partial^2}{\partial x^2}H\right]_- - \lambda\tilde{S}\right)$$
$$\frac{\partial}{\partial \tilde{x}}\tilde{S} = \frac{1}{a}\left(-\mu\frac{a^2}{c}\left[\frac{\partial^2}{\partial \tilde{x}^2}\tilde{H}\right]_- - \lambda\tilde{S}\right)$$

$\Longrightarrow$

$$\tilde{\mu} = \frac{a}{c}\mu \qquad \tilde{\lambda} = \frac{\lambda}{a}$$

if $a = c$ is chosen:

$$\tilde{\mu} = \mu \qquad \tilde{\lambda} = \frac{\lambda}{a}$$

The measured quantities have to be transformed in the following way:

$$
\begin{aligned}
\tilde{v} &= \tfrac{a}{b}v \\
\tilde{\sigma}_h &= c\,\sigma_h \\
\tilde{A} &= A
\end{aligned}
\qquad (3.21)
$$

The asymmetry and the number of maxima are independent of scaling and in this respect a good characterization of the results. If a is chosen equal to λ Eq. 3.3 and Eq. 3.4 depends only on two parameter. For the sake of simplicity the swung dashes are ignored.

$$
\begin{aligned}
\tfrac{\partial}{\partial t}H &= -\tfrac{\partial}{\partial x}e^{S_{min}-S} + d\tfrac{\partial^2}{\partial x^2}H \\
\tfrac{\partial}{\partial x}S &= -\mu\left[\tfrac{\partial^2}{\partial x^2}H\right]_- - S
\end{aligned}
$$

In this view the parameter λ is only a space and time (remind $b = a^2$) scaling factor for the solution of the equation system.

no.	μ	λ	d	L	T	a	b	c
1	1	8	0.5	1	100	1	1	1
2	20	35	10	0.23	0.26	4.38	383	87.5

Table 3.3. Chosen parameter for two simulation runs. The first row represents the standard parameter set. L is the area size and T denotes the total run–time. a represents the space scaling factor, b the time scaling factor and c the height scaling factor.

no.	v_{calc}	h_{calc}	v	σ_h	A
1			0.049 ± 0.003	0.041 ± 2e-5	2.27 ± 0.03
2	4.3 ± 0.2	4.7e-4 ± 2e-7	4.2 ± 0.2	4.7e-4 ± 2e-7	2.28 ± 0.02

Table 3.4. Resulting measurands for simulation run 1 and 2. The subscript "calc" denotes the values calculated from the scale relations Eq. 3.21 with the scale factors of table 3.3.

A numerical check of scaling is described for two sets of model parameters μ, λ, and d in table 3.3. The first row represents the standard parameter set usually chosen. Another parameter set is denoted on the second row. In addition the respective scaling factors are also listed in row two, whereby the results of run 1 and run 2 could be identified. The resulting velocity, variance of height, and asymmetry are measured during the run and averaged over simulation time T. Again the noted deviations are in respect to the time averaged mean value. From the results of run 1 (first row) we could derive the expected values of run 2 (see first column of table 3.4) with the aid of the scale factors of table 3.3 and the scale relations (Eq. 3.21). Since the asymmetry is independent of scaling, it should be preserved in run 2. The agreement between expected values due to scaling and the measured values is well and supports the correctness of the numerical results. The asymmetry is also numerically scale independent.

4. Discretization

This chapter is written also for those, who want to implement Eq. 3.3 and Eq. 3.4. It is detailed enough to program the algorithm straightforward.

4.1 Discrete Model Equation

The discrete formulation of Eq. 3.3 and Eq. 3.4 reads:

Discrete model equation:

$$\frac{H_i^{t+\delta t} - H_i^t}{\delta t} = \underbrace{-\frac{\tilde{S}_i^t - \tilde{S}_{i-1}^t}{\delta x}}_{\text{advective transport}} + \underbrace{d\,\frac{H_{i-1}^{t+\delta t} - 2H_i^{t+\delta t} + H_{i+1}^{t+\delta t}}{\delta x^2}}_{\text{diffusivity}}$$

$$(4.1)$$

$$S_{i+1}^t = \frac{S_i^t - \delta x\,\mu\,\frac{H_{i-1}^t - 2H_i^t + H_{i+1}^t}{\delta x^2}}{1 + \delta x\,\lambda}$$

$$(4.2)$$

δx denotes the grid spacing, δt the time increment, t the total model time, and i the grid cell number. $\tilde{S}_i^t$ stands for $e^{S_{min}^t - S_i^t}$. The simplest way to model the advective stream on the right–hand side of Eq. 3.3 is to use upwind differencing, which is first order accurate in the calculation of the spatial derivatives. The idea behind this is, that a disturbance in the advective quantity $\tilde{S}$ at mesh point i should affect only mesh point $i + 1$, if the transport direction is positive (Press et al. 1995). The diffusional term in Eq. 4.1 is solved fully implicit and centered in space. It is of second order accuracy in space, hence pose no limitation to insure accuracy in spite of the advective term.

The ordinary differential Eq. 3.4 is solved implicitly for the initial values 0 and 1. The solutions are named here $S_0(x)$ and $S_1(x)$. Since the boundaries are periodic the final solution can be written as linear combination (Eq. 3.8).

$$S(x) = S_0(x) + \frac{S_0(L)\,(S_1(x) - S_0(x))}{1 - (S_1(L) - S_0(L))}$$

Eventually the equation system is coupled by an adaptive time step method.

4.2 Problem of Second Order Discretization

The proximate idea arises, to treat $S(x)$ of second order accuracy in space, too, so that the advective and diffusive stream have the same resolution in space. For this case we define S_i as the shadow in middle of node i-1 and i (see Fig. 4.1). Then the differential term is centered in space.

$$\frac{S_{i+1} - S_i}{\delta x} = -\mu \frac{H_{i-1} - 2H_i + H_{i+1}}{\delta x^2} - \lambda \frac{S_i + S_{i+1}}{2} \tag{4.3}$$

The implicit scheme reads:

$$S_{i+1} = \frac{S_i - \mu \frac{H_{i-1} - 2H_i + H_{i+1}}{\delta x} - \frac{\delta x}{2} \lambda S_i}{1 + \frac{\delta x}{2} \lambda}$$
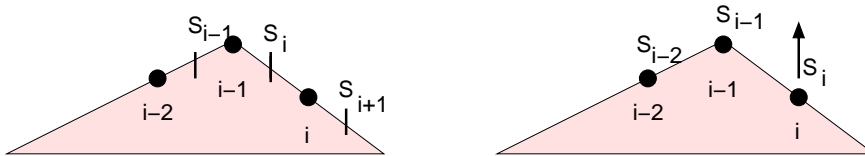
Fig. 4.1. Two definitions of the discrete shadow function around the crest in comparison. The filled circles stand for grid nodes. The arrow in the right diagram symbolized the future development of this grid node.

Figure 4.2 proves the expected higher accuracy of second order discretization because the graphs converge faster with higher space resolution. The problem arises if we try to put $S(x)$ into Eq. 4.1. Due to the new definition, $S(x)$ is shifted about half grid size to the left (if the node numbering goes to the right, compare Figure 4.1). This has to be corrected when we replace the advective term.

$$\frac{\partial}{\partial t} H = -\frac{e^{S_{min} - S_{i+1}} - e^{S_{min} - S_i}}{\delta x} + d \cdots$$

Performing some simulations based on this scheme, it comes out that the initial relief does not move. Instead it grows until a stable state is reached and remains static. The crucial point is, how the shadow function behaves at the crest. In Figure 4.1 the two different shadow approaches are schematically explained. The diagram on the left represents the definition of $S(x)$ according to Eq. 4.3, the one on the right represents the definition finally chosen. Here we can see, why the model breaks down if it is based on the symmetric definition of $S(x)$. Node i will grow proportionally to the difference $S_{i+1} - S_i$. Since both values of the shadow function lies in the lee region, they are very similar and node i does not change a lot in height. The opposite case is true
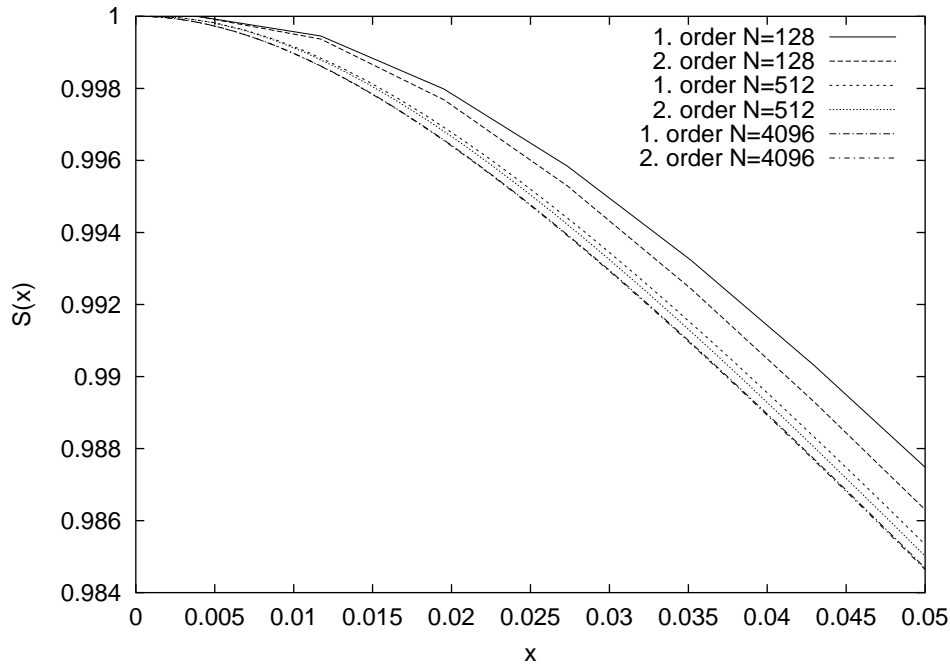
Fig. 4.2. Convergence of first order versus second order discretization of the shadow function.

for the second diagram. S_i is on the lee side, but S_{i-1} is identical with the shadow at the crest, usually around zero. Hence the difference is large and node i will grow. Consequently only in the second case migration is possible, because node i could grow and leave the shadow zone. Physically this means, that the model works only if point i is not influenced by the surface further downstream. The whole interaction has to lie upstream.

4.3 Periodic Boundaries

Periodic boundaries are nice to implement but hard to interpret. The idea behind this choice is always that the calculated area should be a cantle of a much longer region. Mass is conserved on this cantle and the average fluid flow is stationary. The problem is to decide whether the cut out area L is long enough to exclude influence through the boundaries or not.

Figure 4.3 is a plot of the three measured values h, A, and $\#$max over increasing L. The lowest graph indicates the number of maxima. $\frac{L}{\#max}$ is then the average wavelength. For $L < 1.6$ one ripple occupies the calculation area. Above $L \geq 1.5$ and below $L < 3.3$ two ripples can exist. These results are surely dominated by the boundaries because at least one side is always in contact with a boundary. Their wavelength is equal L or $\frac{L}{2}$ and is absolute stable. h increases according to L, as a result of the scaling properties. The
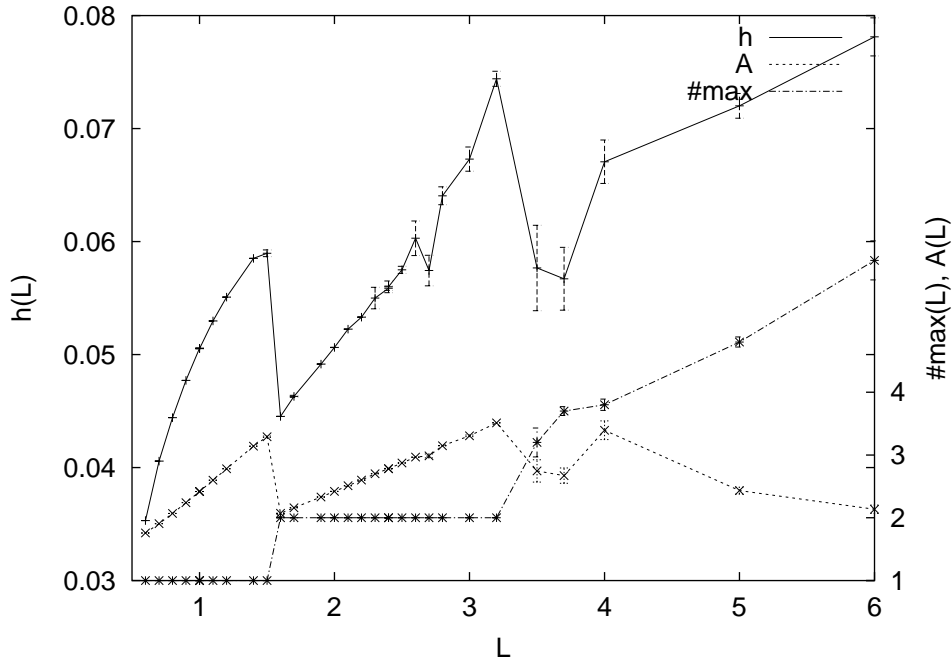
Fig. 4.3. h, A, and #max versus length of the calculation area L.

rigorously linear growth of the asymmetry inside a region of stable ripples is a hint that the solution is forced to arrange on the grid size.

For $L \geq 3.3$ the number of maxima exceeds two and the things start to be more complex, because from three ripples onwards, one of them has no contact to the boundaries and can evolve more freely. The number of maxima is not any more an integer, because the maxima vary with time and thus the mean value is in between (see Fig. 4.4). All measured average values in this region show a much higher variance, due to the less stabilizing effect of the periodicity. The wavelength varies around a mean value, which itself lies around One. Again h grows in relation to the grid size. The asymmetry seems to converge to a limit value shortly above Two. Hence the system seems to develop more freely and admittedly more unstable.

4.4 Variational Time Steps

The model consist of two equations, which have to be coupled in time. Since the advective term in Eq. 3.3 is of first accuracy in space in contrast to diffusion (of second order), we expect here the highest dependence on time step variation. Principally it is important to know that the different processes described through the equations take place on a comparable time scale. If not senseless coupling can involve needless numerical effort.

58
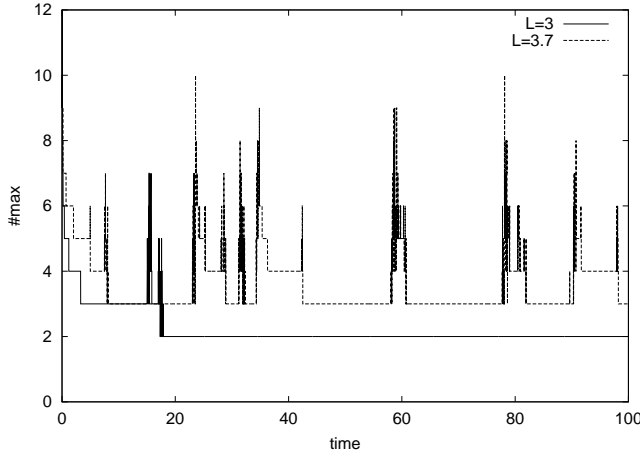
Fig. 4.4. Time evolution of number of maxima for two lengths of calculation area. $L = 3$ lies in solution set, which is dominated by the periodic boundaries and thus allows only two ripples. $L = 3.7$ represents a solution less influenced by the boundaries.
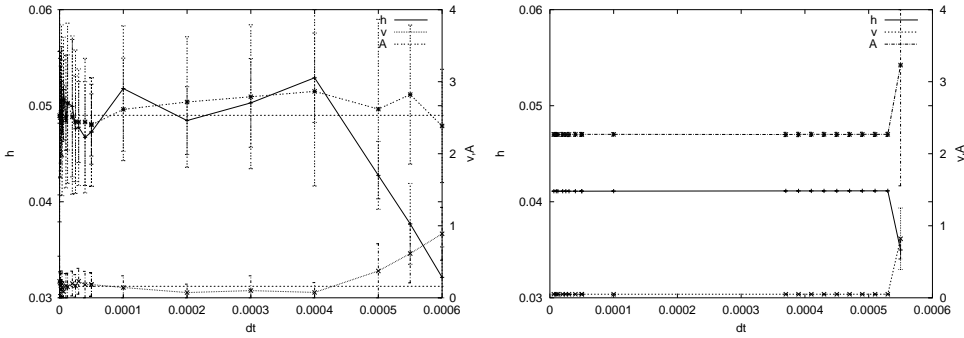
Fig. 4.5. Influence of increasing time steps δt on h, v, and A. The left plot is calculated for grid size, where the stabilization due to the periodic boundaries is negligible. In contrast the right plot is an example of a one ripple solution.

Figure 4.5 shows the effect of the selected time steps. On the right plot we can detect a critical time step around $\delta t_{cr} = 0.0005$, beyond this value the measureants significantly diverge. The solutions for smaller time steps seems to be independent of the time resolution, even though the high variations of the measured values prevent one's to exclude any influence of chosen time steps. Therefore a solution is also considered, where the periodic boundaries care for more stable data. The variation of time step yield a comparable critical time step, so that we assume that the results below this value are independent of the special time step.

The concrete value of the critical time step certainly depends on the grid resolution. The finer the grid spacing the smaller the critical time step. To avoid adjusting of time steps in relation to grid spacing, we couple the model equations by an adaptive time step method (see Fig. 4.6). Therefore we solve Eq. 4.2 with a given relief $I(x) = H(x)$. The resulting shadow function $S((H(x))$ is inserted in Eq. 4.1, where the change of height is always calculated based on $I(x)$. The new height $H(I(x), S)$ in turn is inserted in the
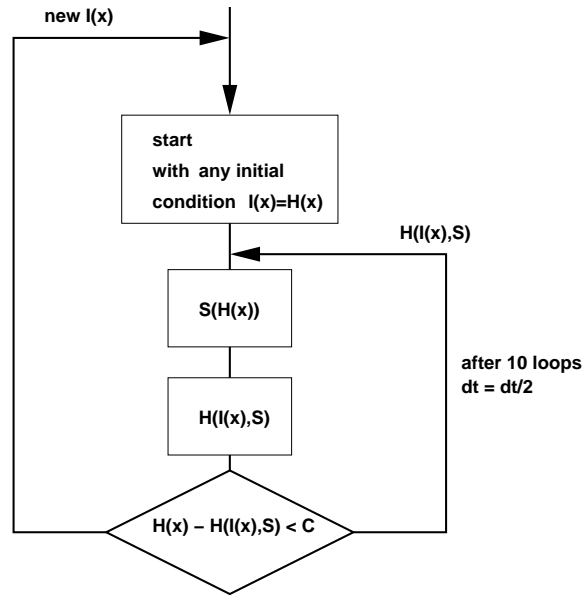
Fig. 4.6. Flow chart of the adaptive time step method.

shadow equation. After some loops the shadowing should no longer change and another time step can be computed. If not, the actual time step is halved and the procedure is repeated.

4.5 Variational Grid Spacing

In our former model (Sect. 2.3) the space resolution was a crucial point because the shadow function was defined in relation to the crest of ripples. For equidistant grids it is clear that the exact position and height of a crest depends on the resolution. A big advantage of the actual model is the robustness against variation of grid spacing. Figure 4.7 shows the variance of the average height over a short simulation run for different grid spacings δx. The equations are solved for different number of grid nodes N and constant grid length L. Hence if N increases, $\delta x = \frac{L}{N}$ decreases accordingly. The graphs converge well for higher resolutions and in the longer run.

Empirically we found that the results become instable if the relation Eq. 4.4 is not fulfilled. Whereby the first term comes from analytic considerations of Eq. 3.4 i.e., Eq. 3.7. The meaning of the criterion is easier to understand with the help of the shadow length $l = \frac{1}{\lambda}$ and δx. The second relation of Eq. 4.4 reads then $l > 6\delta x$. Hence to resolve the shadowing adequately, at least six grid cells per shadow length have to be spent for the correct space resolution.
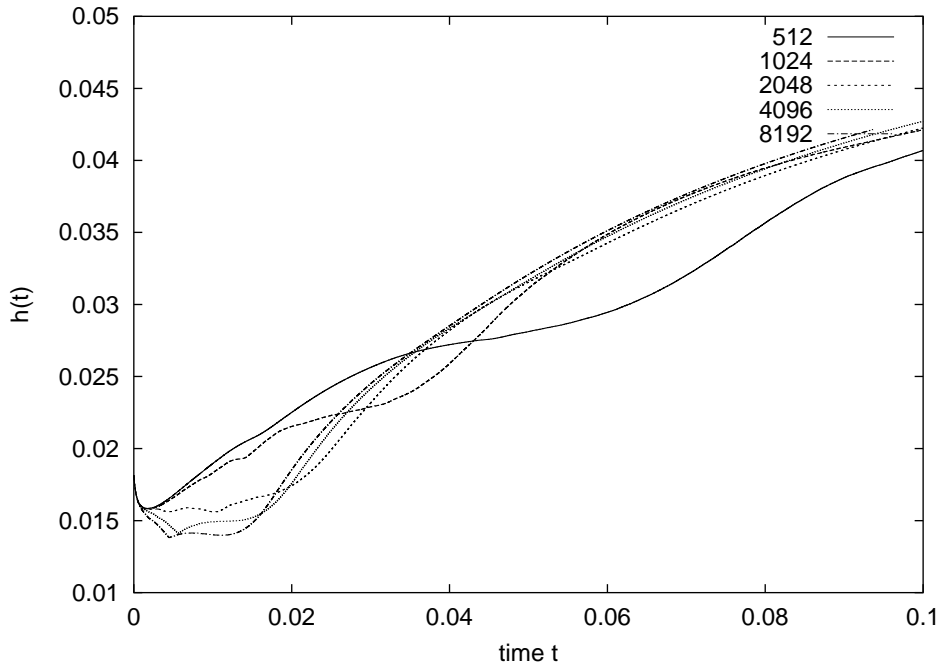
Fig. 4.7. Run of the initial height variance h for different descritizations.

Stability criterion:

$$0 < \lambda L < \frac{N}{6} \qquad\qquad (4.4)$$

In Fig. 4.8 the height variance h and the velocity v are measured over a long run and denoted depending on the space resolution. The system has enough time to develop and to leave the linear range, where the solution certainly depends on grid spacing (see Sect. 3.3). The problem we have to deal with is that the error of the measured values due to time averaging is bigger than or in the same range as the dependency of the grid spacing. The error bars for the velocity allows variation of 100% from the mean in contrast to about 20% due to discretization. The mean h varies around 10% in spite of about 15% because of higher resolutions. Nevertheless we noticed that both measured mean values converge for higher resolutions. The agreement with the fitting function $a/N + b$ underlies the existence of a limit value.

The high variance of the v measurements depends on the methods to determine the velocities of ripples. The definition (p. 48) allows every perturbation to contribute to the group velocity. As the model reacts sensitively on little disturbances, many fast moving waves superimposed can result in highly variable velocities.
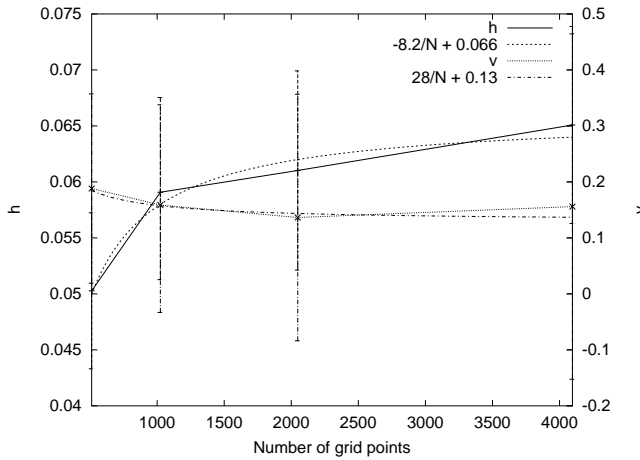
Fig. 4.8. Influence of space resolutions on the measured values h, v. The model parameters are $L = 4$, $\mu = 1$, $\lambda = 8$, and $d = 0.5$. The fitted function is $f(N) = \frac{a}{N} + b$.

4.6 Jumping Length

Some models make differences between the amount of transported particles and the transport distance. The model presented here is stream based and needs neither to distinguish between the transport processes nor to include a jumping length (compare Sect. 2.1.1 and Sect. 2.3). Nevertheless such a fixed transport length could easily be introduced in our model and the effects it produces concerning the principle behavior of the solutions and their dependence on grid spacing are of interest.

The advective term of Eq. 4.1 can be interpreted in the following manner. The amount $\frac{1}{\delta x}\tilde{S}_i$ is eroded from the mesh point i and $\frac{1}{\delta x}\tilde{S}_{i-1}$ is deposited. This means here all "sand packets" are transported One grid spacing δx. What happened if we change this jumping length by a multitude of grid spacing and chose the amount of transported particle (here c) independent of the discretization?

$$\frac{\partial}{\partial t}H = c \cdot \left(e^{S_{\min} - S(x)} - e^{S_{\min} - S(x-\xi)}\right) \qquad (4.5)$$

ξ denotes the jumping length. Figure 4.9 shows h and v respectively calculated for a fixed transport length and with a constant portion c of moved sediment. The number of grid points is increased, which simulate a decreasing transport length of our original model. In the new approach Eq. 4.5 $\xi = j\delta x$ is held constant, which implies a transport over j mesh points. According to decreasing δx the number of overjumped mesh point j grows. v and h are measured for both situations and averaged over a long period of time for different space resolutions. The most upper graph and the lowest graph are calculated without a fixed jumping length (denoted as $dx = 1/N$). Both graphs in the middle are computed according to Eq. 4.5 (denoted as $dx * j$). Qualitatively, sand transport with a fixed jumping length does not differ from the original stream approach. Both converge to a limit value with increasing
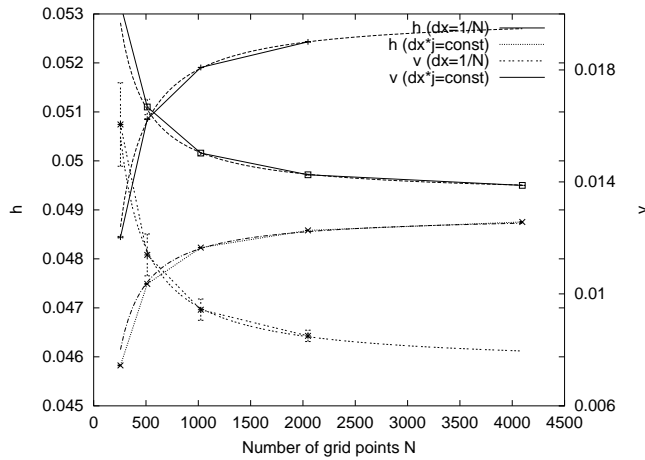
Fig. 4.9. Comparison between simulations with and without a fixed jumping length. $dx * j =$ const denotes result, where the sediment is transported over j mesh points and $dx = 1/N$ represents the original model results. To underline the evolution all graphs are fitted with $f(N) = \frac{a}{N} + b$.

grid spacing. Quantitatively there are differences. The velocity in the case of fixed jumping length ξ is nearly twice as much as for the variable transport length δx and h is about 10 % reduced. Thus a jumping length longer than the cell size enhances the transport velocity.

Also we notice that if a constant transport length ξ is introduced in our model the results do not change qualitatively. This supports our idea to chose a simplified transport process by implementing a stream approach, where the additional parameter ξ is avoidable. We must also admit that on a granular scale it is important to differ between the distance single grains could move and the total number of entrained particles. As long as our attention is directed toward a description of large scale ripple dynamics on a "sand packet scale" this reduction of parameter is reasonable.

5. Results

Our model generates manifold one–dimensional patterns. A central aim of this chapter is to interpret the model results appropriately in order to learn more about naturally observed processes. We concentrate on the set of solutions, which migrates downstream and which are sufficiently asymmetric. An exception is made, when the influence of the different parameter is considered in a systematic way. Although in numerical computations a random distribution (in space and time) of disturbances could be utilized, the results obtained through this approach starts mainly with single small disturbance. The advantage is that initiation and selection of the first bedforms can be better observed. But it is important to state that the simulated ripple formation depends not on the special choice of the starting conditions (Sect. 5.5).

5.1 Simulation Examples

Figure 5.1 shows the simulated formation of ripples, on the left, beginning with a little disturbance and, on the right, beginning with randomly distributed irregularities. Around $t = 0.2$ first ripple pattern covers the whole area. For one irregularity the development successively occurs from the left to the right in downstream direction. In contrast, the random bed fluctuation (right picture) are first smoothed before little ripples start growing, arbitrarily distributed over the entire domain. At the beginning, the random initial condition shows a lot of interaction between ripples of different sizes. Also for developed structures interactions of ripples continues, mainly by merging. Generally the bigger ripples behave more slowly than small ones. The different initial profiles do not influence strongly the ripple evolution at later states. Both examples are taken out of a transient regime.

In Figure 5.2 4 examples of developed ripples are given. Apart from the first all are cutoffs from larger grid sizes $L \in \{8, 16, 32, 64\}$. The profiles result from long simulation runs, $T > 100$, to ensure that the transient phase has finished (compare Fig. 5.4). The measured values: the variance of the ripple height h, velocity v, asymmetry A, and #max are denoted in table 5.1. All measurements agree well within their error bars. The results fulfill the basic features and definitions of ripple forms. With regard to the shape this means that ripples consist of a flat stoss slope and a steep lee slope, so that they
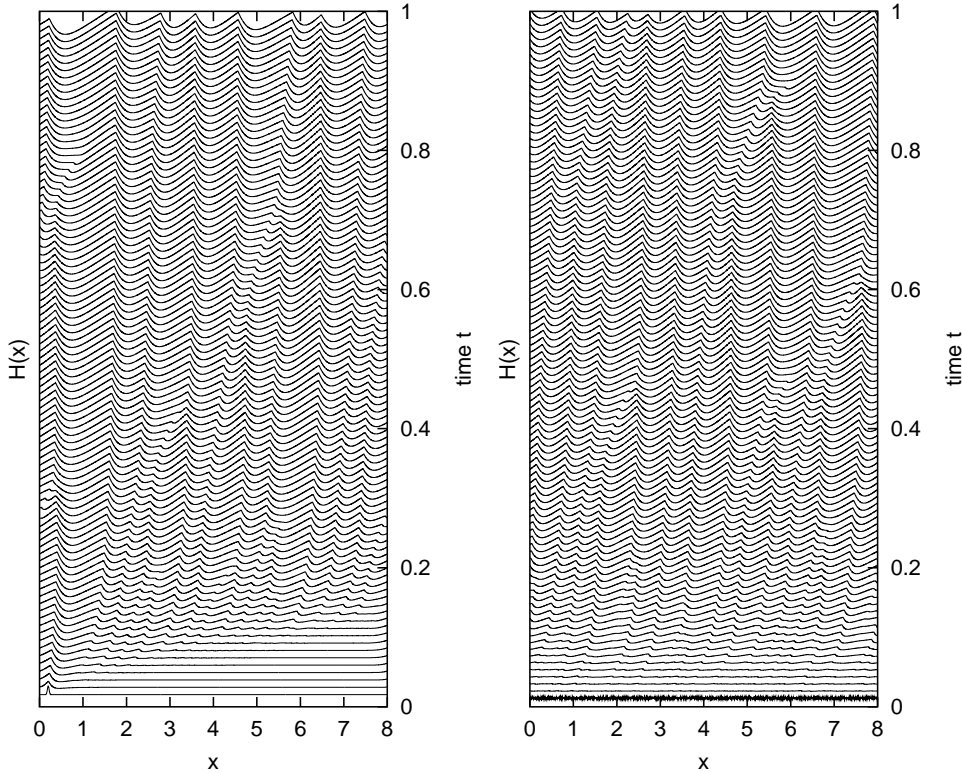
Fig. 5.1. Spatiotemporal evolution of simulated ripple system. The successive profiles are vertically shifted.

L	h	v	A	#max
8	0.051 ± 0.005	0.16 ± 0.1	2.5 ± 0.4	7.9 ± 1.1
16	0.053 ± 0.004	0.17 ± 0.08	2.5 ± 0.4	16 ± 1.7
32	0.057 ± 0.005	0.16 ± 0.06	2.5 ± 0.3	32 ± 2.7
64	0.055 ± 0.004	0.16 ± 0.04	2.5 ± 0.2	64 ± 3.4

Table 5.1. Time averaged data for the plots shown in Fig. 5.2.

are asymmetric. With regard to the dynamics, ripples migrate downstream (positive velocity v) in the direction of sediment transport.

To analyze the distribution of wavelengths we measured all wavelengths and ripple heights of the four profiles and calculated the frequencies (compare Fig. 5.3). The variation of the heights and the wavelengths are around 100%. Our ripple structures show a higher variability than ripples formed under nearly one–dimensional flow conditions (annular channel Sect. 1.2.2). Many different wavelengths can exist simultaneously. During the time, periods of one wavelength with less variability and periods of a multitude of wavelength with high variablity could alternate (see Sect. 5.6 and Fig. 4.4).
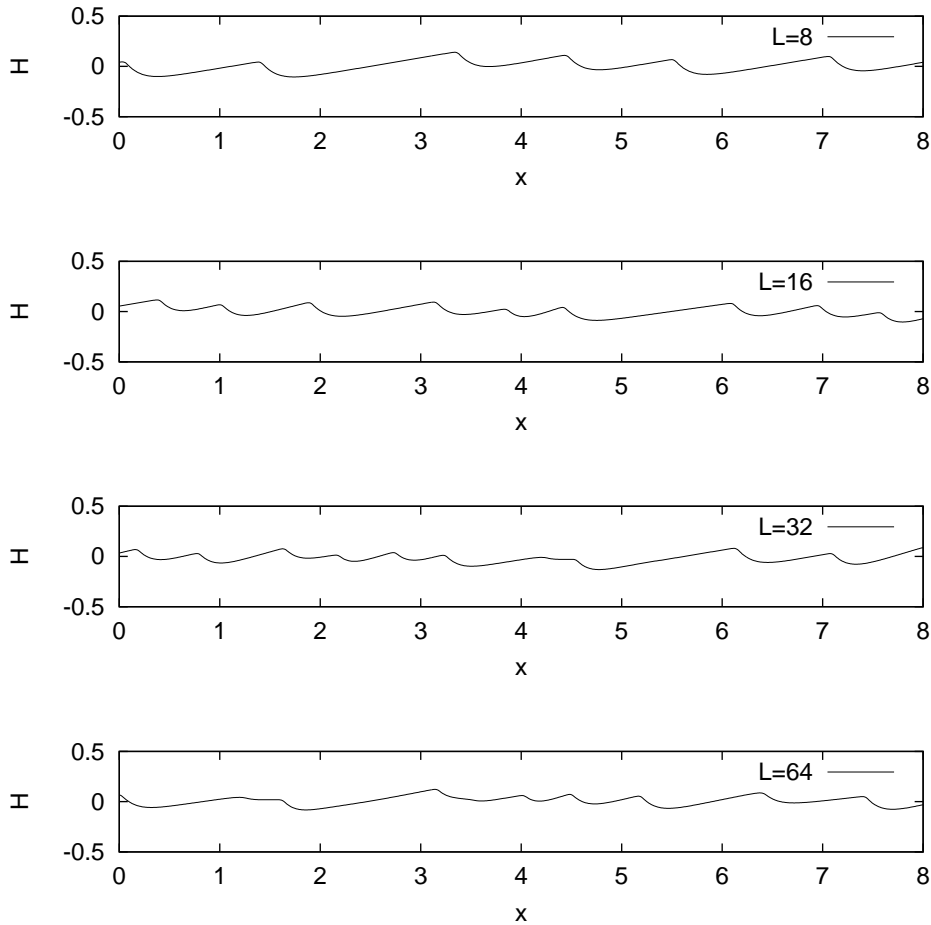
Fig. 5.2. Simulation examples. The chosen parameter are $\mu = 1$, $\lambda = 8$, and $d = 0.5$. The grid length L changes from 8 to 64. Only a cutoff of the length 8 is shown from the profiles.

Looking at the ripple profiles Fig. 5.2, it is hardly distinguishable which one is a cutoff of which area. In detail they do not correspond to each other, but globally the patterns have much in common. The declination of the lee side is nearly the same for all ripples, other than in the cases of merging or diverging ripples. In Fig. 5.4 all measured lee slopes are represented in a bar diagram. The distribution is narrow which affirms that most ripples have a similar lee slope. Thus the grow and migration process at the crest of a single ripple which is responsible for the lee inclination, seems to be the equivalent.

To evaluate the model and to find out model characteristics we have to exclude effects on the result, which depends only on the special choice of the boundaries. The resemblance of the ripples of different grid size in
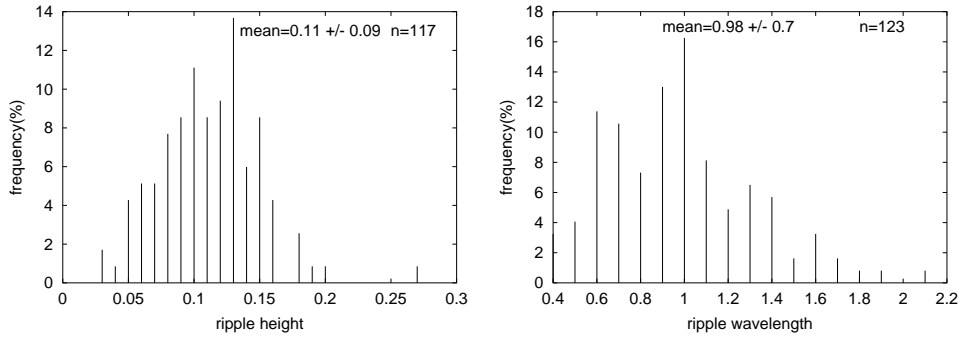
Fig. 5.3. Height and wavelength distribution of the ripples in Fig. 5.2. All ripple heights and wavelengths are calculated considering the entire area. The sampled data are pooled to be represented in a bar chart.
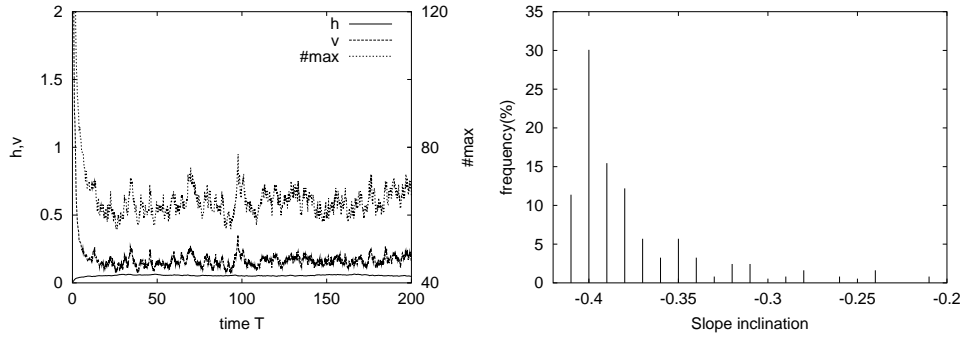
Fig. 5.4. The diagram on the left shows the time development of profile $L = 64$ of Fig. 5.2. There is a clear transient phase before for $T = 20$. The diagram on the right represents the summation over all lee slope inclinations of Fig. 5.2. Therefore the full profile lengths are considered.

Fig. 5.2 indicates already a small influence of the boundaries, which is further investigated in the next section.

5.2 Stability

Two questions concerning the stability are investigated. First, we analyze whether there is a stabilizing effect due to the periodic boundaries of the model? As mentioned above, the results show a high variability which lead us to the second question of what kind of system describes the solution space of our model?

To approach the first question we enlarge the calculation area in order to reduce the boundary influence and to see whether the characteristics of the solution changes. In Fig. 5.5 the average number of maxima are plotted in relation to the area size. The corresponding simulations run over a long time period ($T = 200$). The error bars along the graph represent the variance ρ of
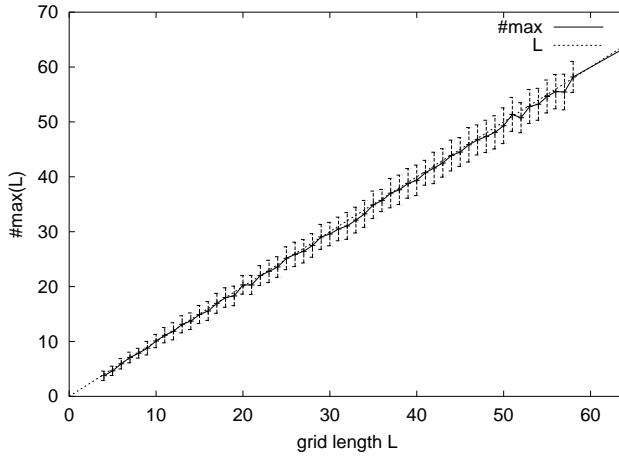
Fig. 5.5. The diagram shows the average number of maxima in comparison to grid lengths for fixed λ. The bisecting line corresponds to a wavelength of one.

#max which follows from Eq. 5.1. The discretization was increased proportionally to the grid length L to ensure a constant number of grid points per ripple and thus to avoid numerical influences.

$$\rho = \sqrt{\frac{1}{T} \sum_t \left(\#max_t - \#max_{av}\right)^2} \tag{5.1}$$

The graph shows that the mean wavelength $\Lambda = \frac{L}{\#max}$ of the solutions does not change with increasing grid length and stays around 1. The other values as h, A, and v are also measured during the simulations. The results are denoted in Fig. 5.6 including a graph where the variance ρ of #max is plotted separately in relation to the grid size. All mean values show no systematic dependency on the area size. In particular the mean values of A and v fluctuate a little depending on L. Therefore, the influence of the periodic boundaries seems to be negligible, especially for larger grid sizes.

To answer the second question, we look closely at typical simulation runs (see Fig. 5.9 and Fig. 5.23). We can see that the main ripple pattern is superimposed by little faster moving structures or perturbations, which imply the high variability of the solutions. Usually, stable solutions are bedforms i. e., ripples which move downstream preserving their shape, hence stationary states which are insensitive to perturbation of the surface. So only the averaged mean values are stable. In fact the perturbations in our simulations seem to be necessary to adjust ripple wavelength over the whole area. The process is reminiscent of avalanching in the case of a sand hill, which holds the slope inclination around the angle of repose. Our former model which does not show such disturbances always develops to a one–ripple system. To characterize the system behavior we ask to what extent perturbations reach if the area is prolongated? Do disturbances still affect the whole domain? – which is surely true for small area sizes due to the periodic boundaries – or are they limited in their range? If the range of perturbations is unlimited the system
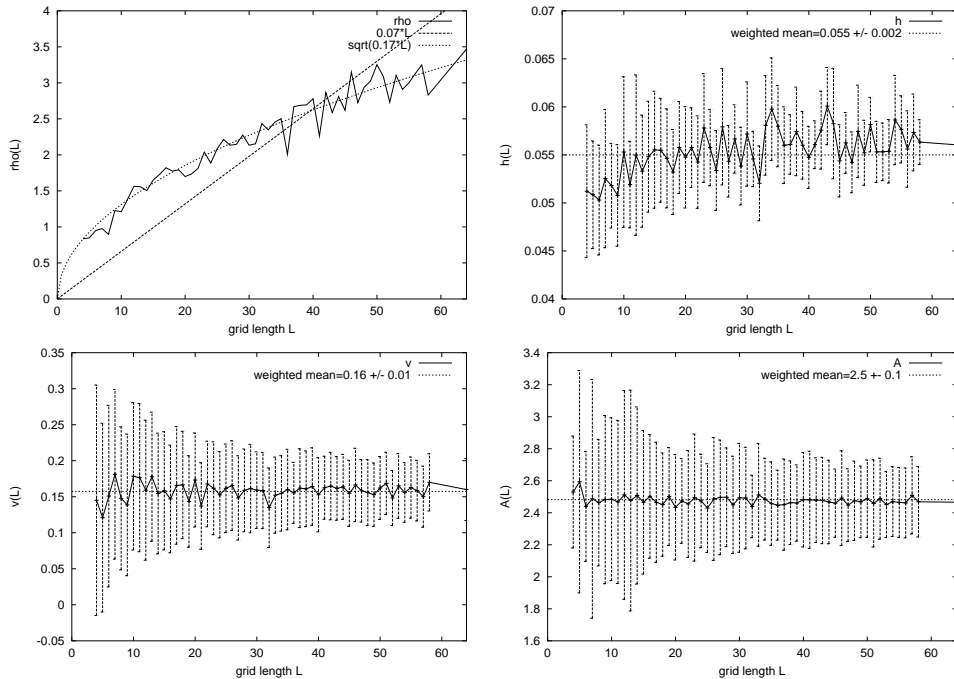
Fig. 5.6. The time averaged mean values of solutions for varying grid sizes L are plotted. The upper left graph shows $\rho_{\#}\text{max}$ (Eq. 5.1), the upper right the variance of the height h and the both lower graphs the velocity v and the asymmetry A. The error bars represent the variance of their respective mean values.

behaves chaotically. For the variance ρ of $\#$max this implies a linear growth with L, as perturbations gain a longer reach in proportion to the area size. As mentioned the first diagram of Fig. 5.6 is the plot of ρ versus L. Its behavior resembles more a root function than a linear fit. The result supports the conjecture, that perturbations have a limited reach and are somehow smothered during propagation. This may correspond to a chaotic system behavior in the subcritical region. The other measured data support this observation, since the absolute values of the variance seem to converge towards increasing grid length L, too. Recent observations (Sect. 1.2) favor a stationary final state for ripples systems than sorts of chaotic system behavior (such as for example in sand piles (Benza et al. 1993)). As long as the experimental influences on the final pattern are still not clear and since there is a lack of long simulation runs, conclusions on the principle system behavior remain uncertain.

5.3 Migration

Ripples in equilibrium state move very slowly (see Sect. 1.8). In contrast the interaction and wavelength selection processes are much faster (compare Fig. 1.12). Thus, beside the normal transport process of ripples which obeys
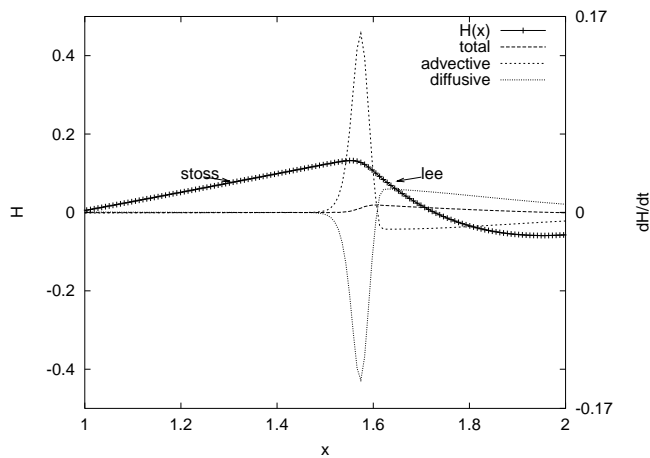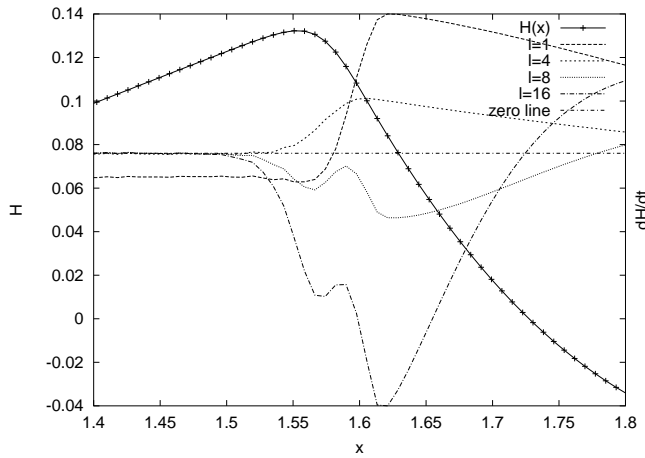
Fig. 5.7. The ripple is a cutout of a structure with six ripples. The corresponding heights are denoted on the left scale. The other graphs represent the change of height per time in the case of only advective stream acting on the surface, only diffusive stream, and the summation of both streams (total). The zero line indicates the change from erosion (stoss side) to deposition (lee side).

the inverse relation, (definition (p. 14)) there is also some faster propagation mechanism. This section is divided into two parts: one considers the migration of isolated ripples and the second describes the movement of a whole ripple system.

5.3.1 Isolated Ripple

Figure 5.7 shows, how simulated ripples move. The plotted ripple is a cutout of a system of six developed ripples. The sediment transport over the present ripple is calculated with respect to the shadowing (advective), to the diffusion (diffusive), and the total transport (total). Beginning with the total sediment flux, we make the following observations: on the stoss side sediment is eroded and transported downstream to the crest; towards the crest with growing negative curvature the shadowing starts and erosion decreases. Around the crest deposition occurs and reaches the maximum on the lee side. Without diffusion nearly all sediment is accumulated just behind the crest. As the curvature changes its leading sign the relaxation of the fluid stream and hence the sediment transport restarts. Therefore erosion takes place even on the lee side, if diffusion is absent. The result would be an increasing inclination of the lee side. Due to diffusion, the sand deposited behind the crest is distributed along the lee slope. The curve named "total" represents the effect of the sum of the diffusional stream j_d and the advective stream j_d. The resulting partition of accumulated material, is fairly comparable to observed natural distributions (Chakrabarti and R.Lowe (1981), Hunter (1985) and Anderson (1988)).

Since the lee slope grows in height and the stoss side loses sediment, the whole ripple moves downstream. If the ripple is not influenced by neighboring ripples, the mass loss on the stoss side is equivalent to the mass gain on the

Fig. 5.8. The ripple is a cutout of a structure with six ripples. The corresponding scale is on the left. The other graphs represent the change of height per time for different values of the inverse shadow length (right scale). The zero line indicates the change from erosional to depositional condition.

lee side and the moving ripple can preserve its shape (Mohrig and Smith 1996). As the velocity of such an isolated ripple obeys the inverse relation: the higher the ripple the slower the velocity (see Fig. 5.10). But there is also another aspect influencing the migration velocity. If the distance between ripple crest and the point of maximum deposition decreases, the velocity of such an isolated ripple also increases. The reason for this is that deposition near the crest is the fastest possibility to move the maximum. All sediment, which is accumulated further downstream on the lee slope first changes the shape of the ripple and since diffusion is acting symmetrically even a little back flow of sand can occur.

The diagram of Fig. 5.8 is a closeup view of the ripple in Fig. 5.7. Four graphs are plotted, which represent the total change of height per time for different values of the inverse shadow length λ. The original ripple was computed for $\lambda = 4$. For this case the corresponding graph is equivalent to the graph 'total' on Fig. 5.7, which represents a moving momentarily stable ripple. Altering λ changes the ripple characteristics. In fact increasing values of the inverse shadow length, tends to diminish the wavelength (see Sect. 5.4) and hence destabilize the existent ripple. To understand the run of the curves we have to remember that higher value of λ means a fast regeneration of the original stream and an abrupt end of shadowing, respectively. So there is a narrow region where the sand transport restarts and erosion takes place. Therefore modulation of the ripple height takes place around this site and a small bump is built, which later on produces new structures. For $\lambda > 4$ the lee slope steepens. The migration direction just after the parameter change turns backwards, since the old patterns mainly decay. Only $\lambda = 1$ preserve the main characteristics of the ripple. The shape will be adjusted towards a less asymmetrical structure. Summing up this example, it makes clear that changing the parameter can completely modify the migration characteristic until new patterns are established. This reorganization needs a relatively long
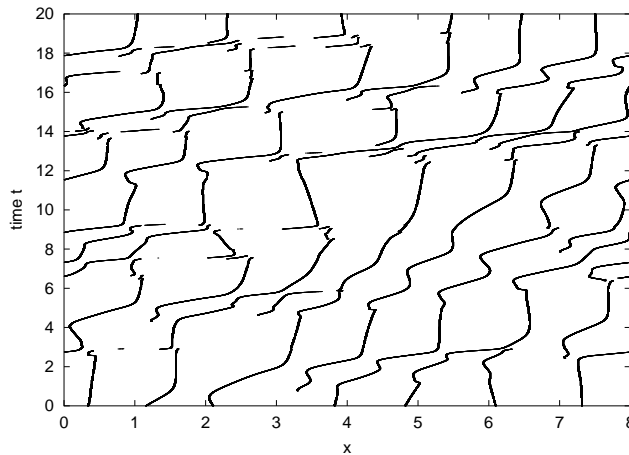
Fig. 5.9. Position of surface maxima plotted in time (vertical) and space (horizontal). Regions of uniformly downstream moving ripples alternate during time with short regions of highly perturbed ripple patterns.

time, especially if the ripple is part of a ripple system as the one considered here.

5.3.2 Ripple System

The migration of a whole ripple system is more difficult to observe and to determine numerically. The algorithm used for calculating the velocity is derived from the cross correlation of two stages of solutions shifted in time (see Appendix A). If the ripple pattern is simply stationary i. e., $H(x, t) = H(x - v_g t)$, then the measured velocity would be equal to the group velocity v_g.

In Figure 5.9 the positions of all surface maxima are plotted in time (vertical) and space (horizontal). We identify each relief maximum with a ripple crest, knowing that some mounds could be only disturbances, especially in regions with highly interacting ripples. We can observe groups of ripples, which migrate very regularly to the right (downstream) preserving their wavelength. Also, perturbations of this ripple occur from time to time forcing the ripples to rearrange their wavelength. This kind of signal propagates very quickly through the area (an interpretation of this processes will be given in Sect. 5.6). Determining the migration velocity, this 'high speed' event contributes inevitably to the measurements and causes an overestimation of the ripple velocity. We have to keep this in mind when we are analyzing measurements of the velocity.

Figure 5.10 is a plot of the velocity v against the variance of the height h. The pairs v, h correspond to different values of the diffusivity d. As the variance of v is much higher than the one from h, we plot only the vertical error bars. The evolution of the graph shows clearly that high velocities are present for small heights of the relief (there is no qualitative difference here between h and the absolute height H) and vise versa. This anti–proportionality is a little disturbed for high values of diffusivity, where the error bars increases.
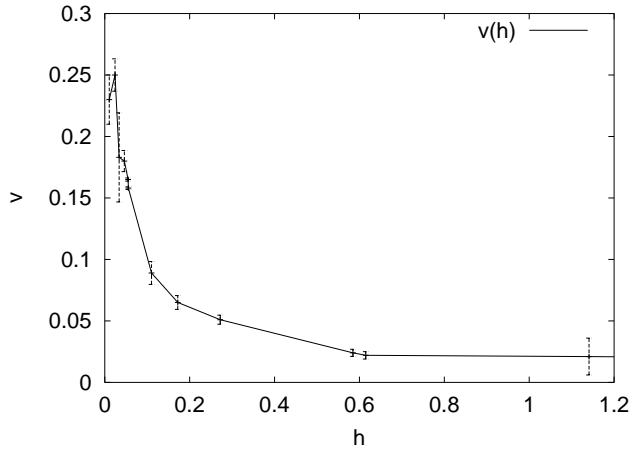
Fig. 5.10. The diagram is a plot of the relation between h and v. The values are measured for a changing parameter d. It decreases for slower velocities. The parameters μ and λ are hold constant.

Generally speaking we can say that despite the tendency of our approach to overestimate ripple velocities, the inverse relation is well confirmed, even for ripple systems.

5.4 Variation of Parameters

The three parameters of the model are considered separately. Due to adequate scaling, λ could be eliminated. Nevertheless we include λ in our examinations in order to enhance the clearness of the model.

5.4.1 Diffusivity d

In Figure 5.11 the four measured values are plotted depending on d. All measurements for different d are performed over long simulation runs ($T = 100$) and for at least three grid sizes ($L = 8, 16, 32$). To hold the space resolution constant the number of grid points is increased accordingly. For each graph either a reciprocal, a linear, or a constant function is fitted. If we first consider the plot which shows the variance of the ripple height h, we can see that according to higher values of d, h decreases approximately as $\frac{0.1}{d}$. This decay is not surprising because the diffusion smoothes patterns. If only diffusion were present the model Equation 3.3 would read:

$$\frac{\partial}{\partial t}H = -d\frac{\partial^2}{\partial x^2}H$$

For a Gaussian distribution with $H(x = 0, t = 0) = H_0$ the solution looks like:

$$H(x,t) = \frac{H_0}{d^{\frac{1}{2}}(4\pi t)^{\frac{3}{2}}}e^{\frac{-x^2}{4td}}$$
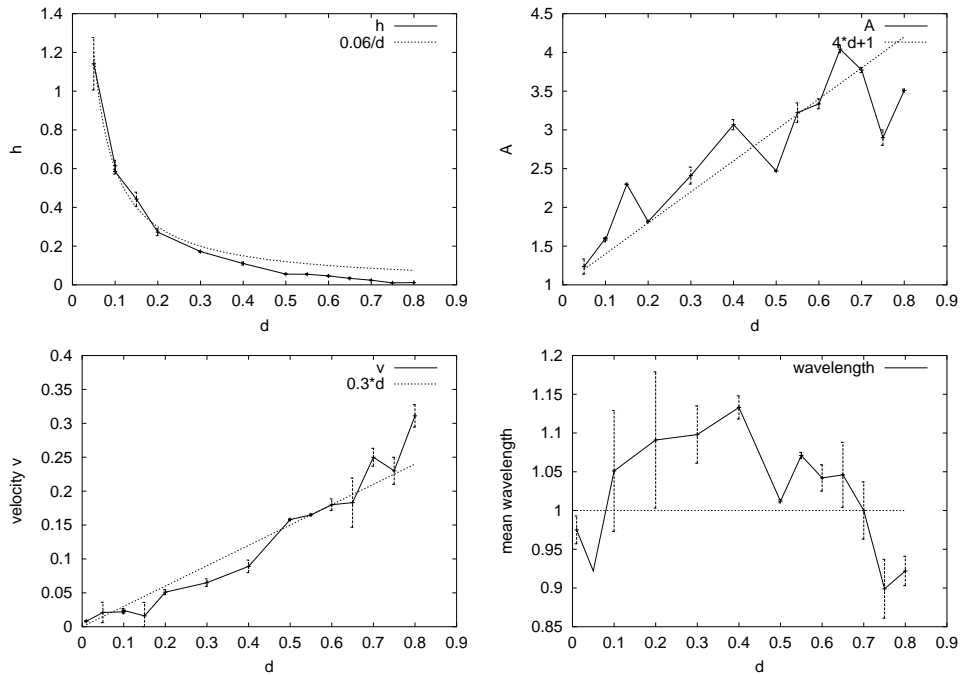
Fig. 5.11. Influence of the diffusivity d on h, A, v, and the average wavelength $\Lambda = \frac{L}{\#\max}$. The denoted fit function shows simply the qualitative evolution of the plots. Beyond $d = 0.8$ the solutions are numerically instable and therefore omitted.

Hence the diffusivity would simply enhance the decay of the structure in time, if no pattern creating process is present. Including the advective term, the diffusivity varies h as long as an equilibrium between both processes is reached. Concerning the lee slopes this implies increasing gradients for decreasing diffusivity (see Figure 5.14).

The next diagram of Fig. 5.11 is about the average asymmetry A of the modeled ripple patterns. The general tendency of the curve shows that the higher d, the higher is the average asymmetry. Due to the high variability of the results only a qualitative linear fit can be adjusted to the evolution of the graph. For determining the asymmetry according to the definition (p. 2) the algorithm needs the location of maxima and minima on the relief. Each pair of maxima and minima is thus included and produces, under certain conditions (e.g. little perturbation), very high values. This explains the high variation of the result. But how can we understand the tendency that an increased diffusivity implies higher asymmetries? Of course the diffusional term in Eq. 3.3 produces itself no asymmetry at all. Nevertheless the diffusion affects the way in which a sand packet transported due to shadowing will be redistributed (compare Fig. 5.7). If d is small, nearly the whole sand packet deposited behind the crest can rest there. As a consequence the crest does not only move, but also grows in height. High growth rates versus low migration
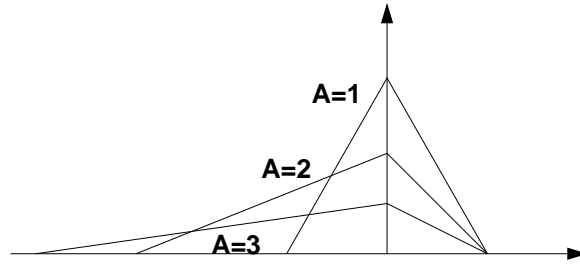
Fig. 5.12. Illustration of the effect of increasing diffusivity d on the asymmetry A. The diagram does not show the complete truth (see Fig. 5.13).

rates generates symmetrical bedforms, shown schematically in Fig. 5.12 ($A = 1$). As the diffusion increases the sand packets are distributed more widely over the lee slope and thus migration overcomes the growth process. Hence smaller, faster and more asymmetrical ripples are the result ($A = 2$, $A = 3$). Consequently this explains also the run of the velocity plot. The ripple velocity increases with increasing d. As mentioned above the variability of velocity data is high.

The last diagram of Fig. 5.11 shows the time averaged wavelength in relation to the diffusivity. d seems to have no systematic effect on the wavelength selection. The mean wavelength is around one. Thus we have to redraw Fig. 5.12 in the following way: the mistake in Fig. 5.12 is that the cross area of
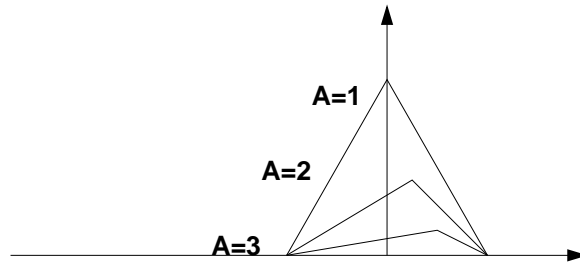
Fig. 5.13. Illustration of the effect of increasing diffusivity d on the averaged wavelength Λ.

the profiles is nearly preserved. Thus the mass is also conserved and therefore it is not possible that for the same transport capacity μ the velocity increases as much as observed. Ripples adjust their entire shape in this way so that the inverse relation is fulfilled. Experimentally the observed inverse relation is based only on crest heights which is not sufficient, if the wavelength does not change accordingly.

Including a diffusional term into our model takes destroying processes into account, mainly due to gravity and granularity (e.g. angle of repose). Since the simulated ripples stop growing and adjust a limited lee slope, we can assert that diffusion is able to confine crest growth and to achieve equilibrium
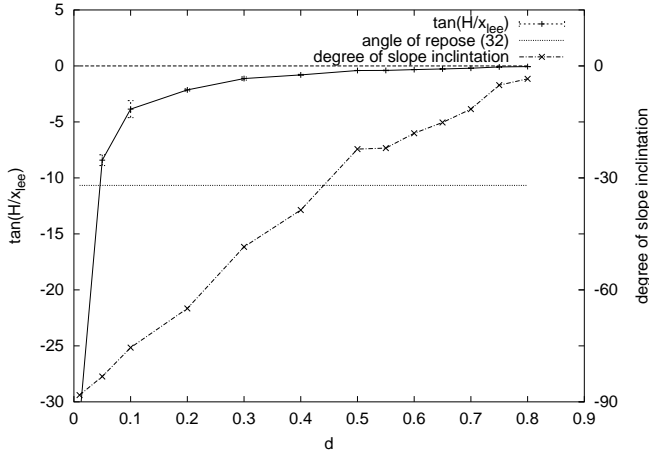
Fig. 5.14. Measured lee slopes of ripples calculated with different diffusivity. The selected profiles are from the model time $T = 100$. The lower horizontal line represents an inclination angle equal to the angle of repose.

conditions. Figure 5.14 shows the measured lee slopes of the profiles belonging to Fig. 5.11 for $T = 100$. One graph corresponds to the slope inclination $\tan(\frac{H}{x_{lee}})$ and the other denotes the angle of slope inclination. The lower horizontal line represents an inclination angle equal to the angle of repose. Higher diffusion implies less inclined slopes. Between $d = 0.4$ and $d = 0.5$ the slope inclination is equal to the angle of repose (p. 9). For ceasing diffusion $d = 0$ the lee slope tends to an vertical inclination (90°), which corresponds to unlimited growth. In the opposite direction the surface tends to a plane bed, if the diffusion is high. For a fixed inclination of lee slope the asymmetry can be derived from the crest height and the length of a ripple. Baas' results show in average asymmetries around 4.2. If in our model the diffusivity d is adjusted around $d = 0.45$ so that the mean lee slope is equal to the angle of repose, the model results tend to an asymmetry of 2.5 ± 0.4 over long runs (see table 5.1), which slightly underestimates the real values. However we have to keep in mind that the experiments from Baas consider 3–dimensional ripple patterns in contrast to our 2–dimensional approach. Nevertheless the range of the asymmetry is reasonable, in particular in comparison to other models (including our former model).

The parameter d has a strong influence on the simulation results.By tuning d it is possible to adjust the lee slopes of the ripples around the angle of repose (Fig. 5.14). This could be a way to calibrate the model results.

5.4.2 Stream Strength μ

The so called stream strength μ is the opponent of the diffusivity. In our process image, changing μ corresponds to a variation of the flow strength which includes a change of the sand transport capability. From an algorithmic view μ determines how strongly the curvature of the bed surface influences the shadowing, thus the maximum amount of transported particles. We assume that for high stream strength the coupling between bed and fluid is easy to
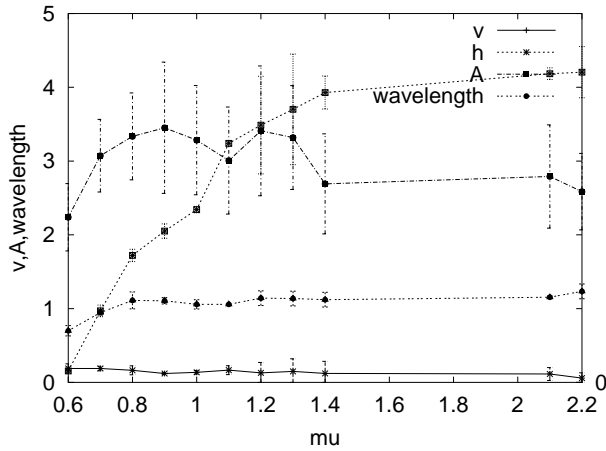
Fig. 5.15. Variation of μ and the consequence for the four measured values. The values are calculated for grid lengths $L = 4, 8$ and averaged over time $T = 100$. Instead of the number of maxima the average wavelength is denoted here.

influence so that the curvature efficiently modulates the sand transport. If we try to compare μ with natural parameters, then the model parameter μ basically incorporates the averaged shear stress (p. 15) and the grain size. Figure 5.15 shows that μ clearly dominates the final mean ripple height. The velocity decreases slightly and the averaged wavelength stay around one. The plot of the asymmetry does not exceed a maximum value of 3.5. Lower and higher values of μ return to values around 2. An increasing asymmetry implies a steeper lee slope which in turn should reduce the growth process. This influence seems to be visible comparing the plot of h and A. However, because of the high variance of the asymmetry we provide here no further interpretation.

Some authors report a hysteresis effect in ripple formation from experimental results (Betat et al. 1999). This means that the way a ripple system reacts on a parameter change is not reversible. If the old parameters are readjusted the back evolution to the former ripple state can be different from the previous evolution. It is even not clear if the same state will be reached again. To verify if such a mechanism is also present in our results, simulations are performed where the parameter μ is changed during the run. Figure 5.16 shows the results of a reduction of μ from 1 to 0.8 (lower diagram) and backward from 0.8 to 1 (upper diagram). Just after μ decreases, the ripple system reacts with complete destabilization. The ripples stop moving, some even move upstream. The effects on the ripple migration velocity can be seen in the right–hand diagram. In addition to this change of sediment transport the number of maxima does not change below $t = 6$. Around $t = 6$ the surface is disturbed, so that a new generation of ripples starts growing and migrating downstream which correspond to a jump of the velocity in Fig. 5.16. The other way from $\mu = 0.8$ to $\mu = 1$ the newly appearing ripples converge again to build a system of seven ripples, which is stable until about $t = 8$. Finally a 6 ripple system, similar to that of the beginning stages, develops. The system reacts much slower on decreasing than on increasing μ and the evolution dif-
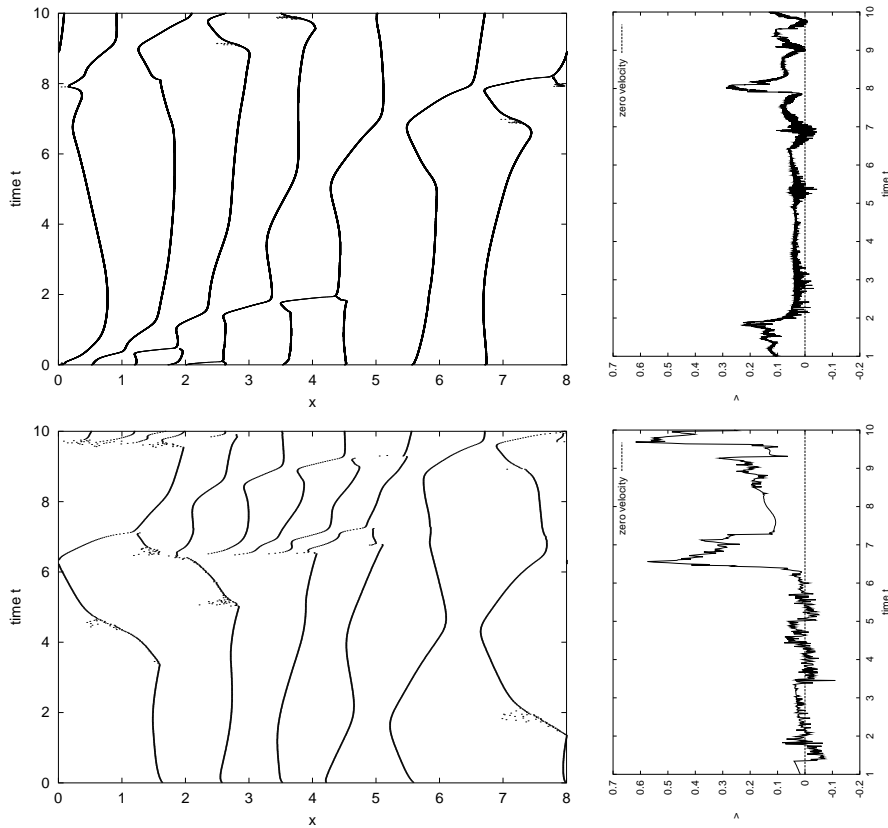
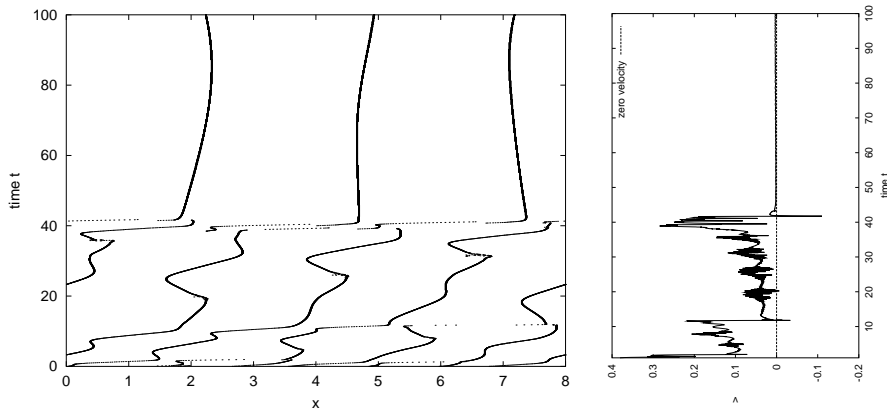**Fig. 5.16.** Simulation run after changing the parameter μ. On the left–hand side the plot of the maxima in time (vertical) and space (horizontal) is shown whereby on the right–hand side the plot of the velocity measurements is denoted. For the lower diagram μ is reduced from 1 to 0.8 and for the upper one μ is increased back from 0.8 to 1.

fers depending on the direction of the parameter change. Hence we see that the ripple system exhibits hysteresis effects.

5.4.3 Inverse Shadow Length λ

The parameter λ determines the reach of shadowing. It measures how fast the influence of the curvature decreases. Small λ means slow relaxation of the originally undisturbed advective flow j_a. Thus long wavelengths are the consequence. In fact λ dominates the wavelength selection of the model (see #max Fig. 5.17). In comparison to natural quantities, it represents the macroscopic reattachment length (Sect. 1.6). It is the only length scale in our model by which the average ripple wavelength is tunable.

Figure 5.17 shows the detailed effect of changing λ. The first three data points before 25 of the graphs represent a two ripple system, which is stabilized by the periodic boundaries and which therefore show small variances.
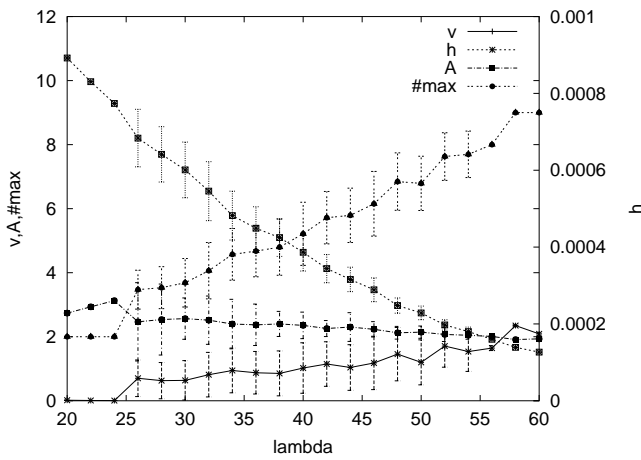
Fig. 5.17. Variation of λ and the consequence for the four measured values. The grid length L is equal to one. Therefore relatively high values of λ are considered. For $\lambda < 26$ the number of maxima is equal to two and hence dominated by the boundaries. Beyond $\lambda > 54$ the structures are very stable again because the space resolution is too coarse.

Fig. 5.18. Simulation run after changing the parameter λ from 8 to 4. The left diagram is the plot of the maxima in time (vertical) and space (horizontal) and the right one is the belonging plot of the velocity measurement.

For the three points on the right the stability criterion (p. 60) is not fulfilled, why this points are not considered in the following. h decreases continuously for increasing λ. This means shorter reattachment lengths and thus shorter wavelengths have reduced crest heights. Since the mass of few ripples is only redistributed over several new little ripples, this causes diminishing crest heights. As expected, the velocity increases accordingly (lower graph). The asymmetry seems to be independent of λ. This is well in agreement with our result that A should be independent of length scaling (Sect. 3.6).

In Figure 5.18 the model parameter λ is reduced during the simulation from $\lambda = 8$ to $\lambda = 4$. Starting with eight ripples the number of maxima diminishes fast to five ripples. The changeover to the next state with lesser maxima takes more time, nearly double the length of time of the previous state. Such a transition is signalized in the velocity measurement (see left
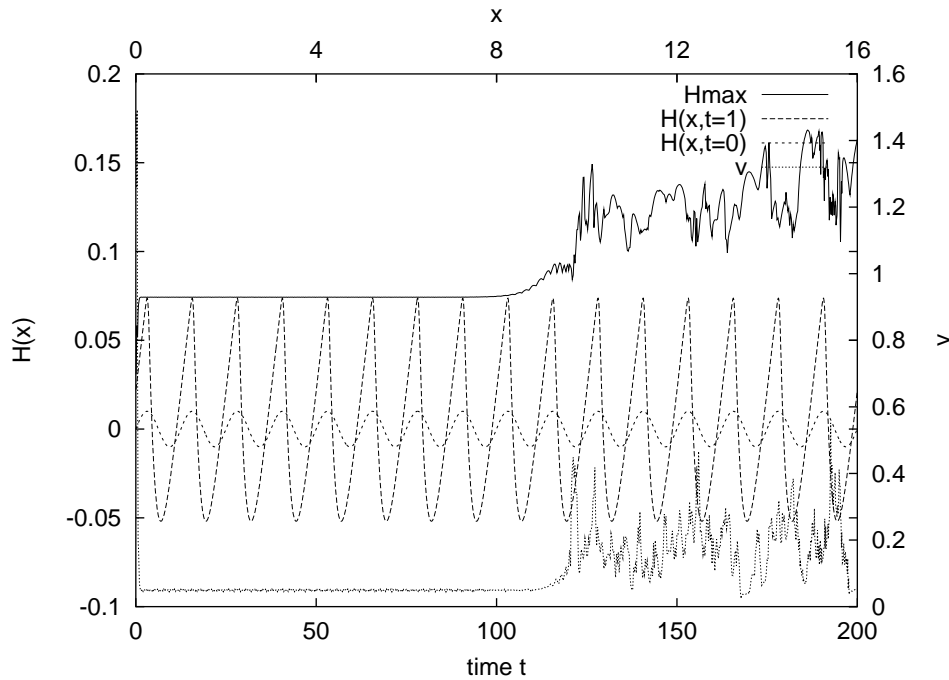
Fig. 5.19. Formation of ripples $H(x, t = 1)$ out of the sinusoidal profile $H(x, t = 0)$. The profile scale is denoted on the top axis. The time scale for the velocity plot and the maximum height plot is on the bottom axis. As usual the left vertical axis denotes the height and the right scale the velocity.

diagram of Fig. 5.18). Here we can easily control how growing wavelengths correlate with slower velocities. A transition to another wavelength causes higher variations (on the velocity plot). This can be explained by recalling that before such a changeover, perturbations play an important role which in turn contribute to the velocity measurement (see Sect. 5.3.2).

5.5 Initiation

Two questions are investigated in this section: firstly, how sensitive is the final pattern to the initial conditions? And secondly, how does the initial wavelength develop?

5.5.1 Dependence on Initial Conditions

The question of whether the initiation of pattern formation is dependent on the shape of the initial profile was already posed in Sect. 3.3. It was found that the special shape is not important for initiation. Here we pose the question a second time focusing now on the final ripple state. We are looking at whether
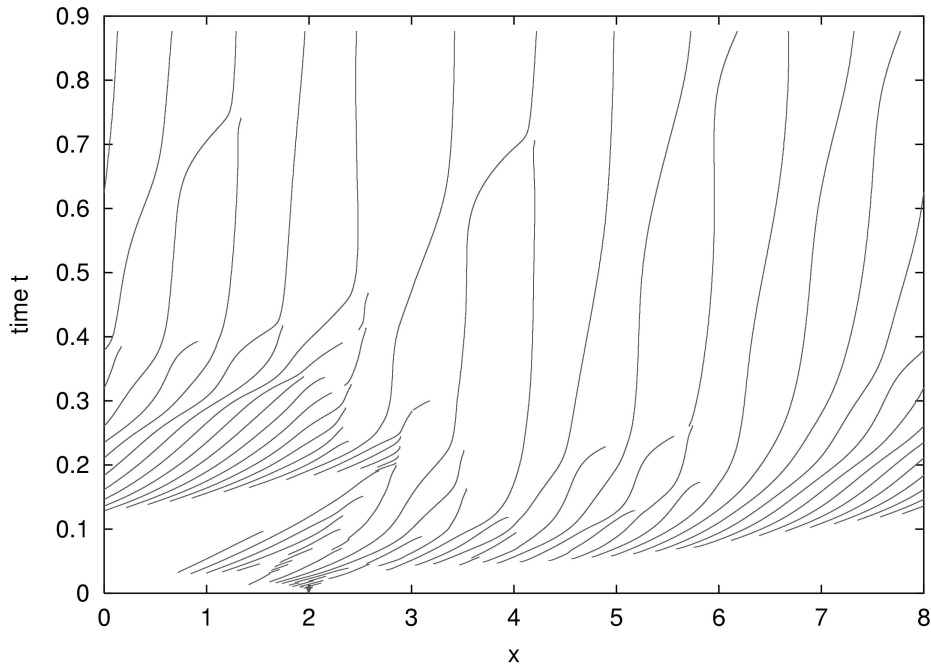
Fig. 5.20. Plot of the maxima in time (vertical) and space (horizontal) starting with a sinusoidal profile of one period.

the final state is independent of the starting profile. If that is true, the final state is also stable against perturbations of the latter stage.

The calculation shown in Fig. 5.19 started from a sinusoidal profile $H(x, t = 0)$ with 16 maxima on a grid length of $L = 16$. The other parameters are the usual ones, so that the sinus function as an initial condition is very near to the expected stable state around a wavelength of one. Indeed the developed ripples $H(x, t = 1)$ are stable in shape for a long time ($t < 120$) and migrate constantly. The velocity and the maximal height hardly varies. However, the system returns finally to the known end state with high variance. The time averaged values measured for $t > 120$ are $h = 0.052 \pm 0.004$, $v = 0.18 \pm 0.09$, $A = 2.4 \pm 0.4$, and $\#max = 16.5 \pm 1.9$. Compared to table 5.1 they are all inside the error bar. Thus the conclusion is allowed that the final state does not depend on a special choice of starting conditions. However the time that is needed to reach the final state is much longer than for a single initial sinusoidal profile. Thus the precise evolution of the system to the final state is dependent on the present (initial) shape of the relief.

5.5.2 Development of Initial Perturbation

In Sect. 3.3 we noticed that the initial wavelength is clearly dependent on the space resolution in the early stage. Figure 5.20 shows the development of a perturbation in time. Again the maxima are plotted in time (vertical)
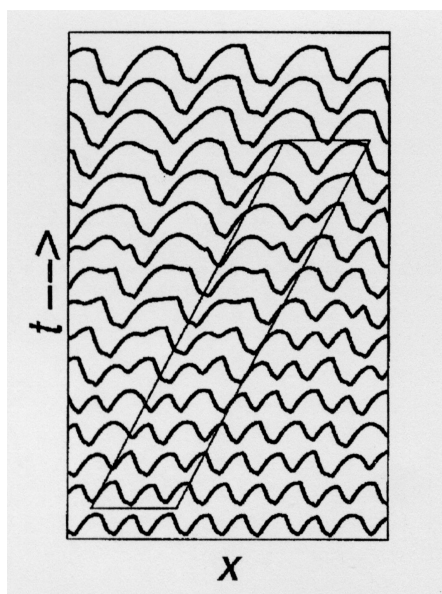
A typical wind ripple interaction from the model of Prigozhin (1999). He describes the process as follows: "As a smaller ripple reaches the larger, the trough between them becomes shallow and a "two-headed" long ripple appears. Then the "downwind head," which originally formed the larger ripple crest, starts to move forward as a separate small ripple and runs ahead. Two new ripples emerge from this recombination."

Fig. 5.21.

and space (horizontal). The perturbation is a sinus profile with one period on the grid length $L = 8$. Interestingly, after a while far from the linear region, new little perturbations (crests) are induced in a downstream direction of the initial maxima. Once created, they slowly grow and move rightwards/downstream. The growth in height and in wavelength is shown in Fig. 1.10 of Sect. 1.7. This pattern formation fulfills the scenario described by Puls (1981). We can observe that merging of ripples occurs shortly after the first pattern is built. This organization of bedforms takes place before the first perturbation pattern meets the original pattern (around $t = 0.2$), due to the periodic boundaries. As the ripples grow, their migration velocity slows down.

Defina (2003) reports the same chain reaction for the formation of bars (diagonal bedforms with height and wavelength comparable to the flow depth and the channel width). In her model, bar height decreases in the flow direction while bar velocity increases. This produces increasing wavelengths in the flow direction. In contrast our simulated ripples show a different formation process: they increase the wavelengths from inwards (near the initial disturbance) to outwards direction, which results in decreasing wavelengths in flow direction.

5.6 Ripple Interaction

Growing interest is posed on the interaction processes occurring during ripple formation (Baas (1999), Betat et al. (1999), and Prigozhin (1999)). The

question is whether the final wavelength of ripples is simply imprinted by the fluid pattern or whether it could be seen as a result of the interaction between the ripples? Prigozhin supposes that small fast moving sand modulation, observed in his model (see Fig. 5.21) has a organizing effect on the wavelength selection. We found very similar processes in our model.

Figure 5.23 illustrates the complex interaction of ripples. The simulation starts with a developed ripple system of averaging 16 ripples. The time scale is plotted at the right boundary. Successive ripple profiles in time are vertically shifted. The vertical curves follow the movement of the maxima during the run. The length scale of the height in y–direction and the coordinates in x–direction are the same. The entire structure moves downstream (to the right) about 9 scale lengths. Regions of stable wavelength and slow migration alternate with regions of high activity, i.e., accelerated movement, birth and death of ripples. Its complexity has more in common with a profile cutoff from a three-dimensional ripple field, than the equilibrium state, measured in an annular channel (see Sect. 1.2).

The detailed view displays interesting processes. New ripples are built on the stoss side of a existing ripple. Sometimes ripples disappear or are caught by another one. If we follow the ripple crest i.e., the maximum through time, and identify the lifetime of a ripple with the existence of the maximum, the lifetimes differ hugely. There is no ripple which stays undisturbed during all the simulation time. In contrast there are a lot of short living ripples. We conclude that our model reacts very sensitively to surface perturbation of short length.

5.6.1 Converging and Diverging Ripples

Converging and diverging of ripples is often observed in flume experiments especially during the transient phase (compare Fig. 1.13 and Fig. 1.12). Converging is more common process as long as the system evolution is below the final state. The time scale for these processes is much shorter than for the normal migration of the ripples.

Figure 5.22 is a simulation example of converging (left diagram) and diverging (right diagram) ripples. For converging the situation starts with the ripple at the site 9.5 which approaches the ripple further downstream. As the ripple climbs up the stoss side of the adjacent ripple, it loses height and its velocity increases, since less mass has to be transported. In contrast, the shadowing of the climbing ripple starts to reduce the sediment transport over the next ripple which as a consequence loses height itself, due to diffusion. However this implies a higher velocity and the ripple can leave without being caught. So it seems that the upstream ripple pushes the one in front of it. Pushing failed the next time at around the site 11.5 and the climbing ripple merges into the adjacent ripple. The evolution is very similar to the scenario shown in Fig. 5.21.
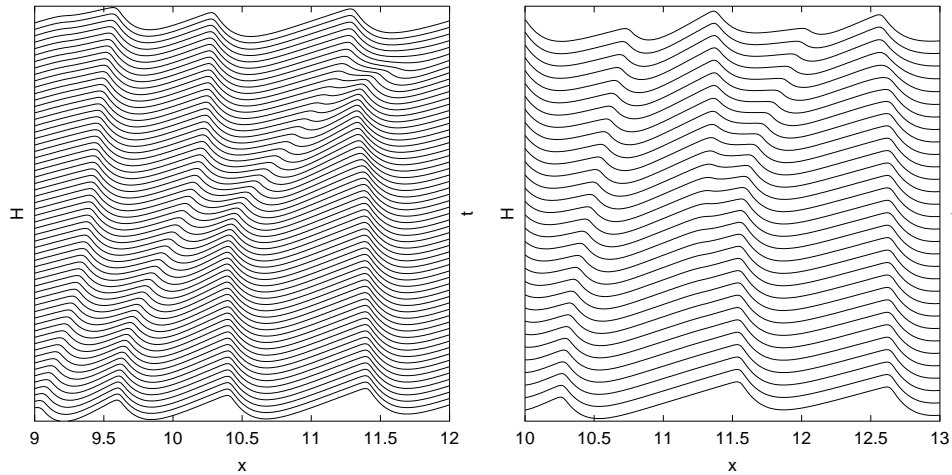
Fig. 5.22. Converging of ripples is shown on the left plot and diverging of ripples on the right plot.

The ripple diverging process compared to other models is new. The typical starting condition is a ripple, which is slightly longer and bigger than the surrounding neighbors. The sand stream at the ripple crest reaches the maximum and the shadowing turns to zero. Then it happens that the region of full stream is prolongated further upstream. In this area the incoming sand flux is equal to the outgoing sand flux and therefore the surface does not change, although in the neighboring region sediment is eroded (upstream) or deposited (downstream). This situation is unstable and does not last long. The small change in curvature at the upstream edge of the area suffices to have a small shadowing effect, representing the fluid detachment. Since the full stream recovers fast (or the fluid reattaches), material is eroded inside the stable surface, which results in the creation of two little mounds and ends in a state similar to the pushing described above.
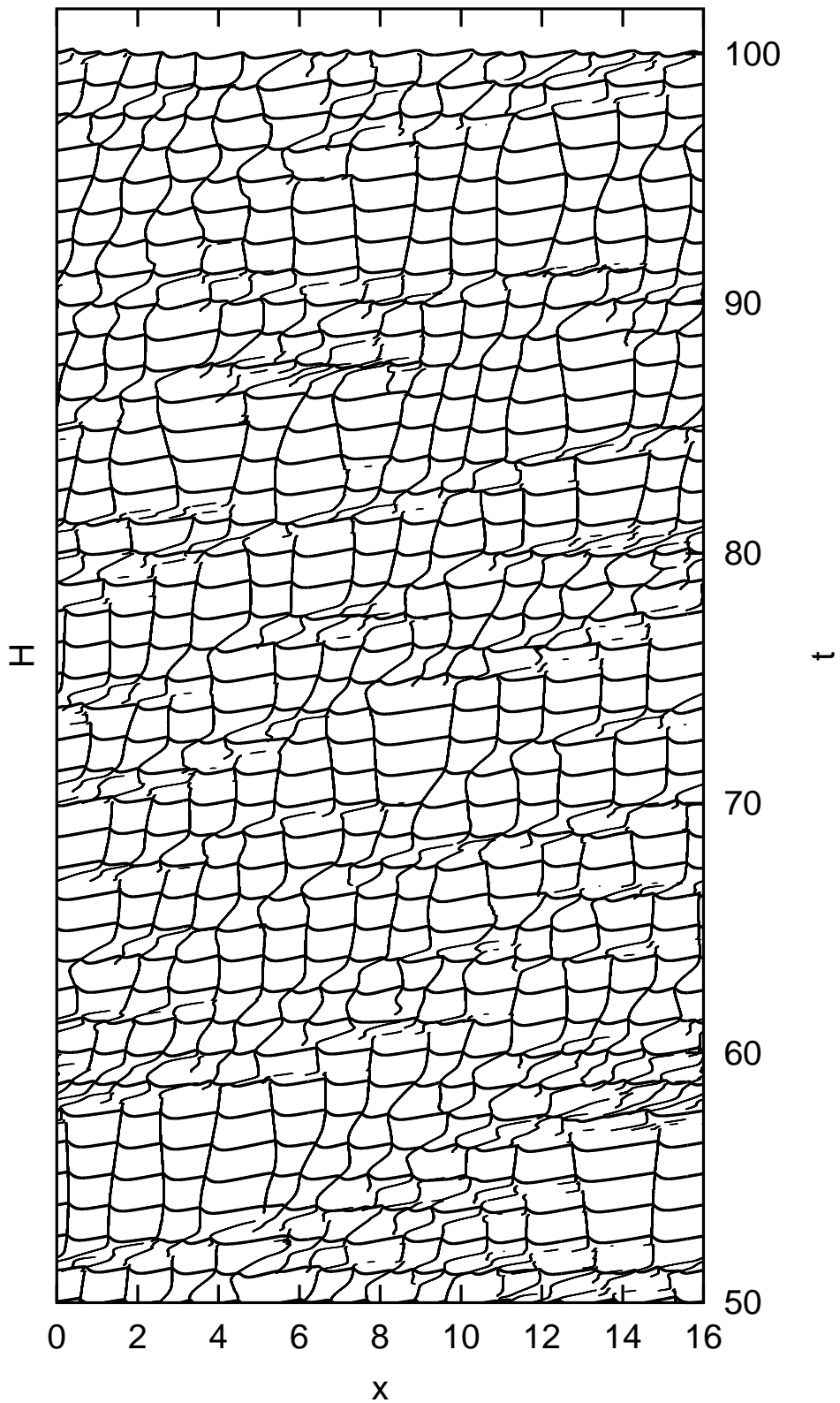
Fig. 5.23. Development of a ripple system in time (vertical shift) and space (horizontal). The ripples migrate to the right and the average velocity is $v = 0.18 \pm 0.08$. Thus the ripples move during a time period of $t = 50$ about 9 length scale. The average asymmetry is about $A = 2.5 \pm 0.4$.

Summary and Conclusions

The aim of this thesis was to approach the problem of ripple formation by a model which describes the phenomenon on a macroscopic scale and does not incorporate the detailed dynamics of the fluid flow field. We developed a parameterization called shadow, which depends only on the negative curvature of the current bed surface. Since the shadow-function is part of a coupled differential equation this approach is non–local. We assert that this non–locality is inevitable to model the characteristic fluid field. Although we avoid back coupling of bedforms to the dynamics of the fluid flow, which seems to be a great simplification of these kinds of models, the resulting shape and their evolution is surprisingly realistic. Furthermore, this approach enables us to simulate the long time and large spatial scale evolution of ripples, which we are hardly able to achieve in natural experiments. Our model supports the idea that the mechanism of ripple formation is not strongly affected by the details of the complex flow structures (Nishimori et al. 1998).

To summerize the results, we begin with the basic ripple features concerning the shape and the migration (Sect. 5.1 and Sect. 5.3). Natural ripples are asymmetrical so that the stoss slope (upstream directed slope) is always much flatter than the lee slope, which is supposed to be mostly around the angle of repose ($32°$). In our model the measured lee slopes turn out to be very stable if no strong influence of the neighboring ripples is present (see Fig. 5.4). It indicates that the local growth and migration processes at the crests seems to be very similar. If the diffusivity d is adjusted in such a manner that the mean lee slope is equal to the angle of repose (see Fig. 5.14), the model results tend over long runs to an asymmetry of 2.5 ± 0.4 (see table 5.1), which slightly underestimates observed values.

Concerning the migration of ripples, the mechanism is clear for isolated ripples (Fig. 5.7 and Fig. 5.8). The redistribution of sediment eroded from the stoss side to the lee side corresponds well to experimental data (Sect. 5.3). An important feature of our model is the fact that it supports the inverse relation, which could be seen as consequence of mass equilibrium (Fig. 5.10). Not only the ripple height but also the ripple shape (asymmetry) changes in that way in that this relation is fulfilled (Fig. 5.13).

The results of our model are more difficult to interpret, when the development of a whole ripple system is investigated. Initiation and stabilization

of the bedforms are especially of interest. It is generally accepted that ripple formation starts in succession of small incidental irregularities of the bed surface (see Sect. 1.7). We experimented with narrow, different shaped initial perturbations and found out that the formation process always shows the following characteristics: firstly the initial wavelength of developing ripples is much shorter than in equilibrium; secondly the perturbation signal propagates faster downstream than the ripples can move; thirdly during initiation the spacing between ripples and the height decreases in downstream direction (Sect. 5.5). This behavior is quite independent of the special shape of the irregularity and in good agreement with natural observed initiation processes. Certainly, if the initial surface is disturbed strongly, this has consequences for the ripple formation at a later stage. From the view of modeling it is a peculiarity that one perturbation is able to create a chain of new surface modulations. Many models, including our former one, need randomly distributed fluctuations in the beginning, which rearrange themselves during the further development process, to build first structures. Here the early pattern formation is not a reorganization or discrimination of existing perturbations, but rather a creation of pattern according to a given fluid flow structure (i.e. shadow).

During the stabilization of ripples converging and diverging of ripples are observable. Both processes (detailed description see Sect. 5.6) are found in the experiments from Baas (1999). In strict two–dimensional experiments from Betat et al. (1999) we detected (see Fig. 1.12) only converging ripples. It is an open question as to whether diverging of ripples could also appear under two–dimensional flow conditions or not. Diverging is responsible in our model for recurring destabilization of ripple patterns, as shown in Fig. 5.23. It seems that little perturbations occurring at the ripple crest control the ripple development from time to time. In this range our measured values vary greatly and it is difficult to decide how stable the system behaves. Therefore we are forced to base all our conclusions on computed mean values. The shown sensibility against little surface modulations at the crest is not present in nature. Perhaps, due to the increasing sediment transport towards the crest, granular damping processes smooth perturbations at the crest rather than amplify them. Future model development will concentrate on granularity to handle the sensitivity against small disturbances (see Sect. 3.3).

Numerically our model is robust and stable. Numerical stable means that the solutions of the model equations (Eq. 3.3 and Eq. 3.4) are independent of grid and time resolutions. Robust means that different discretization schemes i. e., explicit or implicit, do not change the model behavior. There is also no need for adaptive methods as it was necessary in our former model (Küpper 1999). We spend a lot attention on the question of how periodic boundaries influence the model results (Sect. 4.3). As a rule we can notice: solutions, which are not perturbed and thus have small variability are dominated by the boundaries. These are mostly one or two ripple systems. Beginning with

three ripples on the selected area, perturbations arise and the boundaries are of less importance for the solutions. All our measurements are performed for ripple systems of more than six ripples to exclude strong influence through the boundaries.

What is easier to verify, is that our simulated ripples show hysteresis effects. In Sect. 5.4.2 the parameter μ is first decreased and afterwards increased again. Both reactions of the system differ and the initial state is not equal to the final state. This difference in asymptotic values supports the idea that there is a memory effect of the fluid modulation on the landscape evolution (Caps and Vandewalle 2001a). After a parameter change, the evolution of the landscape depends essentially on the former topography i. e., its history. The question is if real granular landscapes show also this memory effect, what is left for future experimental work? Another question of stability is interesting in this context: how stable is the final state concerning perturbations? We investigate the range of perturbations by enlarging the calculation area to find out if the disturbances could still affect the whole ripple system. A linear increase of the range according to the area size would be characteristic for the behavior of a chaotic system. Since the variation of the ripple wavelengths (a measure for the perturbation range) grows like a root function, we assume that our model behaves like a chaotic system in the subcritical region.

Defina (2003) states that the numerical simulation of ripple generation and development in a direct way and on a macroscopic scale could provide the missing link between experimental investigations and simplified theories, offering a valuable tool for bottom morphology investigations. The results discussed above support this assumption and reveal the ability of numerical modeling. Since the main mechanisms of ripple formation are well reproduced by the model, among the complex converging and diverging, our minimal model may be considered as a significant step toward the comprehensive understanding of large scale evolution processes of ripples. The main disagreement concerns the apparent lack of stable equilibrium conditions for the wavelength, due to the sensitivity to perturbations. The whole model approach is based on the assumption that it is possible to simulate the pattern formation only depending on surface attributes. This implies that any change of the flow conditions first rearranges the bed relief before new regular bedforms could develop. Hence our model underlines that ripple formation is not only the result of flow structures, which are simply imprinted on the river bed, but also an effect of ripple interaction.

Acknowledgment

A. Migration Velocity Calculation

Correlation function:

$$K_{\tilde{h}h}(\delta x) := \int_{-\infty}^{\infty} \tilde{h}(x)h(\delta x + x)\, dx$$

$K_{\tilde{h}h}(\delta x)$ measures how much the functions $\tilde{h}(x)$ and $h(x)$ overlap, if they are shifted about δx.

By replacing $\tilde{h}(x)$ with the function $h(x)$ shifted about δt (thus $h(x, t - \delta t)$), you can derive the following relation between δx and δt in regard to K_{max}.

$$K_{\tilde{h}h}(\delta x) = max \qquad \Longrightarrow \qquad \frac{\partial K}{\partial \delta x} = 0$$

$$\frac{\partial K}{\partial \delta x} \quad = \quad \int_{-\infty}^{\infty} \tilde{h}(x)\, \frac{\partial}{\partial \delta x} h(\delta x + x)\, dx = 0$$

$$= \quad \int_{-\infty}^{\infty} \underbrace{h(x, t - \delta t)\, \frac{\partial}{\partial \delta x} h(\delta x + x)}_{=f(\delta x, \delta t)}\, dx = 0$$

$$\Longleftrightarrow \qquad f(\delta x, \delta t) = 0$$

searching for: $\qquad \delta x = \varphi(\delta t) \qquad$ so that $\qquad v_m = \varphi'$

Theorem about implicit functions:

$$
\begin{aligned}
f(\varphi(\delta t), \delta x) &= 0 \\
\frac{\partial f}{\partial \delta t} + \frac{\partial f}{\partial \delta x} \cdot \frac{\partial \delta x}{\partial \delta t} &= 0
\end{aligned}
$$

$$\frac{\partial \delta x}{\partial \delta t} = \varphi'(\delta t) = \frac{-\frac{\partial f}{\partial \delta t}}{\frac{\partial f}{\partial \delta x}}$$

– inserting

$$v_m = -\frac{\int\limits_{-\infty}^{\infty} \frac{\partial}{\partial \delta t} h(x, t - \delta t) \frac{\partial}{\partial \delta x} h(x + \delta x, t)\, dx}{\int\limits_{-\infty}^{\infty} h(x, t - \delta t) \frac{\partial^2}{\partial \delta x^2} h(x + \delta x, t)\, dx}$$

$$= \frac{\int\limits_{-\infty}^{\infty} \frac{\partial}{\partial t} h(x, t - \delta t) \frac{\partial}{\partial x} h(x + \delta x, t)\, dx}{\int\limits_{-\infty}^{\infty} h(x, t - \delta t) \frac{\partial^2}{\partial x^2} h(x + \delta x, t)\, dx}$$

– consideration of the limits $\delta x, \delta t \to 0$

$$v_m = \frac{\int\limits_{-\infty}^{\infty} \frac{\partial}{\partial t} h(x, t) \frac{\partial}{\partial x} h(x, t)\, dx}{\underbrace{\left[\frac{\partial}{\partial x} h(x, t)\right]_{-\infty}^{\infty}}_{\text{h periodic} \Rightarrow 0} - \int\limits_{-\infty}^{\infty} \frac{\partial h(x,t)}{\partial x} \cdot \frac{\partial h(x,t)}{\partial x}\, dx}$$

$$v_m = \frac{-\int\limits_{-\infty}^{\infty} \frac{\partial}{\partial t} h(x, t) \frac{\partial}{\partial x} h(x, t)\, dx}{\int\limits_{-\infty}^{\infty} \left(\frac{\partial}{\partial x} h(x, t)\right)^2\, dx}$$

– discretization

$$v_m = \frac{\sum\limits_{i} \frac{h(t)_{i+1} - h(t)_i}{\delta x} \cdot \frac{h(t+\delta t)_{i+1} - h(t)_{i+1} + h(t+\delta t)_i - h(t)_i}{2\,\delta t}\, \delta x}{\sum\limits_{i} \delta x \left(\frac{h(t)_{i+1} - h(t)_i}{\delta x}\right)^2}$$

$$v_m = -\frac{\delta x}{2\delta t} \cdot \frac{\sum\limits_{i} (h(t)_{i+1} - h(t)_i)(h(t+\delta t)_{i+1} - h(t)_{i+1} + h(t+\delta t)_i - h(t)_i)}{\sum\limits_{i} (h(t)_{i+1} - h(t)_i)^2}$$

94

References

Allen JRL (1970) Physical processes of sedimentation: an introduction. Allen and Unwin, London

Allen JRL (1984) Sedimentary structures: their character and physical basis. Elsevier, Amsterdam

Andersen KH (1999) The Dynamics of Ripples Beneath Surface Waves and Topics in Shell Models of Turbulence. Ph.D. thesis, University of Copenhagen, Copenhagen

Andersen KH, Abel M, Krug J, Ellegard C, Sondergaard LR, Udesen J (2002) Pattern Dynamics of Vortex Ripples in Sand: Nonlinear Modeling Experimental Validation. Phys Rev Lett 88:234302

Andersen KH, Chabanol ML, van Hecke M (2001) Dynamical models for sand ripples beneath surface waves. Phys Rev E 63:066308

Anderson RS (1987) A theoretical model for aeolian impact ripples. Sedimentolgy 34:943–956

Anderson RS (1988) The pattern of grainfall deposition in the lee of aeolian dunes. Sedimentolgy 35:175–188

Anderson RS (1996) The attraction of sand dunes. Nature 379:24

Ashley GM (1990) Classification of large-scale subaqueous bedforms: a new look at an old problem. J Sed Petrol 60:160–172

Baas JH (1993) Dimensional analysis of current ripples in recent and ancient depositional environments. Geologica Ultraiectina 106:1–199

Baas JH (1994) A flume study on the development and equilibrium morphology of current ripples in very fine sand. Sedimentology 41:185–209

Baas JH (1999) An empirical model for the development and equilibrium morphology of current ripples in fine sand. Sedimentology 46:123–138

Bagnold RA (1941) The Physics of Blown Sand and Desert Dunes. Chapman and Hall, Methuen London

Bennet S, Best J (1995) Mean flow and turbulence structure over fixed, two-dimensional dunes: implications for sediment transport and bedform stability. Sedimentology 42:491–513

Benza VG, Nori, Pla (1993) Mean-field theory of sandpile avalanches: From the intermittent- to the continuous-flow regime. Phys Review E 48:4095–4098

Betat A (1999) Rippelbildung granularer Materie unter dem Einfluss einer Wasserscherströmung. Ph.D. thesis, University of Magdeburg, Magdeburg

Betat A, Frette V, Rehberg I (1999) Sand Ripples Induced by Water Shear Flow in an Annular Channel. Phys Rev Letters 83:88–91

Betat A, Kruelle C, Frette V, Rehberg I (2002) Long-Time behavior of sand ripples induced by water shear flow. Eur Phys J E 8:465–476

Blatt H, Middleton G, Murray R (1980) Origin of sediment rocks. Prentice-Hall, Englewood Cliffs, N.J.

Blom A, Ribberink JS, de Vriend HJ (2003) Vertical sorting in bed forms: Flume experiments with a natural and a trimodal sediment mixture. Water Res Res 39:WR001088

Caps H, Vandewalle N (2001a) Labyrinthine granular landscapes. Phys Rev E 64:052301

Caps H, Vandewalle N (2001b) Ripple and kink dynamics. Phys Rev E 64:041302

Carling P, Gölz Orr RP (2000) The morphodynamics of fluvial sand dunes in the River Rhine. II. Hydrodynamics ans sediment transport. Sedimentolgy 47:253–278

Chakrabarti C, R.Lowe D (1981) Diffusion of sediment on the lee of dune-like bedforms: theoretical and numerical analysis. Sedimentology 28:531–545

Cockrell D, Markland E (1963) A review of incompressible diffusor flow. Aircraft Engineering 35:London

Defina A (2003) Numerical experiments on bar growth. Water Res Res 39:001455

Fredsøe J, Deigaard R (1992) Mechanics of coastal sediment transport. World Scientific

Frette V, Christensen K, Sørenssen, Feder, Jøssang, Meakin (1996) Avalanche dynamics in a pile of rice. Nature 379:49–52

Grass AJ (1971) Structural feature of turbulent flow over smooth and rough boundaries. J Fluid Mech 50:2

Grasselli Y, Herrmann H (1999) Shapes of heaps and in silos. Eur Phys J B 10:673–679

Grasselli Y, Herrmann HJ (1997) On the angles of dry granular heaps. Physica A 246:301–312

Hand BM, Bartberger (1988) Leeside sediment fallout patterns and the stability of angular bedforms. J Sed Petrol 58:33–43

Hansen J, van Hecke M, Ellegaard C, Andersen K, Bohr T, Haaning A, Sams T (2001) Stability Balloon for Two-Dimensional Vortex Ripple Patterns. Phys Rev Lett 87:204301

Hergarten S (1998) Self-organized criticality in a landslide model. Geophys Res Letters 25:801–804

Hergarten S (2002) Self-organized criticality in earth systems. Springer-Verlag, Berlin, Heidelberg, New York

Hergarten S, Hinterkausen M, Küpper M (2003) Sediment Transport - from Grains to Partial Differential Equations. Lecture Notes in Earth Sciences 97:199–214

Hoyle R, Woods (1997) Analytical model of propagating sand ripples. Phys Review E 56:6861

Hunter RE (1985) A kinematic model for the structure of lee-side deposits. Sedimentology 32:409–422

Küpper M (1999) Modellierung kleinskaliger Sedimentstrukturen in fliessenden Gewässern. Master's thesis, Institute of Geodynamic, University of Bonn

Kurtze DA, Both JA, Hong DC (2000) Surface instability in windblown sand. Phy Rev E 61:6750–6758

Leeder MR (1980) On the stability of lower stage plane beds and the absence of current ripples in coarse sands. J Geol Soc Lond 137:423–430

Li MZ, Amos W (1996) Predicting ripple roughness and sand resuspension under combined flows in a shoreface environment. Marine Geology 130:139–161

Linz SJ, Hänggi P (1995) Minimal model for avalanches in granular systems. Phys Review E 51:2538–2542

Luding S (1997) Die Physik kohäsionsloser granularer Medien. Habilitationsschrift, Universität Stuttgart

McLean SR, Nelson J, Wolfe S (1994) Trubulence structure over two-dimensional bed forms: Implication for sediment transport. J Geophy Res 99:12729–12747

Mendoza C, Zhou (1999) Theoretical derivation of yalin's (1964) empirical equation for ripple length. Mech Res Communications 26:151–159

Mohrig D, Smith JD (1996) Predicting the migration rates of subaqueous dunes. Water Res Res 32:3207–3217

Nelson J, Shreve R, McLean S, Drake T (1995) Role of near-bed turbulence structure in bed load transport and bed form mechanics. Water Res Res 31:2071–2086

Nelson JM, McLean SR, Wolfe S (1993) Mean flow and turbulence fields over two-dimensional bed forms. Water Res Res 29:3935–3953

Nelson JM, Smith J (1989) Mechanics of flow over ripples and dunes. J Geophy Res 94:8146–8162

Nikora V, Habersack H, Huber T, McEwan I (2002) On bed particle diffusion in gravel bed flows under weak bed load transport. Water Res Res 38:WR000513

Nishimori H, Ouchi N (1993) Formation of ripple patterns and dunes by wind-blown-sand. Phy Rev Let 71:197–200

Nishimori H, Yamasaki M, Andersen KH (1998) A simple model for the various pattern dynamics of dunes. Int J Modern Phy 12:257–272

Ouchi N, Nishimori H (1995) Modeling of wind-blown sand using cellular automata. Phy Rev E 52:5877–5880

Press W, Teukolsky S, Vetterling W, Flannery B (1995) Numerical Recipes in C. The Art of Scientific Computing. Cambridge University Press, Cambridge

Prigozhin L (1994) Sandpiles and river networks: Extended systems with nonlocal interactions. Phy Rev E 49:1161–1167

Prigozhin L (1999) Nonlinear dynamics of Aeolian sand ripples. Phy Rev E 60:729–733

Puls W (1981) Numerical simulation of bedform mechanics. Mitteil Inst Meereskunde Uni Hamburg 24:1–149

Pye K (1994) Sediment transport and depositional processes. Blackwell Scientific Publ., Oxford UK

Raudkivi AJ (1997) Ripples on stream bed. J Hydr Engrg 123:58–64

Rubin DM, Hunter RE (1982) Bedform climbing in theory and nature. Sedimentolgy 29:121–138

Southard JB (1971) Representation of bed configurations in depth-velocity-size diagrams. J Sedim Petrol 41:903–915

Southard JB, Boguchwal LA (1990) Bed Configurations in steady unidirectional water flows. J Sedim Petrol 60:658–679

Stegner A, Wesfreid (1999) Dynamical evolution of sand ripples under water. Phys Review E 60:R3487

Trefil J (1984) A Scientist at the Seashore. Macmillan Publishing Company, New York

Werner B (1995) Eolian dunes: Computer simulations and attractor interpretation. Geology 23:1107–1110

Werner B, Gillespie (1993) Fundamentally discrete stochastic model for wind ripple dynamics. Phys Rev Letters 71:3230–3233

Williams PB, Kemp P (1972) Initiation of ripples by artificial disturbances. J Hydr Div ASCE 98(Hy6):1057–1070

Yalin MS (1992) River Mechanics. Pergamon Press Ltd., Oxford UK

Index